Controlled Multi-Batch Self-Assembly of Micro Devices

Xiaorong Xiong

A dissertation submitted in partial fulfillment of
the requirements for the degree of Doctor of Philosophy

Doctor of Philosophy

University of Washington

2004

Program Authorized to Offer Degree: Electrical Engineering

University of Washington
Graduate School

This is to certify that I have examined this copy of a doctoral dissertation by

Xiaorong Xiong

and have found that it is complete and satisfactory in all respects,
and that any and all revisions required by the final
examining committee have been made.

Chair of Supervisory Committee:

Karl F. Böhringer

Reading Committee:

Karl F. Böhringer

Daniel T. Schwartz

Robert Bruce Darling

Date:

In presenting this dissertation in partial fulfillment of the requirements for the doctoral degree at the University of Washington, I agree that the Library shall make its copies freely available for inspection. I further agree that extensive copying of the dissertation is allowable only for scholarly purposes, consistent with .fair use. as prescribed in the U.S. Copyright Law. Requests for copying or reproduction of this dissertation may be referred to Proquest Information and Learning, 300 North Zeeb Road, Ann Arbor, MI 48106-1346, to whom the author has granted .the right to reproduce and sell (a) copies of the manuscript in microform and/or (b) printed copies of the manuscript made from microform.

Signature____________________________

Date____________________________

University of Washington

Abstract

Controlled Multi-Batch Self-Assembly of Micro Devices

by Xiaorong Xiong

Chair of Supervisory Committee:

Professor Karl F. Böhringer
Department of Electrical Engineering

A technique is described for assembly of multiple batches of micro components onto a single substrate. The substrate is prepared with hydrophobic alkanethiol-coated gold binding sites. To perform assembly, a hydrocarbon oil is applied to the substrate and wets exclusively the hydrophobic binding sites in water. Micro components are then added to the water, and assembled on the oil-wetted binding sites. Moreover, assembly can be controlled to take place on desired binding sites by using an electrochemical method to de-activate specific substrate binding sites. By repeatedly applying this technique, different batches of micro components can be assembled to a single substrate sequentially. As a post assembly procedure, electroplating is incorporated into the technique to establish electrical connections for assembled components. Important issues presented are: substrate fabrication techniques, electrochemical modulation by using suitable alkanethiol (dodecanethiol), electroplating of tin and lead alloy, surface energy and surface tension force simulation and binding site design simulations. Finally, We demonstrate: a two-batch assembly of silicon square parts, electrical connectivity establishment by electroplating contacts to assembled surface-mount light emitting diodes (LEDs) and self-assembly of nano devices such as polystyrene beads.

TABLE OF CONTENTS

LIST OF FIGURES

LIST OF TABLES

ACKNOWLEDGMENTS

This thesis is the result of an important and enjoyable journey, whereby I have been supported and accompanied by many people. First, I'd like to thank my advisor Professor Karl F. Böhringer for providing me with the unique opportunity to work on the idea of self-assembly, for giving me the freedom of carrying out the research and for offering the guidance, support and knowledge. Ever since our first meeting with Professor Daniel T. Schwartz, he has become not only a collaborator but also my bona fide second advisor. I would express my appreciation for his unique perspective from the electrochemistry end and for his determination and enthusiasm. Thanks also to my committee members Professor Robert Bruce Darling and Professor Keith A Holsapple for their help and advice.

Thanks to all the past and current members in the MEMS group, who have made my work and life at University of Washington fun experience: Professor Tai C. Chen, Xuanghong Cheng, Yanbing Wang, Yu-Ming Chen, Jiandong Fang, Sidhartha Goyal, Anupama Govindarajan, Udo Lang, Ashutosh Shastry and Jaideep Mavoori. I'd like to specially thank Dr. Yael Hanein, who has offered generous help and great ideas. I've really enjoyed the time working with her. Working with Sheng-Hsiung Liang on geometric design, Nels Jewell-Larsen and Kerwin Wang on nano-assembly has been good time.

I would like to thank our collaborators: J. Lienemann, Dr. A. Greiner Prof. J. G. Korvink at Albert Ludwig University in Germany for their contributions in self-assembly modelling; Professor Shaoyi Jiang and Dr. Shengfu Chen at the Chemical Engineering Department for generously providing us with mica samples and Dr. Weihua Wang for her help and hospitality during my days in the electrochemistry lab. Special thanks to Professor Roger Howe and Dr. Uthara Srinivasan at University of California, Berkeley for insightful discussions and advice.

Support for our self-assembly research was provided in part by the National Science

Foundation (NSF) Career Award NSF ECS-9875367 to Karl F. Böhringer and a Ford Fellowship to Xiaorong Xiong and in part by Agilent, HP, Intel, Microsoft Research, Tanner, Tektronix, Washington Technology Center.

Finally, I'd like to thank my family and friends for their support.

DEDICATION

To my parents and my husband.

Chapter 1

INTRODUCTION

1.1 Background and motivation

The development of micro electromechanical systems (MEMS) has been based on the techniques and tools traditionally used for the silicon integrated circuits (IC) industry. In Peterson's paper [1] of 1982, he envisioned a major trend towards silicon machining motivated by the excellent mechanical properties of single crystal silicon. In the past two decades, research and development have demonstrated novel devices based on bulk and surface micro machining.

More recently, pioneering research has extended the traditional semiconductor manufacturing techniques into smaller scales and into a much wider variety of application fields. With the latest innovative fabrication techniques, micro structures and devices have been manufactured by using new materials beyond the silicon, such as plastics, alloys, ceramic, polymer, piezo-materials and biomaterials. A wide range of micro functionalities (communicating, sensing, actuating, computing etc.) have been developed. Successful commercial products include accelerometers as in air bag sensors [2–4] or micro-fabricated printer heads [5]. More recently, invented at Bell labs, Lucent's commercial WaveStar$^{(\mathrm{TM})}$ optical switches use arrays of microscopic mirrors to steer optical signals between optical fiber, which enables the all optical networks. The digital mirror device (DMD) developed and commercialized by Texas Instruments' have been used as digital light switches for display systems. The surface-machined mirrors with controlled movement are used to precisely project light source [6]. In the wireless communication areas, radio frequency (RF) MEMS switches have been developed with the advantages of low power consumption and high isolation compared to positive intrinsic negative (PIN) diodes or field effect transistor (FET) switches [7]. In addition, advances in BioMEMS have found promising applications in the areas including development of microfluidic systems, medical diagnostics and therapeutical devices [8–14].

With all these innovative developments, a large variety of functionalities have emerged. Integration of these functionalities into compact, reliable micro systems with high performance has become an important issue. In general, integration methods can be divided into two classes: monolith and hybrid integration. Monolithic integration, as a wafer level process, is realized by fabricating all the functionalities through the same process on a single wafer [15–18]. It is widely used for micro electronics, which provides low cost integration particularly in large volume. On the downside, monolithic integration is often limited by poor compatibility between functionalities' fabrication processes or materials. To circumvent the problems caused by the incompatibility, hybrid integration is used. It can integrate functionalities from different fabrication processes and different materials, and therefore increase the flexibility of the system. As hybrid integration is realized by assembly of the different functionalities after fabrication, the development of an efficient low cost assembly method is of great importance. In the following sections, we will review and discuss different techniques for assembly at the micro scale, which are referred to as micro-assembly techniques in the rest of this dissertation.

1.2 Micro-assembly

Micro-assembly, as an important step in hybrid integration, provides a solution to circumvent the difficulties caused by monolithic integration. In general, micro-assembly is performed after each batch of the individual devices is fabricated and tested separately, and prior to other packaging processes. As advantages, micro-assembly allows micro devices to be fabricated through optimized processes and materials; with independent tests of each component before integration. Therefore, the reliability of the final system can be improved.

A thorough study and analysis of various micro assembly strategies was presented by Cohn [19]. A number of techniques developed to assemble micro components into complex systems can be divided into two major categories: serial and parallel assembly. In the serial assembly category, "pick and place" methods are used to perform the assembly. In the parallel assembly category, wafer-to-wafer transfer and self-assembly approaches have been developed.

1.2.1 "Pick and place"

As a straightforward approach, conventional "pick and place" serial assembly methods have been adopted in the micro domain by using miniaturized robots and tools for moving and placing parts with high precision. There are two major concerns about this technique: time efficiency and the "sticking problem". The first is due to the serial manipulation. When a large number of parts need to be assembled, the time for assembly will be limited by the number of manipulators. Hence, this method might only be applicable to systems consisting of rather small number of components.

The "sticking problem" is caused by the adhesive forces between manipulator surfaces and parts. With parts smaller than a millimeter, the forces primarily due to electrostatic, van der Waals or surface tension, are significant compared to gravitational force [20]. To overcome the "sticking problem", robots and manipulators with special design [21] or with feedback controlled have been used [22–24]. For assembly of nano parts, atomic force microscopes (AFMs), scanning electron microscope (SEM) and focus ion beam (FIB) systems to perform manipulating, positioning and assembly [25–27].

In order to accomplish efficient micro assembly of a very large number of components, parallel assembly approaches have emerged, falling into two major categories: wafer-to-wafer transfer and self-assembly.

1.2.2 Wafer-to-wafer transfer assembly

Micro-assembly of different components can be realized by transferring micro structures between aligned wafers [28–30]. In [28, 29], two wafers, a donor wafer and a target wafer, are prepared with different micro structures. To integrate them, the donor wafer is first aligned with the target wafer, and then it is pressed against the target wafer with metal bumps. With reflow, the metal bumps can bond the micro structures on the donor wafer to the target wafer. When the donor wafer is moved away from the target, specifically designed "tethers" on these micro structures will break and the micro structures will be assembled to the target wafer.

1.2.3 Self-assembly

Self-assembly refers to assembly processes that organize individual components into structures without human intervention [31]. It can also be described as a stochastic assembly process which takes place spontaneously without external control. Self-assembly widely happens in nature, with self-assembled systems ranging from bacteria to solar systems. As an example, complex supramolecular frameworks have been formed from "programmed" molecular subunits spontaneously by self-assembly [32,33].

In technology, processes have been developed to imitate what happens in nature to self-assemble different components and organize them into desired structures and functional systems. A large variety of methods, in place of the traditional assembly methods widely used at the macro scales, have been created by using different driving mechanisms. They can be applied to build integrated systems, particularly at micro or nano scales. To describe the methods in the self-assembly category in general, assembly of a large number of identical micro parts occurs on specifically designed identical target sites. The assembly of all the micro components takes place simultaneously and the final assignment of each part to its destined site is random. Self-assembly methods can be divided into different categories in terms of driving forces such as electrostatic forces, magnetic forces, surface tension forces etc.

Complementary geometric shape recognition

Yeh and Smith developed a process called fluidic self-assembly (FSA$^{(\mathrm{TM})}$) [34,35]. When fluid with trapezoidal micro components flows on a substrate with complementary holes, the parts can be trapped into the holes, and therefore be assembled on the substrate (Fig. 1.1). After assembly, the substrate is planarized and a metallization process is performed to establish electrical connections for the parts.

As a commercialized patented process, FSA$^{(TM)}$ has been applied to produce flexible display systems, and more recently to manufacture high-volume low cost radio frequency identification (RFID) products [36].

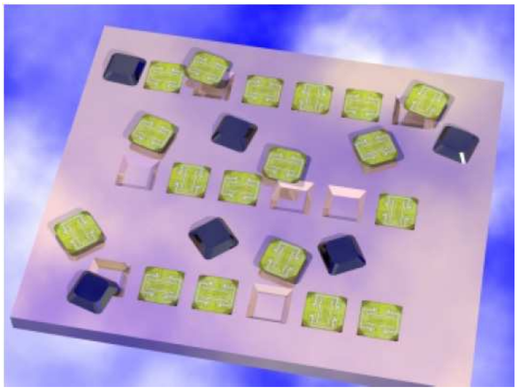

Figure 1.1: An illustration of FSA$^{(TM)}$ process. The holes on the substrate have three dimensional complementary shapes with the parts. Parts can be assembled and fill in the holes [36].

Magnetic driving force

The methods in this category use magnetic forces to drive the assembly [37–39]. In [37], magnetic nano wires suspending in fluid have been assembled with the help of magnetic forces to align them with designed orientation. In [38, 39], superparamagnetic colloidal particles have been assembled to desired 2D patterns by magnetic forces. Different methods have been demonstrated to control the number of beads deposited [38]. By switching the magnetic forces from repulsive to attractive, the particles can be moved into holes on a substrate, and vice versa [39].

Electrostatic driving force

Electrostatic forces have been used to assemble components ranging from nano to millimeters to construct complex 2D or 3D structures [40–44]. Böhringer et al. have proposed a self-assembly approach by employing electrostatic driving force applied to microscopic parts such as surface mount capacitors, with the aid of ultrasonic vibration to overcome and eliminate friction and adhesion [42]. In [43], an electrostatic self-assembly approach is applied to selectively pattern charged 10μm gold disks on a substrate. Grzybowski et al. have successfully demonstrated self-assembly and organization of two types of macro crystals by using electrostatic force. Two different polymetric crystals are charged oppositely with agitation on a gold surface. With the electrostatic force between the crystals, they can be self-assembled into well-organized structures and the structures can be controlled by the ratio between the different crystals [44]. Results from assembly of different combinations of crystals are shown in Fig 1.2.

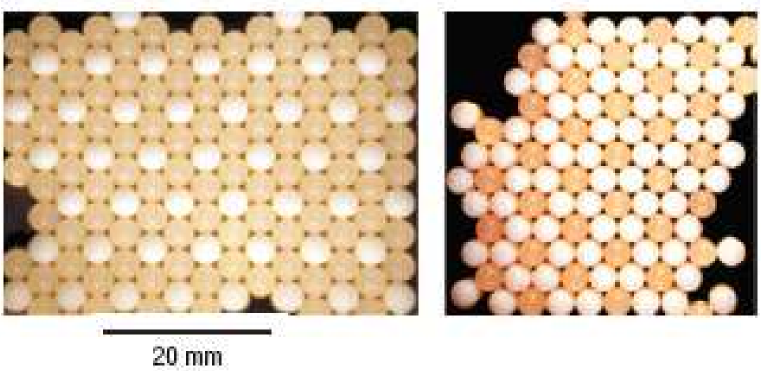

Figure 1.2: Two types of macro crystals of different materials are self-assembled and organized in certain patterns by electrostatic forces. The patterns are determined by the ratio of the two crystals [44].

Chemical and biological binding force

As inspired by nature, self-assembly approaches have developed by using biological and chemical binding forces between certain molecules such as DNA and protein [45–47]. For applications in chemical (biological) sensing and detection, cells have to be attached and patterned. Self-assembly and patterning of different cell populations methods been successfully demonstrated in the area of cell biology [45, 46]. In [45], an electrochemical reduction has been used to change the surface chemistry in order to control the cell culture. In [46], a thermally reactive polymer has been deposited on fabricated micro heater arrays. By using the heaters to change the polymer surface property, protein patterning and selective adsorption and growth of cell cultures can be accomplished. In [47], self-assembly of nano beads, Au particles and micro devices have been accomplished by using the hybridization of single strand (ss)- to double-stranded (ds) DNA and the bonding between ligand (avidin) and receptor (biotin).

Surface tension driving force

Surface tension force, which scales linearly with dimension, becomes dominant at the micro domain. It is capable of driving micro scale motions for various applications: high-resolution wet printing [48, 49]; a liquid-metal micromotor [50]; three-dimensional hinged micro structures [51] and formation of micro optical lens [52]. It can also be involved as the driving force for micro-assembly. Syms et al. review the state of the art surface-tension driven packaging and self-assembly approaches in [53]. In particular, success has been achieved in creating a large variety of micro structures by self-assembly of objects using surface tension forces at micro and even nano scale [54–60].

Whitesides and coworkers first developed a strategy driven by surface tension force to self-assemble millimeter light emitting diodes (LEDs) into simple electrical circuits [56, 57]. To prepare for the assembly, the parts are patterned with active hydrophobic surfaces and protective hydrophilic surfaces. The assembly is the result of both geometric shape matching and the hydrophobic interaction with the presence of a hydrophobic ultraviolet (UV) curable lubricant in an aqueous environment. Later three-dimensional electronic networks [55] have been built from millimeter-sized functional parts, by using liquid solder to self-assemble and align polyhedral parts (Fig. 1.3(a)).

Srinivasan et al. adopted the capillary force driven assembly technique in [56, 57] to assemble microscopic parts onto desired sites on silicon and quartz substrates [58, 59] by using a hydrocarbon polymer as the lubricant. It has succeeded in self-assembling micromirrors onto a substrate with desired configuration shown in Fig. 1.3(b) [54]. In general, the substrate is patterned with hydrophobic alkanethiol self-assembled monolayer (SAM) coated gold patterns on hydrophilic background. A lubricant, deposited exclusively on the hydrophobic patterns, is used to attract and assemble the microscopic parts on to a single substrate in water, and the lubricant is then hardened to physically bond the parts. Recently, self-assembled arrays of GaAs/GaAlAs LEDs on a flexible curved substrate have also been demonstrated in [60]. In this approach, metal solder has been used as the lubricant to establish both physical and electrical connectivity between the LEDs and a flexible substrate (Fig. 1.3(c)).

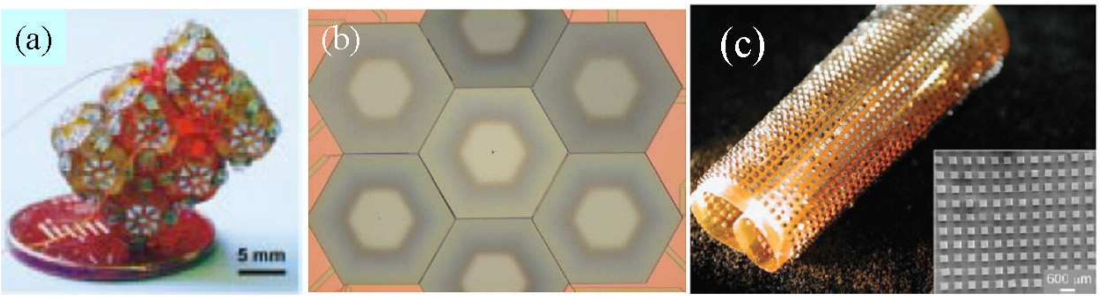

Figure 1.3: Surface-tension-driven assembly results: (a) a self-assembled three dimensional network of polyhedrons [55]; (b) an array of functional micro mirrors self-assembled on a single silicon substrate [54] and (c) a curved flexible substrate with arrays of self-assembled GaAs/GaAlAs LEDs [60].

1.2.4 Multi-batch self-assembly

In summary, surface tension force, as a dominant force at the micro scale, has demonstrated the capability of driving self-assembly of micro and millimeter parts with high alignment precision and yield [55–61]. However, in all the studies in the surface-tension-driven category, parallel assembly has been performed with only one batch of identical components (Figs. 1.3). For the assembled devices, either none or only one electrical connection was established.

In practice, as a system integration method, assembly of different functionalities is necessary. In addition, multiple electrical connections for assembled parts might be required. Therefore, for general micro devices assembly, we develop a new approach to assemble multiple batches of components followed by establishment of multiple electrical connections in a parallel manner.

In principle, our self-assembly method is driven by capillary force and it proceeds on specially treated hydrophobic sites on the substrate as described in [58, 59]. In addition, electrochemical modulation of the hydrophobicity of specific binding sites is used to alter the driving force for assembly. With this added innovation, assembly can be controlled to take place only on desired binding sites. By repeating the process to activate different sites on the substrate for assembly, different batches of micro parts can be assembled on a single substrate in a sequential manner. Electroplating is exploited as a post assembly process to establish electrical connections for assembled components, such as LEDs.

The multi-batch assembly is the combination of surface-tension driven self-assembly, the electrochemical surface modulation and electroplating methods. The important issues in the development of this approach include: fabrication process design for the substrates suitable for the multi-batch assembly; integration of the electrochemical surface modulation method into the self-assembly technique; development of electroplating as a post-assembly process to establish electrical connections between assembled parts and substrate in a parallel manner. To study the process, we analyze the surface energy and surface tension forces associated with the self-assembly process by using *variational calculus* and finite element methods. In addition, a binding site design method is investigated, which can be used to find designs ensuring the uniqueness of assembly alignment.

The rest of the chapters are dedicated to address these issues. In Chapter 2, the principles of this technique are investigated. An overview of all the processes for this technique is presented with explanation of each step. Chapter 3 includes the discussions of the fabrication process development, and self-assembly experimental design. For assembly of different micro parts such as Si parts and LEDs, substrates with different design are used. In Chapter 4, we discuss the models for the surface energy and surface tension forces associated with the self-assembly process. A numerical simulation tool is used to obtain the quantitative information of the energy and the force, with which we can estimate the assembly motion and gain better understanding of the self-assembly process. In Chapter 5, we address the binding site design issue for the self-assembly, which can be used to find designs ensuring a unique self-assembly position and orientation. In Chapter 6, we investigate the details of characterization and experimental implementation of the electrochemical surface modulation and electroplating methods. In Chapter 7, we study the scaling effects of this technique in order to find the working domain. Initial attempts of extending it to the nano scale are described. Finally, the summaries and conclusions are presented in Chapter 8.

Chapter 2

MULTI-BATCH SURFACE-TENSION DRIVEN SELF-ASSEMBLY CONCEPTS

To achieve multi-batch assembly, we integrate electrochemical surface modulation to the surface-tension driven self-assembly method. In this chapter, we discuss the process concepts of the multi-batch self-assembly technique, with focus on explaining the principles of the surface tension driven self-assembly and electrochemical surface modulation.

2.1 Process concepts

In Figs. 2.1(a)-(g), we illustrate the schematic flow of our self-assembly approach, which is explained step by step in this section. First, a supporting structure destined for the assembly (referred to as "substrate" hereafter) is fabricated with exposed clean hydrophilic gold (Au) patterns (Fig. 2.1(a)). The assembly "parts", defined as those objects that are to be assembled, are prepared with corresponding patterns. For simplicity, we use the term "binding sites" for the exposed gold patterns on the substrate and the corresponding patterns on the parts.

Second, the substrate is soaked in ethanolic alkanethiol ($CH_3(CH_2)_nSH$) solution and a hydrophobic alkanethiol self-assembled monolayer is chemisorbed on the exposed Au patterns [62]. The SAM adsorption activates all the Au binding sites on the substrate for assembly. The remaining areas on the substrate stay hydrophilic (Fig. 2.1(b)). In order to control the assembly to take place on selected binding sites, we use an electrochemical method to modulate the hydrophobicity of the binding sites we wish to de-activate (Fig. 2.1(c)) by removing the SAM from the surface. After the desorption process, assembly occurs only at the hydrophobic binding sites. Fig. 2.1(d) depicts the assembly process, which includes lubricant application, part transferring and alignment steps. For assembly,

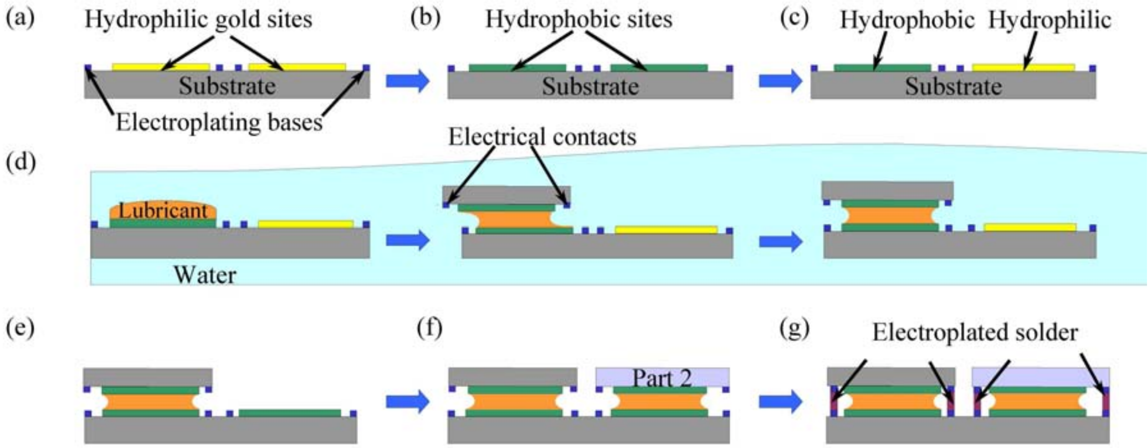

Figure 2.1: Schematics of two-batch assembly steps: (a) a micro fabricated substrate with electrically isolated regions of hydrophilic Au binding sites and Ni electroplating bases; (b) alkanethiol SAM adsorbed on Au patterns turns them hydrophobic; (c) electrochemical SAM desorption from selected binding site (the right site) is used to de-activate it for assembly; (d) application and partitioning of a hydrocarbon lubricant to a hydrophobic binding site, followed by assembly of the part and lubricant curing in an aqueous environment; (e) deposition of alkanethiol SAM on the vacant Au binding site to activate it for another assembly; (f) repeating the step in (d) for other micro parts; (g) establishing electrical connections between assembled parts and the substrate by electroplating. Note that the vertical dimensions have been exaggerated for illustration purposes.

the capillary driving force is created by a hydrocarbon-based lubricant liquid meniscus between binding sites on a part and on a substrate in an aqueous environment. The lubricant is spread on the dry substrate. After being immersed in water, the lubricant wets only the SAM-coated hydrophobic patterns. Parts are then transferred into water and aligned by surface tension forces. Next, the lubricant is polymerized by heat and the parts are permanently bonded to the substrate. During the assembly process, the hydrophilic Au binding sites which have gone through SAM desorption remain clean and are reserved for future assembly. By repeating the SAM adsorption and assembly process, another batch of micro parts can be assembled on the vacant binding sites (Figs. 2.1(e), (f)).

After assembly, different micro parts are physically bonded to the substrate. In most cases, electrical connections and controls for these parts are needed. An electroplating method has been investigated for this purpose. By electroplating, metal alloy can be deposited on the plating bases on the substrate to establish electrical connections between the assembled parts and the substrate in a parallel manner (Fig. 2.1(g)).

2.2 Surface tension driven self-assembly

In this section, we discuss the principle of the surface tension driven self-assembly technique in detail. In general, the self-assembly and self-alignment phenomenon is the result of minimization of the interfacial energy between the lubricant meniscus and water. As discussed in the previous section, the self-assembly process has three steps (Figs. 2.1(d)), in which surface tension force plays a significant role in each of the step. In the first step, when a substrate with lubricant is immersed in water, the lubricant stays exclusively on the hydrophobic binding sites, while water occupies all the hydrophilic areas. The different wetting phenomena are the result of surface energy minimization, as the lubricant-SAM interfacial tension ($\gamma <1$ mJ/m^2 [61]) is much lower than that of the water-SAM interface ($\gamma \approx$ 50mJ/m^2). In the second step, when a part is introduced in water, with agitation the part surface will contact with the lubricant in water and the lubricant will wet its hydrophobic surface as well, due to the same reason as described above. As a result, it forms a meniscus between the substrate binding site and the part. The third step is the self-alignment step. After the second step as shown in the middle plot of Figs. 2.1(d), the lubricant-water interfacial energy is usually not minimal. The morphology of the meniscus tends to change in order to decrease its interface with water, therefore reducing the lubricant-water interfacial energy. The driving force for self-assembly of the part is generated from the interfacial energy change. When the energy reaches minimum, the driving force becomes zero and the part should be aligned with a substrate binding site.

2.3 Surface modification techniques

The study of self-assembled monolayers of organic molecules on metal or other surfaces has been the subject of hundreds of scientific papers. The adsorption and desorption of the monolayer has been used to "engineer" surfaces for potential applications in wetting, lubrication, adhesion, corrosion,catalysis, chemical and biological sensing and nano scale fabrication. The usage of SAM formation to change surface hydrophobicity for the purpose of assembling micro structures was first demonstrated in Whitesides' group [63]. As discussed in the previous sections, our multi-batch self-assembly technique extends the previous single-batch approach to multi-batch by adopting the SAM desorption in the assembly process. The crucial issue is how to engineer the surface hydrophobicity. In our technique, the surface is changed from hydrophilic to hydrophobic by SAM formation on gold, while the surface property is reversed by desorbing the SAM from gold. The following sections are dedicated to discussing how to adsorb and desorb the SAM.

2.3.1 Alkanethiol SAM adsorption

The active binding site for assembly consists of a self-assembled alkanethiol monolayer on a gold surface. The sulfur compound of the alkanethiols will be chemisorbed on metals such as gold, silver, platinum etc. The most common method to form SAM on Au is by soaking the Au substrate in the thiol solution at room temperature, with ethanol as the most common solvent [64]. Another common method, which has been widely used to pattern SAMs of different thiols, is contact printing. An elastomer stamp with thiol solution as the "ink" is pressed on the Au surface in order to transfer the thiol to the Au surface [65]. Electrochemical method can also be used for SAM deposition [63,66]. By applying positive potential bias to Au surface in alkaline electrolyte with alkanethiol, SAM can be formed on the surface. Another method to perform SAM adsorption is through gas-phase transfer in vacuum [67].

We have chosen to use the first method for SAM adsorption. The reason is based on considerations of the compatibility of the method with other assembly processes and the complexity of its implementation. The method is simple to implement, and does not require special treatment such as vacuum or plasma. It can be easily incorporated with other processes. By exposing Au to the alkanethiol in solvent, the monolayer can be formed. The self-assembly process will take place in minutes (Fig. 2.1(b)), however more incubation time is needed to get full coverage, and well ordered monolayers.

In addition, to achieve a fully covered and well organized monolayer, the metal surface has to be free of organic contaminants. Therefore, cleaning process is performed by using oxygen plasma or nano-strip$^{(\mathrm{TM})}$ (H_2SO_4/H_2O_2, Cyantek Corp) soaking prior to the adsorption process.

2.3.2 Alkanethiol SAM reductive desorption

To realize the multi-batch assembly, the key is how to selectively activate the binding sites. As discussed in the previous section, the adsorption method does not have any selectivity, as alkanethiol forms SAM on all the Au binding sites. In this section we discuss the methods that can be used to selectively modulate the surface properties, and specifically, to desorb the SAM.

One method is electrochemical desorption, which is commonly used for the purpose of characterizing the SAMs [62, 68, 69], e.g. for the measurement of the SAM coverage [69]. By applying potential bias to the Au electrode in an alkaline solution, the SAM can be desorbed from the Au surface by reduction, i.e.,

$CH_3(CH_2)_nSAu + e^- \rightarrow Au + CH_3(CH_2)_nS^-$.

After desorption, the Au surface is free of SAM, and becomes hydrophilic, and the desorbed alkanethiol dissolves into the solution.

There is another method that uses pyrimidine-terminated thiols that are sensitive to UV light [70]. When exposed to the UV light of certain wavelengths (240nm or 280nm), the contact angle of the thiol monolayer can be changed as much as of 38°. Compared to the electrochemical method, it has drawbacks such as the limited change of hydrophobicity and the complexity of operation.

Therefore, we use the electrochemical reductive desorption of the SAM on gold as shown in Fig. 2.1(b) to change the surface from hydrophobic to hydrophilic. To perform the desorption, potential bias is applied to the selected binding sites. After the desorption they are de-activated and can be re-activated later for assembly of different batches.

In Chapter 6, we will discuss reductive desorption characterization of different alkanethiol SAMs, the implementation of this method and how to adapt it into the assembly experiment.

Based on this characterization we chose dodecanethiol ($CH_3(CH_2)_{11}SH$) for our assembly experiments.

2.4 Summary

To summarize, we have described the process concepts (Figs. 2.1) of our multi-batch assembly approach in this chapter. The process include fabrication (Fig. 2.1(a)), surface modulation (Figs. 2.1(b)(c)), self-assembly (Figs. 2.1(d)) and electroplating (Fig. 2.1(g)). By repeating the surface modulation and self-assembly steps as shown in Figs. 2.1(e) and (f), multi-batch assembly can be achieved. In particular, the principles of the self-assembly and the surface modulation methods are also discussed. In next chapter, we will focus on the fabrication issue and the experimental method of the self-assembly.

Chapter 3

FABRICATION PROCESS DEVELOPMENT AND SELF-ASSEMBLY EXPERIMENTAL METHOD

From the discussion of the multi-batch self-assembly principles in the previous chapter, it follows that the development of this technique should combine the fabrication, surface modification and electroplating approaches, so as to accomplish the assembly and integration of different components into a functional system. The entire experimental process sequence includes the fabrication of suitable substrates and parts, SAM adsorption and selective desorption, assembly setup, and finally, the electroplating process. In this chapter, we describe the fabrication process and experimental methods used to perform the self-assembly.

We use two types of components for the experiments: silicon parts and commercial surface mount LEDs. In general the experimental processes are the same for both components, except the silicon parts do not need electroplating after assembly, therefore fabrication processes for the suitable substrate are less complicated.

3.1 Fabrication of substrates and parts

3.1.1 Test silicon part fabrication

We use two types of $1\times1\text{mm}^2$ silicon test parts for multi-batch assembly. The first batch of parts has square Au patterns ($1\times1\text{mm}^2$) on one side, serving as the binding site, and Au patterns of $0.8\times0.8\text{mm}^2$ on the other side. The second batch of parts is patterned with $1\times1\text{mm}^2$ Au binding sites on one side. The second batch of parts is fabricated by dicing a silicon wafer, which has an adhesion layer of 100Å chrome (Cr) and 1000Å Au sputtered on the polished side. The square test parts are used as fabricated without any further processing. Untreated Au surfaces have a contact angle of 63° after exposure to lab atmosphere, which is sufficient to ensure assembly.

Commercial devices, i.e., surface mount LEDs (0.8×1.6mm, Lumex), are used as assembly components to demonstrate the electroplating method.

3.1.2 Substrate fabrication

In Figs. 3.1(a)-(e), we show the schematic fabrication flow of a substrate designed to support self-assembly of square test parts. The substrate is prepared with a thermal oxidation layer of approximately 4500Å as an isolation layer on a 3” (100) silicon wafer (Fig. 3.1(b)). Next, a layer of Cr/Au is patterned on the substrate by a lift-off process. The substrate is first patterned with photoresist (AZ1512, Clariant), followed by sputtering of Cr (100Å) and Au (1000Å) on the substrate. The photoresist is then dissolved by acetone, and the metal layer is patterned on the substrate (Fig. 3.1(c)). The wafer is then cleaned with isopropyl alcohol (IPA), deionized (DI) water and dried with N_2. An approximately 3000Å thick passivation layer of spin-on glass (SOG) (311, Honeywell) is spun on and cured, before photoresist AZ1512 is patterned as a mask to define the SOG pattern. This step is followed by a reactive ion etch (RIE Phantom, Trion technology) of CH_3F with O_2 to expose the Au binding sites. Finally, the substrate is cleaned with acetone to strip off the photoresist, rinsed with IPA, DI water and dried with N_2 (Figs. 3.1(d) and (e)). Figs. 3.2 show the cross-section and a top view of a substrate designed for LED assembly and to demonstrate electroplating. To prepare such a substrate, a Cr/Au layer is patterned as the binding sites for assembly. Additional metallization layers of 100Å Cr and 250Å nickel (Ni) are thermally evaporated and patterned by lift-off, prior to the Cr/Au layer deposition. This additional Cr/Ni layer is patterned as metal bases for electroplating, as well as the connections between the Au binding sites and the electrical contacts (Fig. 3.2(b)). The electrical contacts serve as an interface to the external control for the electroplating process, and to activate the LEDs afterwards. Silicon nitride (3000Å) is sputtered as a passivation layer. The passivation layer is patterned photolithographically with an adhesion layer of primer (prime-P10, Shin-EtsuMicroSi) and AZ1512 photoresist. Finally, RIE of SF_6 is used to etch the nitride layer to expose the binding sites and the electroplating bases. This step is followed by acetone, IPA, and DI water cleaning and N_2 dry.

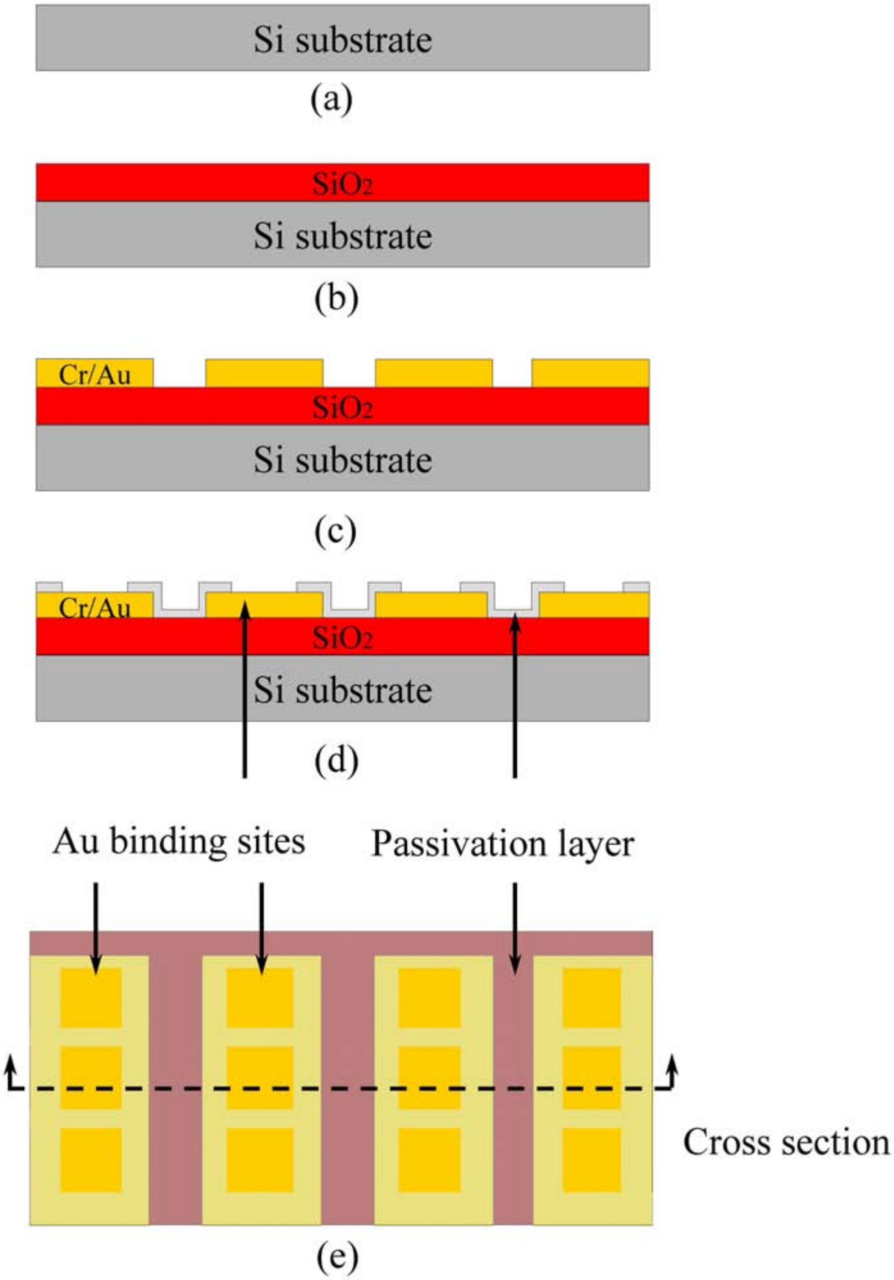

Figure 3.1: Fabrication flow of substrates designed for square test parts assembly. (a) Silicon substrate. (b) Silicon dioxide layer, which isolates the silicon substrate from the metal layer. (c) Cr/Au metallization layer. Here, this layer is patterned with an array of electrically isolated stripes. (d) Passivation layer of SOG. This layer has openings that expose the square binding sites on the Au stripes. (e) Top view of a fabricated substrate.

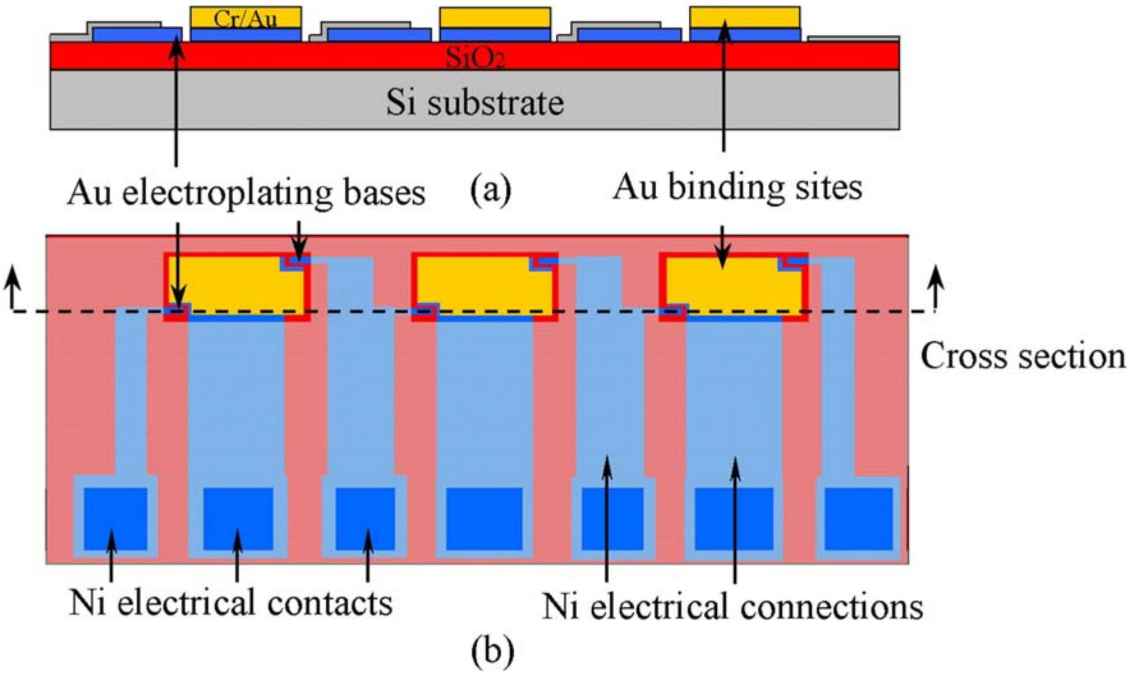

Figure 3.2: Schematic plots of a fabricated substrate to support LED assembly and electroplating. (a) Cross-section of the substrate. (b) A top view of the substrate.

As examples, pictures of fabricated substrates for the assembly are shown in Fig. 3.3: Fig. 3.3(a) is a picture of a substrate with square binding sites (inserted figure at left bottom) for silicon parts assembly; Fig. 3.3(b) is the picture of a substrate with specific binding sites for LED (inserted figure at left bottom) assembly.

3.2 Surface modification

To prepare for the assembly, electrochemical modulation of surface hydrophobicity is performed. The purpose of surface modification is to activate some binding sites on the substrate, while keeping the other binding sites inactive. The active ones are hydrophobic

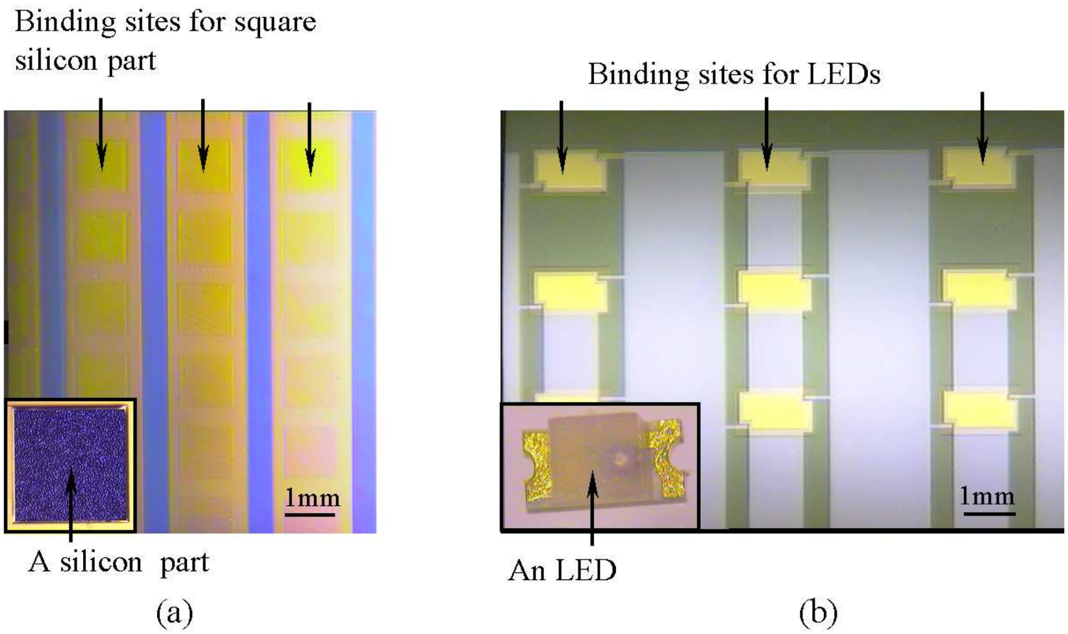

Figure 3.3: Pictures of fabricated substrates for assembly of different components. (a) A substrate for assembly of square silicon parts. The picture of a Si part is inserted at the left bottom. (b) A substrate for assembly of LEDs. The picture of an LED is inserted at the left bottom.

binding sites, while the inactive ones are hydrophilic. The surface modification methods include: surface cleaning and alkanethiol SAM adsorption and desorption.

3.2.1 Surface cleaning

The Au surface has high free energy, which is in the order of 100mJ/cm^2 [71]. Such a surface is easy to be contaminated, as the consequence of reducing the free surface energy. Nonpolar organic contaminants are easily adsorbed on the Au surface [64, 71] in the lab environment. Such organic contaminants on the Au surface will increase its hydrophobicity. It has been observed that exposure of Au to atmosphere even for a short time will significantly increase the surface hydrophobicity. Therefore, a cleaning process is crucial for our experiments to keep the Au surface free of organic contaminant and hydrophilic.

We use two minutes of oxygen plasma to clean the substrate. In addition, nano-strip$^{(\mathrm{TM})}$

cleaning is found to be effective as well. The samples have to be soaking in nano-strip for twenty minutes, followed by DI water rinsing and N_2 dry, prior to the SAM adsorption process. Both processes can remove the contaminants and make the gold surface hydrophilic. After the clean step, the substrate has to be put in ethanolic alkanethiol solution, or it has to be stored in ethanol to prevent it from being contaminated again.

3.2.2 SAM adsorption

The SAM adsorption is used to activate binding sites for assembly. In this step, an alkanethiol SAM is formed on the Au surface. Therefore, the binding sites on the surface can be activated and turned hydrophobic. For the alkanethiol adsorption, the cleaned substrate is placed into a glass container with freshly prepared ethonalic alkanethiol solution. The solution is prepared with 1mM alkanethiols ($CH_3(CH_2)_nSH$, Aldrich) in ethanol, and the substrate is soaked in the solution for at least two hours to allow SAM adsorption [64,69,72]. Usually, the alkanethiol is deposited on the Au surface in seconds, however, to get a stable alkanethiol monolayer, the substrate is soaked in the solution for approximately 10 hours [64, 72, 73]. Discussion of the adsorption mechanism is discussed in Chapter 6 in detail. Thus, an alkanethiol monolayer is deposited on the exposed Au areas on the substrate. After the adsorption process, the exposed Au binding sites turn hydrophobic with a contact angle in the range of 110° [64].

3.2.3 Selective SAM desorption

After the adsorption process, all the Au binding sites are activated. To control the assembly to take place on the selected sites, we deactivate others. In other words, we remove the SAM from these binding sites by using an electrochemical desorption method.

The electrochemical desorption of alkanethiol SAMs is employed to modulate surface hydrophobicity. Reductive desorption of SAMs is performed in a conventional three-electrode electrochemical cell [74], as shown in Fig. 3.4.

SAM coated Au surfaces, i.e., the binding sites on fabricated wafers and Au(111) on mica samples, act as the working electrodes. The counter electrode is a platinum mesh. A satu-

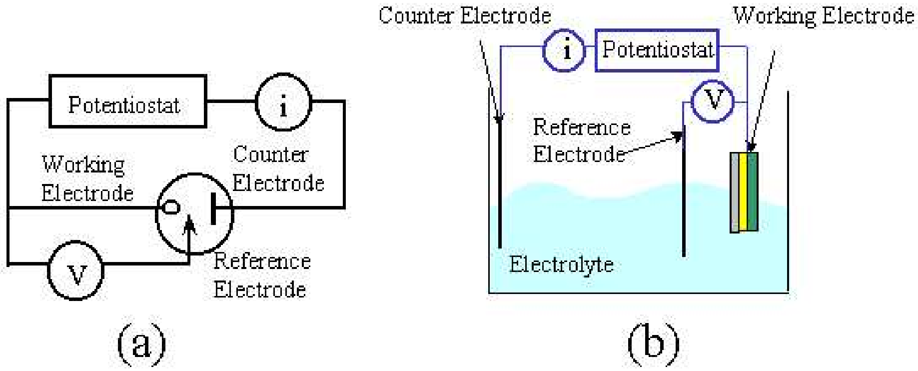

Figure 3.4: Three-electrode electrochemical cell. (a) Concept drawing of the electrochemical cell. (b) Experiment setup of the cell.

rated calomel electrode (SCE, Accumet) is used as the reference electrode. The electrolyte is 0.5 M (pH=13.5) aqueous KOH (Fisher Scientific) solution. The potential is controlled between the working and the reference electrodes, and the current which passes through the working electrode, electrolyte and the counter electrode is measured (Fig. 3.4(a)). The control of the cell is performed by a potentiostat (Potentiostat/Galvanostat 263A, Princeton Applied Research). Cyclic voltammetry (CV) (i. e., the repeated scanning of the working electrode potential) is performed to monitor and characterize the desorption of SAMs from working electrode surfaces [69]. The potential windows for the CVs are from 0V to -1.4V vs. SCE. Lower pH solutions are not feasible, as the low desorption potentials of the SAMs (below -1V vs SCE) would have strong interference from the co-evolution of H_2.

3.3 Assembly and electroplating

3.3.1 Lubricant Deposition

Here, we use two kinds of hydrocarbon polymers as lubricants for our experiments: heat curable and UV light curable ones. The heat curable lubricant is composed of 97wt.% triethyleneglycol dimethacrylate (Sigma) as the monomer, and 3wt.% benzoyl peroxide (Sigma) as thermal initiator [75]. This lubricant can be polymerized at 80° for one hour.

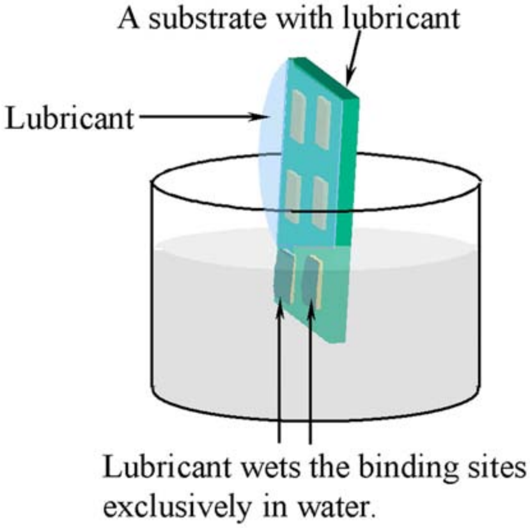

Figure 3.5: A substrate with the lubricant is immersed into water. The lubricant forms droplets exclusively on the binding in water.

The UV curable lubricant is composed of 95wt.% 1,6-hexanediol diacrylate (Aldrich) as the monomer and 5wt.% benzoin methyl ether (Aldrich) as the photoinitiator. To cure this lubricant, we use a UV lamp with the power of 100W and the wavelength of 365nm. The lubricant can be polymerized for an hour by exposure to the UV lamp with intensity of 21mW/cm^2.

As discussed previously, a liquid lubricant meniscus is formed between the component and substrate binding site to create the driving force for assembly. Prior to assembly, the lubricant has to be deposited exclusively on the active (hydrophobic) binding sites on the substrate. To deposit the lubricant, we spread it all over the substrate. The substrate is then slid vertically into water in a petri-dish. Fig. 3.5 illustrates the lubricant deposition step. Due to the high water-SAM interfacial tension compared to lubricant-SAM interfacial tension, the lubricant wets exclusively the SAM-coated binding sites in water. Fig. 3.6 is a schematic plot of the substrate with lubricant.

Another method has been demonstrated by passing the substrate through a thin lubricant film on the water surface, by coating the lubricant exclusively on the binding sites [59].

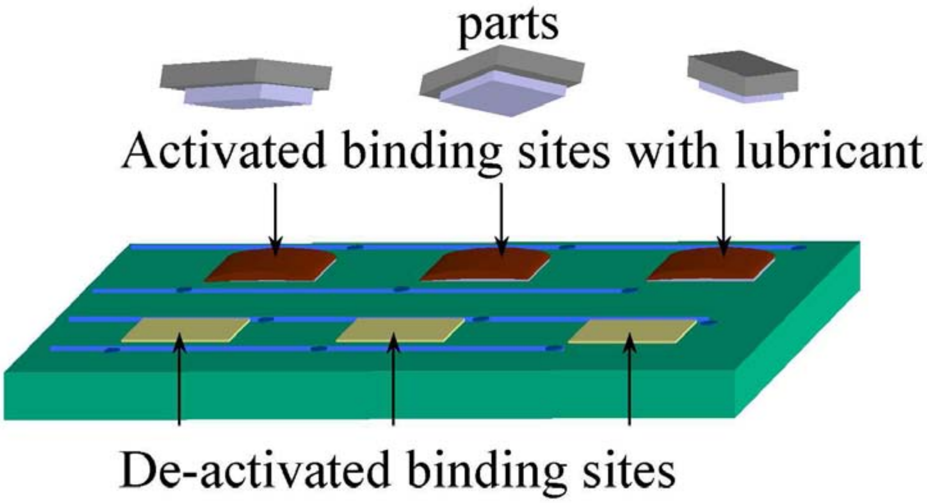

Figure 3.6: Schematic plot of a substrate after the lubricant deposition.

For the second method, the lubricant film has to remain continuous during the sliding process in order for all the binding sites to have uniform lubricant coverage. Therefore, the thickness of the lubricant film on the water surface has to be controlled in order to have a continuous and uniform lubricant deposition.

In previous studies [61], the two lubricants have similar surface tension. To characterize the lubricant, we measure the cured lubricant thickness on different binding sites after deposition. Here, we use the UV light curable lubricant for characterization, as its shrinkage during polymerization is smaller than that of the heat curable lubricant. This is possibly due to the higher temperature during the polymerization process for the heat curable lubricant. We will use the characterization data for surface energy and surface tension force simulation in the next chapters.

3.3.2 Micro part assembly

After applying the lubricant, the micro parts are poured into water as shown in Fig. 3.7(b). With agitation, the assembly takes place exclusively on the hydrophobic areas with lubricant. The agitation is provided either by an orbital shaker or by manual shaking. As soon as the part binding site has contact with a lubricant droplet on the substrate, it is aligned to the substrate binding site by the capillary driving force. The lubricant is then cured and bonds the parts to the substrate. The polymerization process of the heat curable lubricant takes approximately one hour at 80°C in water.

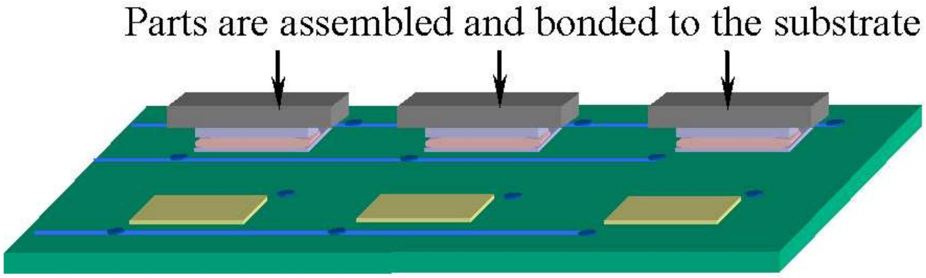

Figure 3.7: Parts are assembled to the binding sites with lubricant and bonded to them after the polymerization of the lubricant.

Here we use a heat-curable lubricant, which can be completely polymerized at 80°C in water after approximately an hour, permanently bonding the parts to the binding sites.

Pictures of assembled square silicon parts and LEDs are shown in Figs. 3.8 and 3.9: a lubricant droplet on a square binding site in Fig. 3.8(a); an assembled square Si part in Fig. 3.8(b) and an array of assembled square Si parts in Fig. 3.8(c); an array of assembled LEDs in Fig. 3.9(a); a zoomed image of an assembled LED in Fig. 3.9(b).

3.3.3 Electroplating to establish electrical connections

Electroplating is used to grow metal from the substrate to the assembled parts. Though physically connected after the lubricant has been cured, the assembled components sometime need to have electrical connections to the substrate as well. An example is that for LEDs in previous work [60], the physical and electrical connections were established together by using a conductive alloy lubricant, where each assembled component has only one electrical connection. Our new method deals with more general cases, where multiple electrical

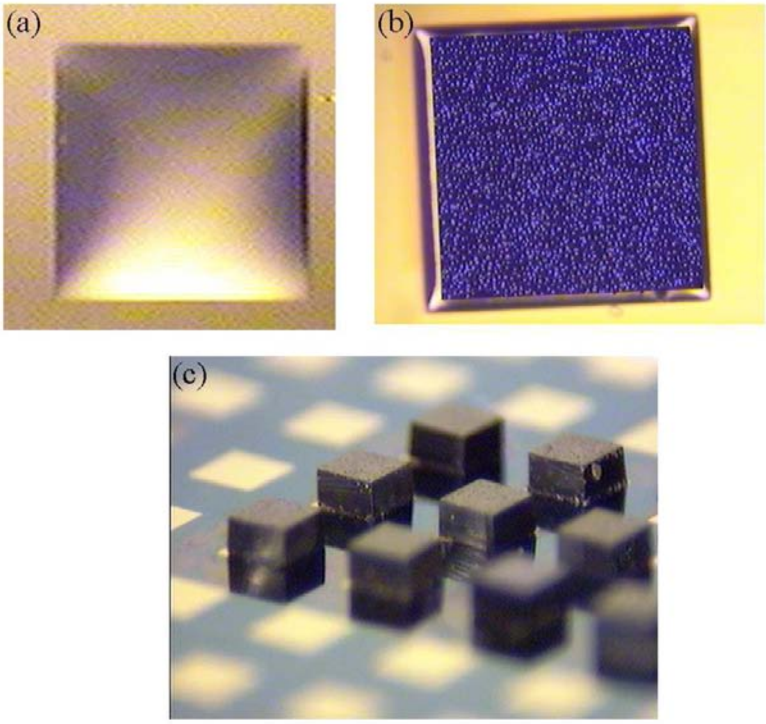

Figure 3.8: Assembled square Si parts permanently bonded on a substrate. (a) Lubricant droplet on a square binding site (b) A square silicon part assembled on the substrate (c) An array of square Si parts assembled. Note that the substrate for (c) has square Au binding sites on a silicon oxide layer without passivation layer.

connections are required. A simple example we use is a packaged commercial LED, which has two electrical connections. Here, we separate the physical and electrical connections by bonding the component to the substrate followed by electroplating to establish electrical connections as illustrated in 3.7. The details of the electroplating method will be discussed in Chapter 6.

Two batch assembly can be achieved by repeating the SAM adsorption and assembly, followed by the electroplating.

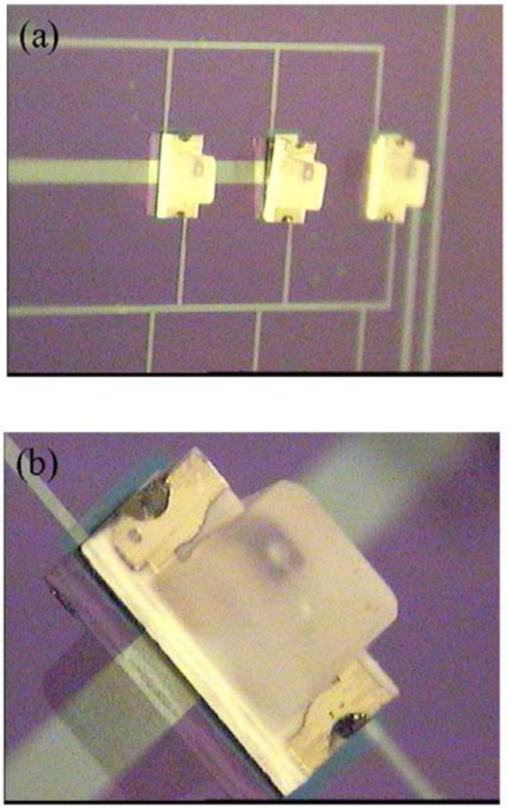

Figure 3.9: Assembled LEDs permanently bonded on a substrate. (a) An array of assembled LEDs and (b) a zoomed image of an LED.

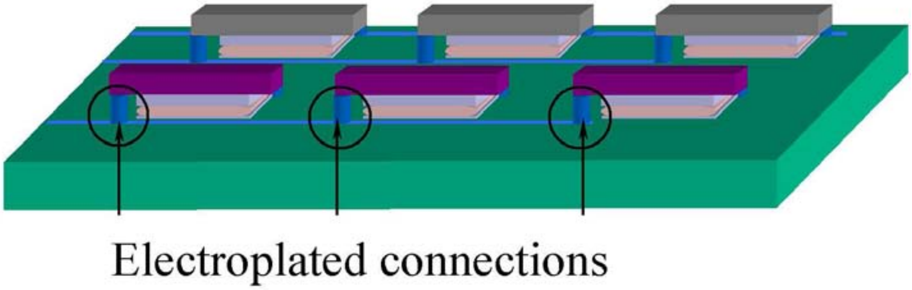

Figure 3.10: Electrical connections between assembled components and the substrate are established by electroplating.

Chapter 4

SURFACE-TENSION DRIVING FORCE MODEL

Surface tension forces have been known as the driving forces many phenomena in nature: soap bubbles, raindrops, liquid rise in a capillary tube etc. Practical applications by using surface tension have emerged. In particular, with recent advances at the micro and nano scale, surface tension has demonstrated the capability of driving actions at such scales for a large variety of applications in adhesion [76]; biology [45, 77]; building microfluidic systems [12,13]; micro printing [48,49] etc. At such scales, the surface tension force becomes more significant at smaller scales compared to gravity, since the surface force scales with dimension squared and the gravity scales with dimension cubed.

Our self-assembly technique is another application that takes advantage of the surface tension force by using it to move and manipulate micro objects. With the assembly part and the substrate binding site patterned with hydrophobic regions, a lubricant meniscus can be formed between the two hydrophobic surfaces in an aqueous environment. If there is any displacement between the two surfaces, the meniscus is stretched and surface energy is increased. To restore the surface energy minimum of the meniscus, surface tension force is created. This force can help the part to be aligned with the binding site in water. To study and understand this process, we dedicate this chapter to the discussion of the surface energy and surface tension force for our self-assembly and self-alignment process.

This chapter starts with some basic concepts and properties of surface energy, which include the discussion of surface energy and surface tension from both microscopic and macroscopic aspects; the relationship between surface tension, pressure and surface geometry: Laplace-Young equation; and a quantitative measurement of surface energy: contact angle. Afterward, we investigate the general problem of surface energy minimization, as self-assembly and self-alignment is the result of the minimization of surface energy. The minimal surface bounded by two coaxial circular shapes is illustrated as the simplest example and an analytical solution for surface minimization is derived: a catenoid surface. For situations other than the catenoid surface, we use a finite element method (FEM) software to simulate the surface energy minimization of the lubricant meniscus and the restoration surface tension forces. The simulation results include the surface energy and alignment forces for assembly with circular and square binding sites.

4.1 Surface energy and surface tension

4.1.1 Microscopic explanation

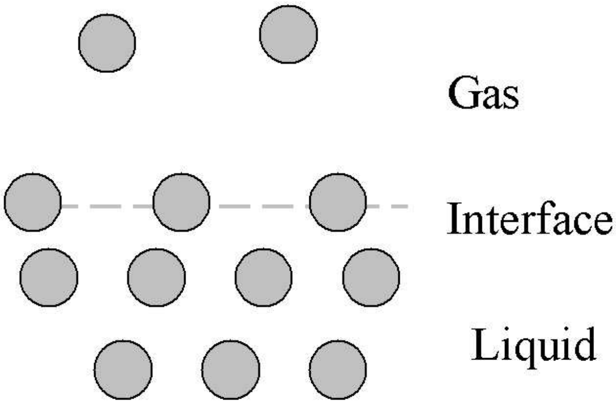

Figure 4.1: Molecular distribution difference at the liquid-air interface.

The difference of the molecular distribution in the bulk and at the interface gives rise to the surface energy and surface tension. The molecules at the interface have a different environment from those in either bulk interior. For example, Fig. 4.1 illustrates the molecular distribution at the liquid-gas interface. The density of molecules decrease from the liquid bulk to the interface and to the gas bulk, and a qualitative plot of the molecular density is shown in Fig. 4.2. As a result, the interaction forces between molecules are different. A molecule in liquid bulk has balanced interactive forces from the molecules in its neighborhood, as its neighbors are symmetrically distributed (Fig. 4.3(a)). The molecules at the interface have stronger interactive forces from the bulk liquid than from the gas bulk due

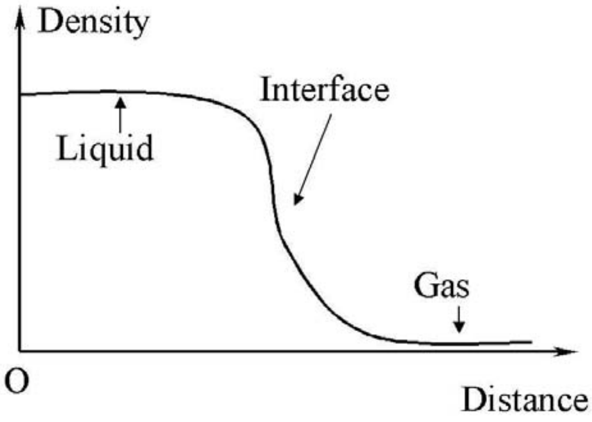

Figure 4.2: Molecular density difference at the liquid-air interface.

to the density difference (Fig. 4.3(a)). From the energy point of view, moving a molecule from the liquid bulk to the surface requires work. To achieve the minimum energy for the system, the interface area has to be minimized, as shown in Fig. 4.3(b). An example of the surface minimization is the spherical raindrop.

This additional energy is the interfacial energy. The surface tension γ is the surface energy per unit area, and it is tangent to the surface. The surface tension for any line on the surface is in the direction perpendicular to the line.

In general, this discussion applies to the interface between two different bulk materials, e.g. liquid-air, liquid-liquid (two immiscible liquids).

4.1.2 Laplace-Young Equation

From the previous discussion, the interface shape is determined by the surface energy. From the macroscopic point of view, the excess pressure p at a point on an interfacial surface relates to the surface curvatures, which is described by the Laplace-Young equation:

$$p = \gamma(\frac{1}{R_1} + \frac{1}{R_2}) \tag{4.1}$$

where R_1 and R_2 are the principal radii of the surface point. The equation can be simply derived as follows. Suppose the normal at point O on a interface is N and the principal radii

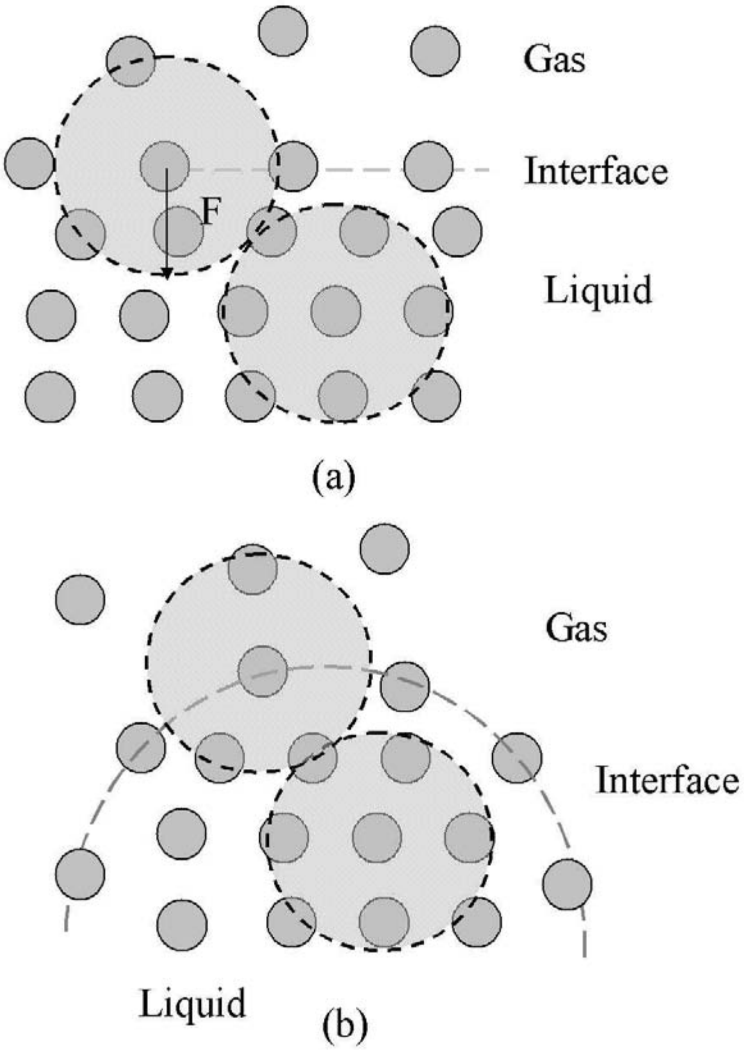

Figure 4.3: (a) The difference of interaction forces on molecules at the bulk and at the interface, if the interface is a plane. The molecules inside the shaded region are those which interacts with the molecule in the center. From the figure, we can see the forces are balanced for the bulk molecule, while the forces are pointing to the bulk for the interface molecule when the forces are attraction forces. (b) The difference of interaction forces on molecules at the bulk and at the interface, when the interfacial area is reduced.

at O are R_1 and R_2 as shown in Fig. 4.4. If we consider a small patch around O enclosed by a circle with radius of r (r is very small), the force on this patch should be zero:

$$F = F_{\text{pressure}} + F_{\text{surf}} = 0 \tag{4.2}$$

The pressure force $F_{pressure}$, which is in the direction of N is :

$$F_{\text{pressure}} = p\pi r^2 \tag{4.3}$$

The surface tension force F_{surf} acts on the perimeter and tangent to the surface. Therefore, at point A on the perimeter (Fig. 4.4), the surface tension force is:

$$\delta F_{\text{surf}} = \gamma r \delta\phi \tag{4.4}$$

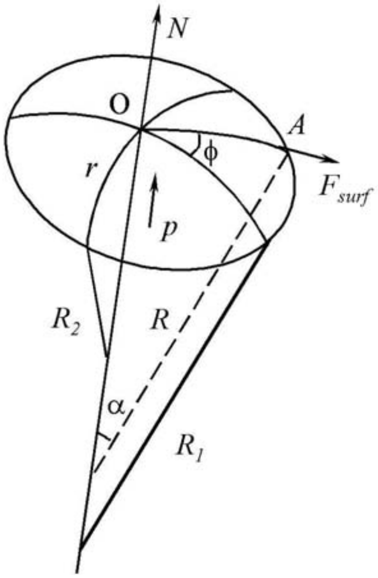

Figure 4.4: A small circular element of an interface centered at point O and with radius r. N is the surface normal and the principal radii are R_1 and R_2, corresponding to the principal curves.

From the illustration in Fig. 4.5, where R is the radius of the curve on the surface passing O and A, the surface tension force F_{surf} projected in the direction of the surface normal can be calculated as:

$$\delta F_{\text{surf\_normal}} = -\gamma r \sin\alpha \delta\phi \tag{4.5}$$

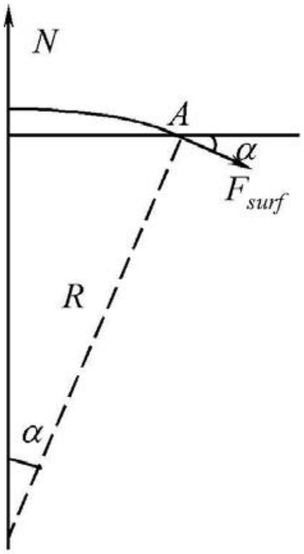

Figure 4.5: A plane passing through the surface normal N and point A. From the geometric similarity, the angle between the surface force F_{surf} and the horizontal direction is the same as the angle between the radius and the surface normal.

As $\sin\alpha = \frac{r}{R}$ and the radius R can be represented in terms of R_1 and R_2 [78], we have

$$\begin{aligned}
\delta F_{\text{surf\_normal}} &= -\gamma r^2 \frac{\delta\phi}{R} \\
&= -\gamma r^2 \delta\phi\left(\frac{1}{R_1}\cos^2\phi + \frac{1}{R_2}\sin^2\phi\right) \\
&= -\gamma r^2 \delta\phi\left(\frac{1}{2R_1}(1+\cos(2\phi)) + \frac{1}{2R_2}(1-\cos(2\phi))\right) \\
&= -\gamma r^2\left(\frac{1}{2R_1} + \frac{1}{2R_2}\right)\delta\phi - \gamma r^2\left(\frac{1}{2R_1} - \frac{1}{2R_2}\right)\cos(2\phi)\delta\phi
\end{aligned}$$

The total surface tension force in the direction of the surface normal can be calculated as:

$$\begin{aligned}
F_{\text{surf\_normal}} &= \int_0^{2\pi} -\gamma r^2\left(\frac{1}{2R_1} + \frac{1}{2R_2}\right)\delta\phi - \gamma r^2\left(\frac{1}{2R_1} - \frac{1}{2R_2}\right)\cos(2\phi)\delta\phi \\
&= \int_0^{2\pi} -\gamma r^2\left(\frac{1}{2R_1} + \frac{1}{2R_2}\right)\delta\phi \\
&= -\pi\gamma r^2\left(\frac{1}{R_1} + \frac{1}{R_2}\right)
\end{aligned} \tag{4.6}$$

From Eqs. 4.3, 4.4, 4.6, we have

$$
\begin{aligned}
&F_{\text{pressure}} + F_{\text{surf\_normal}} = 0 \\
&p\pi r^2 - \pi\gamma r^2\left(\frac{1}{R_1} + \frac{1}{R_2}\right) = 0 \\
&p = \gamma\left(\frac{1}{R_1} + \frac{1}{R_2}\right)
\end{aligned}
$$

Therefore, we have derived the Laplace-Young equation. For the example of a spherical raindrop with the radius of R, the pressure difference inside and outside of the droplet can be calculated as:

$$p = 2\gamma\frac{1}{R} \tag{4.7}$$

4.1.3 Contact angle

An important characteristic of solid surfaces is the *contact angle* denoted by θ. It is an important quantitative measurement related to surface energy. When a liquid rests on a solid surface, the cross-section is shown in Fig. 4.6.

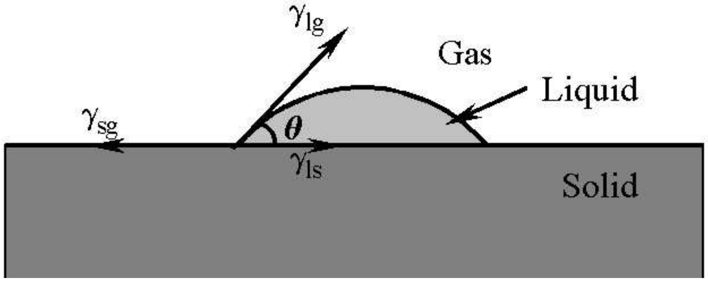

Figure 4.6: An illustration of the surface contact angle. At the intersection between three phases: solid, liquid and gas, the contact angle is between the tangent direction of the liquid surface and the horizontal direction.

The contact angle θ is in the direction tangent to the liquid surface at the intersection of the solid, liquid and gas phases. Since the forces should balance at the intersection point, the surface tensions at the direction of the gas-solid interface should be zero. Suppose the surface tensions between the three phases are denoted as γ_{lg} (liquid-gas surface tension), γ_{ls}

(liquid-solid surface tension) and γ_{sg} (solid-gas surface tension). Therefore, we can derive the value of contact angle with the condition that the horizontal forces balance:

$$\begin{aligned} \gamma_{\text{sg}} &= \gamma_{\text{ls}} + \gamma_{\text{lg}} \cos\theta \\ \cos\theta &= \frac{\gamma_{\text{sg}} - \gamma_{\text{ls}}}{\gamma_{\text{lg}}} \end{aligned} \tag{4.8}$$

Eq. 4.8 is known as *Young's Equation.* A wetting coefficient k is defined as follows to describe the wettability of the solid surface by the liquid:

$$k = \cos\theta = \frac{\gamma_{\text{sg}} - \gamma_{\text{ls}}}{\gamma_{\text{lg}}} \tag{4.9}$$

The solid surface is completely wetted, if $k = 1$; while it is not wetted when $k = -1$.

Hydrophobicity is used to describe the wettability of a solid surface by water. The surfaces can be categorized into two classes: *hydrophilic* when $0 < k \leq 1$ and *hydrophobic* when $-1 \leq k \leq 0$.

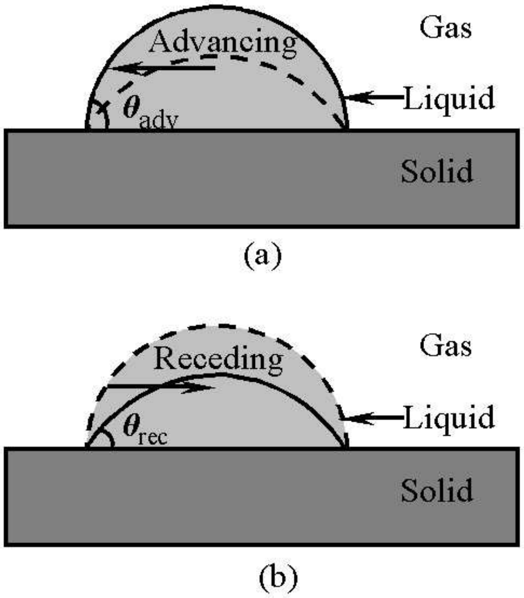

Figure 4.7: Illustrations of the dynamic contact angles: (a) advancing angle and (b) receding angle.

However, in practice, the measured contact angles always show a rather significant variance even though the solid surfaces are of the same materials. One reason is the difference in surface properties: roughness, contamination, etc. Another reason is the measurement method: *advancing* or *receding*. The difference of *advancing* and *receding* is illustrated in Fig. 4.7.

When adding more liquid to a static droplet resting on a surface, the liquid-solid interfacial area will not change simultaneously and therefore the contact angle increases. When a certain angle θ_{adv} is reached, the droplet will spread out and increase the contact area. The receding angle θ_{rec} is the dynamic angle measured when liquid is removed from a static droplet. The difference between θ_{adv} and θ_{rec} might be large.

In our technique, we take advantage of the different surface tensions of different materials. The advancing and receding contact angles of water on different surfaces are measured and shown in Table 4.1.

Table 4.1: Contact angles of water on different surfaces.

Solid surface	Advancing angle (θ_{adv})	Receding angle (θ_{rec})
Au [1]	63°	35°
Au with SAM	93°	69°
Ni	25°	14°
Ni in ethanol [2]	62°	28°
Ni with SAM	56°	31°
Thermal SiO_2	33°	14°

---

[1] Exposure of Au surface to the lab environment even in a short time will cause organic contamination on the surface and therefore increase the contact angle [64]. We store clean Au samples in ethanol. It has been observed the wetting property is different on exposed Au samples and on the samples stored in ethanol. However, during the process of measuring the contact angle, Au from ethanol changed to hydrophobic, and the contact angle obtained is similar to those from Au in air.

[2] Ni surface in air has different contact angle from the samples stored in the ethanol solution, as the exposure in the lab environment might cause contamination on the surface and make the oxidation process easier.

Due to the differences in surface homogeneity, roughness and other surface properties, contact angles might vary even for the same kind of materials.

4.2 Surface energy minimization and surface tension forces

From the surface energy point of view, the stable state is when the surface energy is minimized. It can be modelled as:

Object function to minimize

$$E_{\text{surf}} = \int_A \gamma dA \tag{4.10}$$

Subject to the constraints:

- Integral constraints, e. g. constant volume.
- Boundary constraints, i. e. fixed surface vertices or surface boundaries.

The analytical methods for such minimization problems are from the general area of *calculus of variations*. The simplest example is the one dimensional problem of determining the shortest path connection between two points. An analytical solution can be obtained and it is the straight line connecting between those two points.

In this section, we first discuss using the *calculus of variations* for finding the minimal surfaces with the example of the minimal surfaces bounded by two coaxial circular shapes. With the linear relationship between surface energy and surface area, the minimum area surfaces correspond to the minimum in surface energy as well. Then, we present a brief description of an FEM software *Surface Evolver*, which can be used to find numerical solutions to this minimization problem.

4.2.1 Surface with minimal area: catenoid surface

To illustrate the *calculus of variations* method, we use a two dimensional problem: the minimal surface area bounded by two identical coaxial circular shapes as in [79]. Suppose the radius of the two circular shapes is r, and the distance between them is h, which is shown in Fig 4.8 in a cartesian coordinate system.

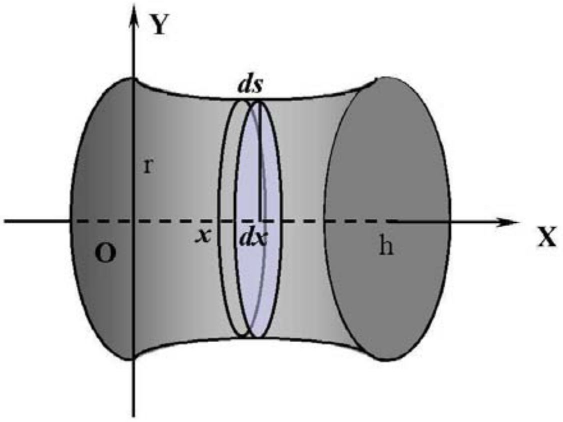

Figure 4.8: A minimal catenoid surface bounded by two identical coaxial circular shapes.

The surface is axially symmetric about axis X and the coordinate in Y is function y(x). The area enclosed by two circles at x and x+dx is:

$$dA = 2\pi y ds \tag{4.11}$$

where ds is the curve length between x and dx and it can be calculated as:

$$ds = \sqrt{1 + y_x^2} dx \tag{4.12}$$

where $y_x = \frac{dy}{dx}$.

Therefore,

$$dA = 2\pi y \sqrt{1 + y_x^2} dx \tag{4.13}$$

The surface area A is the integration of Eq. 4.13 over x:

$$A = \int_0^h 2\pi y \sqrt{1 + y_x^2} dx \tag{4.14}$$

In order to find the minimum surface area, we introduce the *Euler-Lagrange* equation [79]:

Suppose function J is in the form of

$$J = \int_{x_1}^{x_2} f(x, y, y_x)dx \tag{4.15}$$

Then J is an extremum point if

$$\frac{\partial f}{\partial y} - \frac{d}{dx}\frac{\partial f}{\partial y_x} = 0 \tag{4.16}$$

which is called *Euler-Lagrange* equation.

When the partial derivative of f with respect to x equals zero ($\frac{\partial f}{\partial x} = 0$), we can have a simplified *Euler-Lagrange* equation,

$$f - y_x \frac{\partial f}{\partial y_x} = C \tag{4.17}$$

where C is a constant. This equation is also called *Beltrami* identity.

With Eq. 4.14 satisfying the condition for *Beltrami* identity, we can derive that the minimal surface A is achieved when

$$2\pi y\sqrt{1+y_x^2} - y_x \frac{\partial 2\pi y\sqrt{1+y_x^2}}{\partial y_x} = C \tag{4.18}$$

Therefore we have

$$\frac{2\pi y}{\sqrt{1+y_x^2}} = C \tag{4.19}$$

Solving Eq. 4.19, we have

$$y = c_1 \cosh(\frac{x - c_2}{c_1}) \tag{4.20}$$

Such surfaces are called catenoid, as they can be generated by rotation of a catenary curve.

However, Eq. 4.20 is the solution for the minimal surface under certain constraints. For example, when the two disks are far apart, the minimal surfaces will be two discontinuous droplets covering the two disks. We can derive the constraints as follows.

With the boundary conditions at $x = 0, y = r$ and $x = h, y = r$, we can derive $c_2 = \frac{h}{2}$ and the constraint on h and r is

$$r = c_1 \cosh(\frac{\frac{h}{2}}{c_1}) \tag{4.21}$$

To find the relation between r and h, we can simply convert Eq. 4.21 to:

$$rk = \cosh(lk) \tag{4.22}$$

Where $k = \frac{1}{c_1}$ and $l = \frac{h}{2}$.

In Fig. 4.9, we illustrate the relationship between the two functions $f_1(k) = \cosh(lk)$ and $f_2(k) = rk$ with the variable k. Given l, in order for Eq. 4.22 to have solution, the linear function f_2 must be at least tangent to the curve of function f_1. In other words, in this situation, the slope of function f_2 is the smallest of all the feasible rs for Eq. 4.22 to be solvable.

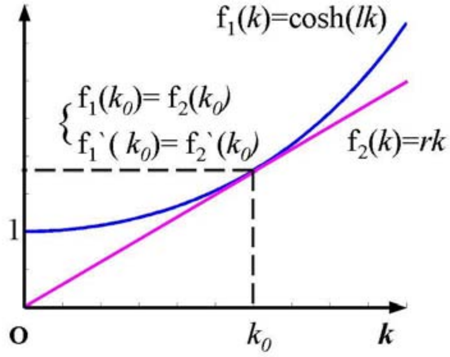

Figure 4.9: The condition of Eq. 4.21 to be solvable: function f_1 is tangent to function f_2.

Therefore, at point k_0 as shown in Fig. 4.9, we have the following equations:

$$\begin{aligned} f_1(k_0) &= f_2(k_0) \\ f_1^{'}(k_0) &= f_2^{'}(k_0) \end{aligned} \tag{4.23}$$

Then we have

$$rk_0 = \cosh(lk_0) \tag{4.24}$$

$$r = l\sinh(lk_0) \tag{4.25}$$

When Eq. 4.24 is divided by Eq.4.25, we have

$$lk_0 = \coth(lk_0) \tag{4.26}$$

Solve Eq. 4.26, we have $lk_0 = 1.19968$. By replacing the lk_0 value in Eq. 4.25, the relation between r and l can be derived as:

$$\begin{aligned} r &= l\sinh(lk_0) \\ \frac{r}{l} &= \sinh(1.19968) \approx 1.50888 \end{aligned} \tag{4.27}$$

Therefore, the condition for the existence of the solutions to Eq. 4.22 is $\frac{l}{r} \leq 0.662743$ and $\frac{h}{r} \leq 1.32549$, which is also the condition for the existence of a minimal continuous surface bounded by two disks with radius of r.

In addition, with

$$\begin{aligned} y &= c_1\cosh(\frac{x-h/2}{c_1}) \\ y_x &= \sinh(\frac{x-h/2}{c_1}) \end{aligned}$$

we can calculate the minimum surface area A from Eqs. 4.14:

$$\begin{aligned} A &= \int_0^h 2\pi y\sqrt{1+y_x^2}dx \\ &= 2\pi\int_0^h c_1\cosh(\frac{x-h/2}{c_1}\sqrt{1+\sinh^2(\frac{x-h/2}{c_1})}dx \\ &= 2\pi\int_0^h c_1\cosh^2(\frac{x-h/2}{c_1})dx \\ &= \pi c_1^2/2(\sinh(\frac{2(x-h/2)}{c_1}) + 2\frac{x-h/2}{c_1}) \mid_0^h \\ &= \pi c_1^2\left(\sinh(\frac{h}{c_1}) + \frac{h}{c_1}\right) \end{aligned} \tag{4.28}$$

The volume V of the lubricant bounded between the hydrophobic surface is:

$$\begin{aligned} V &= \int_0^h \pi y^2 dx \\ &= \pi \int_0^h c_1^2 \cosh^2(\frac{x-h/2}{c_1}) dx \\ &= \pi c_1^2 \int_0^h \frac{1+\cosh(\frac{2(x-h/2)}{c_1})}{2} dx \\ &= \frac{\pi c_1^2}{2}\left(h + c_1 \sinh(\frac{h}{c_1})\right) \end{aligned} \tag{4.29}$$

where c_1 is determined by Eq. 4.21 on the condition that $\frac{h}{r} \leq 1.32549$.

From Eq. 4.28 and 4.29, we obtain the relation between the volume and area of a catenoid surface:

$$V = \frac{c_1 A}{2} \tag{4.30}$$

Suppose volume V and radius r are given as the boundary conditions, we have the equation array:

$$\begin{cases} r &= c_1 \cosh(\frac{\frac{h}{2}}{c_1}) \\ V &= \frac{\pi c_1^2}{2}\left(h + c_1 \sinh(\frac{h}{c_1})\right) \end{cases} \tag{4.31}$$

There is no analytical solution to Eqs. 4.31. With given V and r, numerical solutions can be obtained, and the minimal surface A and the optimal lubricant thickness h can be calculated.

The catenoid surface is the simplest case for the minimal surface problem. In most of the cases, analytical solutions to the minimal surface problem, e.g. the *Euler-Lagrange* equation (Eq. 4.16), might not exist. For example, when the two disks are non-coaxial, there might not be analytical solutions [79]. Therefore, a numerical method is used to find the minimal surface, which is investigated in the next section.

4.2.2 Surface energy minimization with Surface Evolver

For most of the surface minimization problems, we cannot obtain analytical solutions as the catenoid surface discussed in the previous section. Therefore, we use a software called *Surface Evolver* for self-assembly process simulations. By "evolving" the surfaces along the energy gradient, the surface energy decreases and the minimum can be found. The software is implemented by using different energy gradient search methods: gradient descent, conjugate gradient or Hessian methods. In addition, the surface tension force or torques can also be derived as the energy derivative. In *Surface Evolver*, there are five different methods to calculate the force [80, 81]: finite differences, principle of virtual work by finite differences, principle of virtual work using Lagrange multiplier, variational formulation and explicit forces.

All the methods except the last one calculate the forces as the derivatives of surface energy with respect to the displacement, while the force is calculated directly in the last method. In [81], the advantages and disadvantages of difference methods are discussed, and comparisons of them are also presented.

However, such numerical methods might end up with solutions of local energy minima instead of the global one. To avoid reaching a local minimum, we must choose the initial condition close to the optimal solutions.

In the following section, we calculate the surface energy and surface tension forces by using *Surface Evolver*. Due to the time efficiency and the simplicity of data preparation of the principle of virtual work using Lagrange multiplier, we use it to calculate the surface tension forces.

4.3 Finite element simulation of surface energy and forces for self-assembly

In the surface tension driven self-assembly process, the lubricant is confined between two hydrophobic surfaces in an aqueous environment. The surface tension force created from the lubricant-water interface drives the movement of the part, till the surface energy minimum is reached.

Fig. 4.10 illustrates different steps in the self-assembly and self-alignment process. When a part with hydrophobic binding site touches a lubricant droplet on a substrate binding site (Fig. 4.10(a)), the lubricant will spread on the part binding site and completely wet it (Fig. 4.10(b)). The surface of the part is wetted by the lubricant, because the lubricant energetically favors the hydrophobic surface compared to water. With the minimization of water-lubricant surface energy, the part is attracted towards the binding site (Fig. 4.10(c)) until they are aligned and the minimum energy is reached (Fig. 4.10(d)).

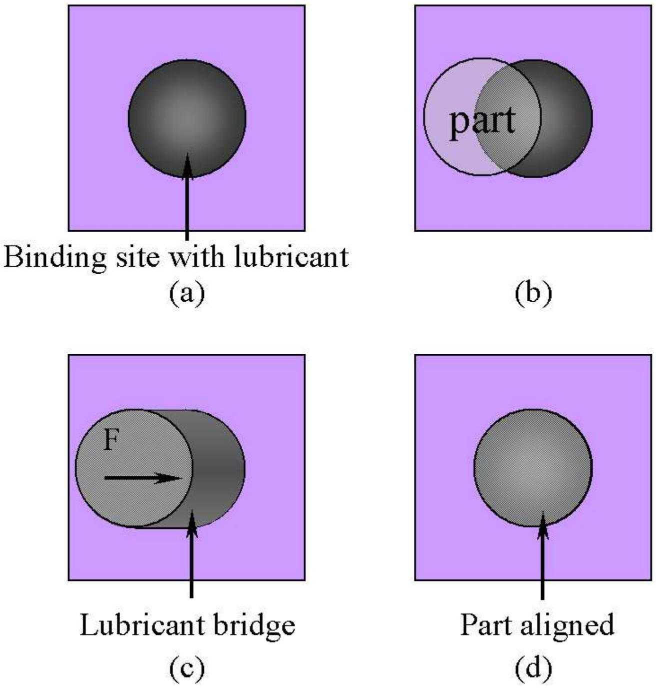

Figure 4.10: An illustration of the self-assembly and self-alignment process. (a) A substrate binding site with a lubricant droplet. (b) A part touches the droplet. (c) The droplet spreads on the surface of the part and forms a bridge between the part and the substrate binding site. (d) The part is aligned to the substrate binding site.

To analyze the self-assembly process, we have the following assumptions:

- We always assume the lubricant wets both the part surface and the substrate binding site.
- We consider the self-assembly as a quasi-static process with no friction, inertia effects ect.

To study the self-assembly process, we can calculate the lubricant-water interfacial energy for each position of the part during the movement, as well as the surface tension restoration forces. We study two different binding site shapes: disk and square in the following sections.

4.3.1 Circular binding sites

When the binding sites are disks, the model for surface energy is similar to the minimal catenoid surface. When the part is not aligned with the substrate binding site, the two disks are not co-axial and the lubricant-water interface might not be catenoid. Therefore, we use *Surface Evolver* to calculate the surface energy and surface tension force.

To obtain the information for the lubricant droplet (thickness, volume, contact angle etc.) on the binding site, we measure the lubricant thickness after it is polymerized. Figs. 4.11 show the polymerized lubricant on 500μm binding sites.

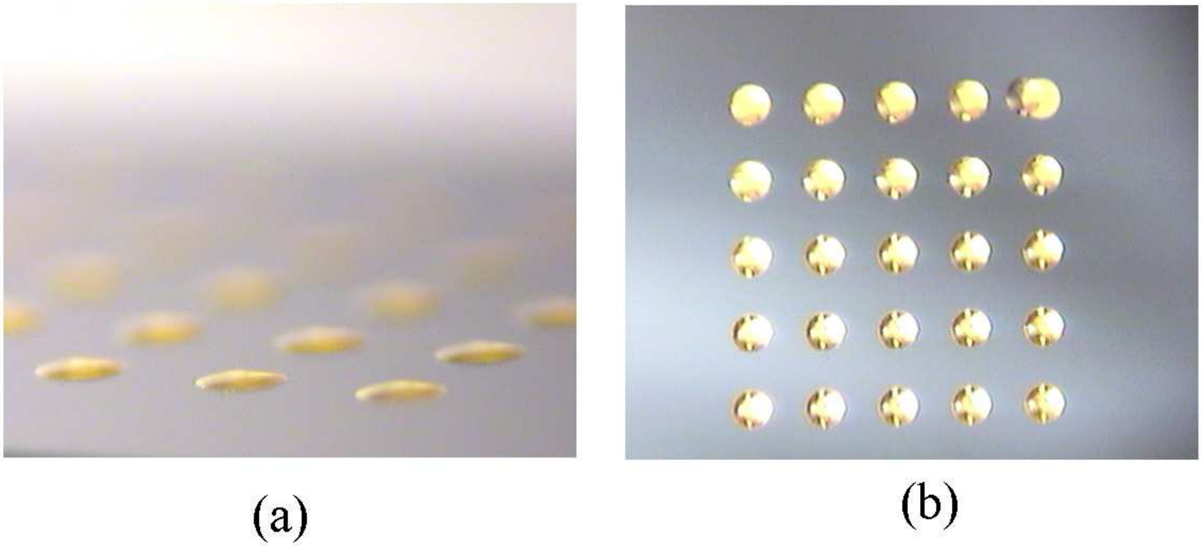

Figure 4.11: Polymerized lubricant on 500μm circular binding sites: (a) Side view shows the contact angle of the lubricant on the binding site is small (less than 90°). (b) Top view of the lubricant droplets.

We can calculate the contact angle of lubricant on the binding site in water from the lubricant thickness. Suppose the lubricant droplet is a spherical cap. From the contact angle illustration in Fig. 4.12, we have

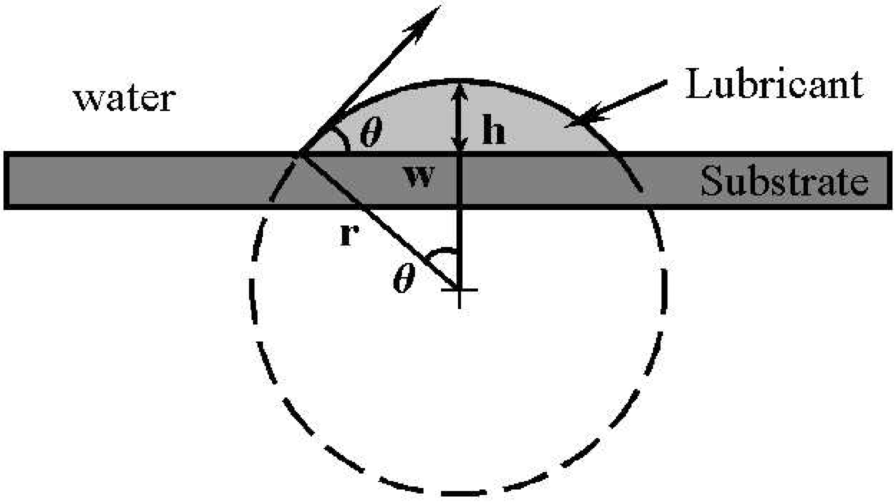

Figure 4.12: A plot of the relationship between the contact angle, binding site width w and droplet height h.

$$\begin{aligned} r\sin\theta &= \frac{w}{2} \\ r\cos\theta &= r-h \end{aligned} \tag{4.32}$$

Therefore,

$$\begin{aligned} \frac{2h}{w} &= \frac{1-\cos\theta}{\sin\theta} \\ \frac{2h}{w} &= \frac{\sin(\frac{\theta}{2})}{\cos(\frac{\theta}{2})} \\ \theta &= 2\arctan(\frac{2h}{w}) \end{aligned} \tag{4.33}$$

With the averaged lubricant thickness on these binding sites being 41μm, the contact angle is approximately 19°. From Eq. 4.8, the lubricant-water surface tension γ_{wl} can be estimated as

$$\gamma_{wl} = \frac{\gamma_{ls} - \gamma_{ws}}{\cos\theta} \tag{4.34}$$

where γ_{ws} $\approx$46mJ/m^2 is the surface tension between lubricant and SAM-coated binding site, and γ_s $\approx$1mJ/m^2 is the surface tension between water and the SAM-coated binding site. The lubricant-water interfacial energy can be estimated to be γ_{wl} $\approx$50mJ/m^2.

The volume of the lubricant on a circular binding site can be derived in terms of r and h as follows:

$$V = \frac{\pi h(3r^2 + h^2)}{6} \tag{4.35}$$

With r=250μm and h=41μm, the volume is V=4.1× 10^{-3}mm^3. We can calculate the surface energy and surface tension forces during the self-alignment process by using *Surface Evolver.*

Suppose the lubricant volume does not change during the process, the lubricant is insoluble in water and the shrinkage of the lubricant during polymerization process is negligible, the volume will be the constraint for the optimization. To find the restoration force at a certain displacement of the part, the simulations are carried out in two steps as shown in Fig. 4.13:

- With the lateral displacement of x, the part has an optimal vertical position, at which the vertical restoration force is zero. We search a range of vertical positions and calculate the restoration force by *Surface Evolver* until the optimum is found (Fig. 4.13(a)).

- At the optimal vertical position, the lateral restoration force is calculated as the derivative of surface energy by using *Surface Evolver.*

When the part is at zero lateral displacement with the binding site, we simulate the surface energy and surface tension force with respect to the vertical displacement, which is plotted in Fig. 4.14. From the numerical simulation with r=250μm and V=4.1× 10^{-3}mm^3, we can obtain that the minimum surface has area and energy of approximately 0.0330609mm^2 and 1.6530nJ respectively, when the part vertical displacement (lubricant thickness) is

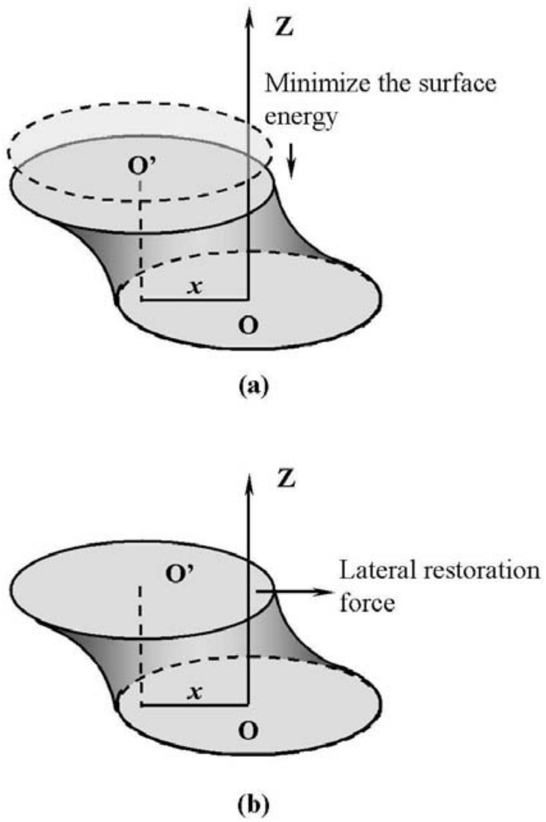

Figure 4.13: The two steps of simulation for each pose of the part: (a) finding the optimal vertical displacement of the part; (b) calculation of the surface energy and restoration force.

0.021094mm. This minimal surface is a catenoid surface. As discussed in the previous section, this minimal surface can also be determined by solving Eqs. 4.31, with given r=250μm, h=41μm and V=4.1× 10^{-3}mm^3. Table 4.3.1 shows a comparison between the results derived from the two different methods: *Variational Calculus* and *Surface Evolver*.

By repeating the calculations of the surface energy and lateral surface tension forces for different part lateral displacements, we can obtain the surface energy (Fig. 4.15(a)) and the restoration forces (Fig. 4.15(b)). Fig. 4.15(c) shows how the vertical displacements of the part change with lateral movements of the part.

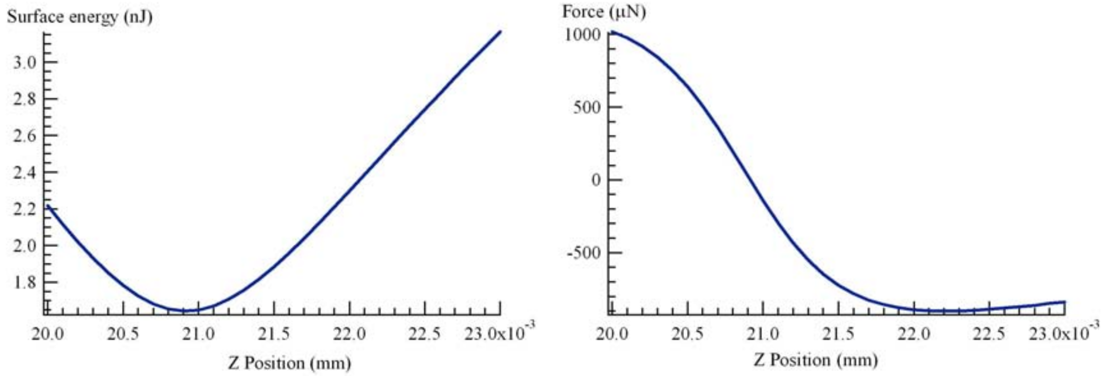

Figure 4.14: The simulation results of surface energy and lateral forces calculated by *Surface Evolver*. When the part has no lateral displacement with the binding site, (a) surface energy and (b) surface tension force with respect to the part height. The binding site is disk with the radius of 500μm.

Table 4.2: Comparison of minimal surface results from different methods: analytical solutions from *Variational Calculus* and numerical solutions from *Surface Evolver*.

Methods	Vertical displacement	Interfacial area	Interfacial energy
Variational Calculus	0.020906mm	0.0328287mm^2	1.6414nJ
Surface Evolver	0.021094mm	0.0330609mm^2	1.6530nJ

4.3.2 Square binding sites

We also use square binding site for our experiment. An array of polymerized lubricant on square binding sites is shown in Fig. 4.16. To calibrate the lubricant volume deposited on a square binding site, we use a surface profiler (P15, Tencor) to characterize the morphology of the cured lubricant on one binding site (Fig. 4.17). The peak point height of a cured lubricant droplet is 62.1μm, and the volume of the droplet is calculated to be 0.033mm^3.

For square binding sites, the restoration torque due to the misalignment in orientation has to be calculated in addition to the lateral restoration forces. The simulations results include:

- The relation between the surface energy and vertical surface tension force with respect to the vertical displacement of the part, which is shown in Figs. 4.18(a) and (b).

- When the part has lateral misalignments (Fig. 4.19(a)), the vertical displacements of the part, the surface energy and lateral restoration forces with respect to the lateral displacement x of the part are shown in Fig. 4.19(b), (c) and (d) respectively.

- When the part has orientational misalignments (Fig. 4.20(a)), the vertical displacements of the part, the surface energy and lateral restoration forces with respect to the relative orientation α of the part are shown in Fig. 4.20(b), (c) and (d) respectively.

By simulation, we can estimate the optimal height of the part with respect to the binding site is $\approx$0.032951mm and the minimal surface energy is 6.5967nJ with the volume V=0.033mm^3 and the binding site size of is 1×1mm^2.

4.4 Summary

In this chapter, we have explained the surface energy and surface tension force from the microscopic point of view. The minimization of surface energy was modelled, and an analytical solution of minimal surface between two coaxial disks has been derived. FEM simulations are used to calculate the surface energy and surface tension forces for our self-assembly step.

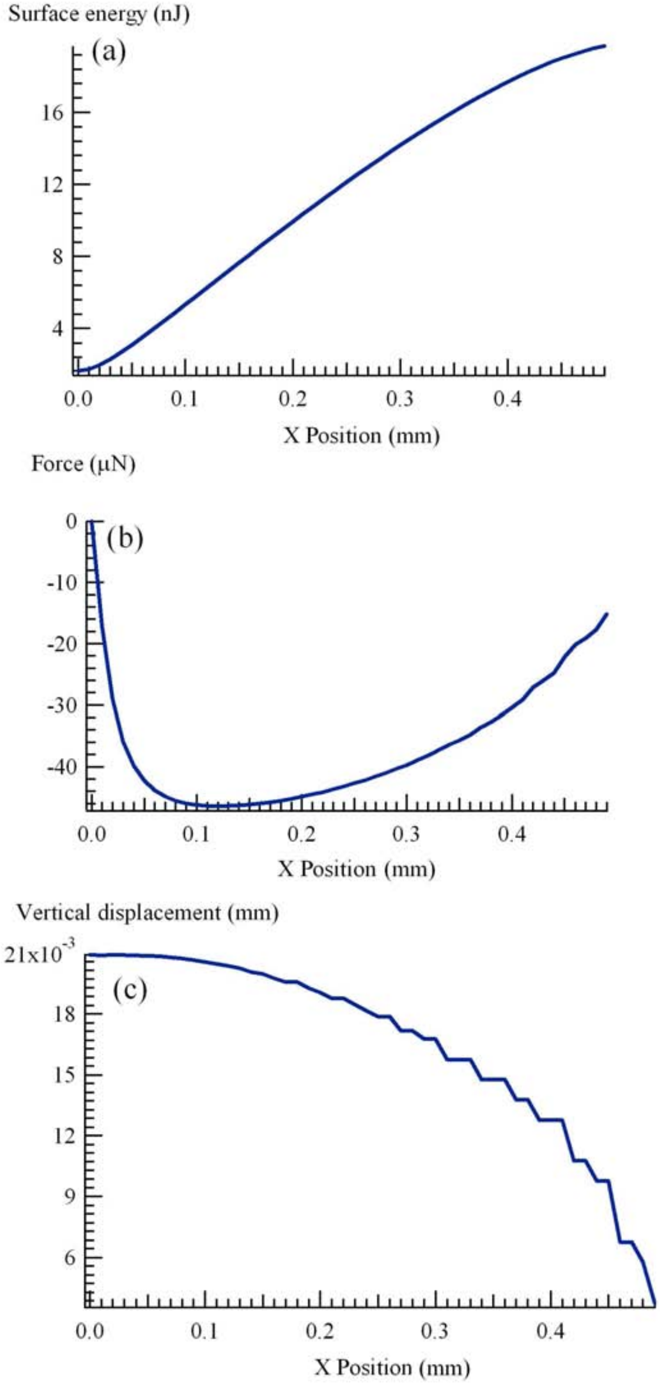

Figure 4.15: *Surface Evolver* simulation results: (a) surface energy, (b) lateral restoration forces and (c) vertical displacements of the part with respect the lateral displacements of the part. The binding site is disk with diameter of 500μm.

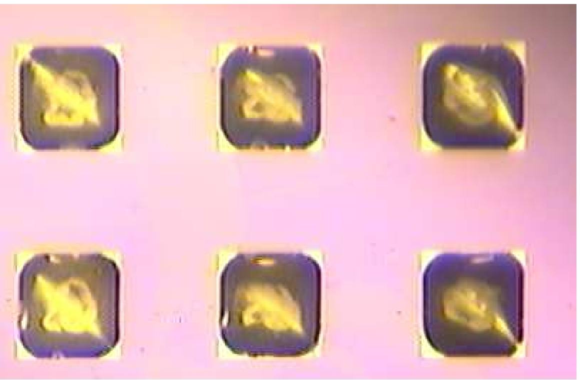

Figure 4.16: A substrate with an array of binding sites with cured lubricant. The lubricant is deposited exclusively on the binding sites.

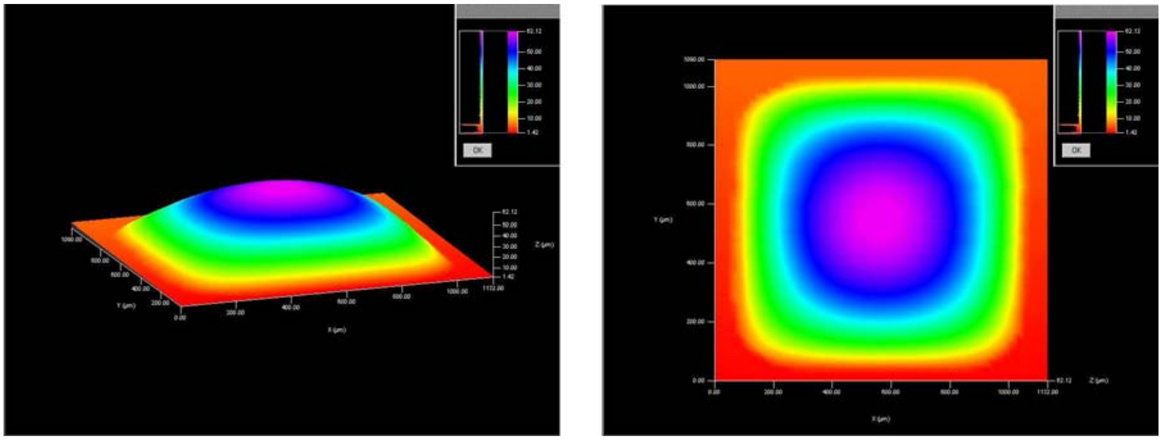

Figure 4.17: Surface topograph of a lubricant droplet on a 1×1mm^2 square binding site. (a) Side view of surface profile of the lubricant droplet. (b) Top view of the surface topology, and different gray scales indicate different surface heights.

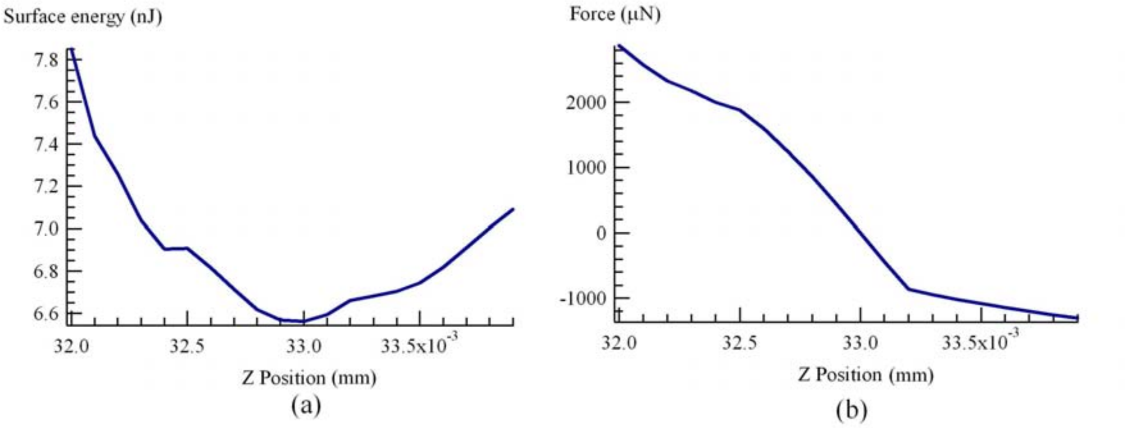

Figure 4.18: When the part has no lateral displacement with the binding site, (a) surface energy and (b) surface tension force with respect to the part height can be calculated by *Surface Evolver* . The binding site is 1×1mm^2 square.

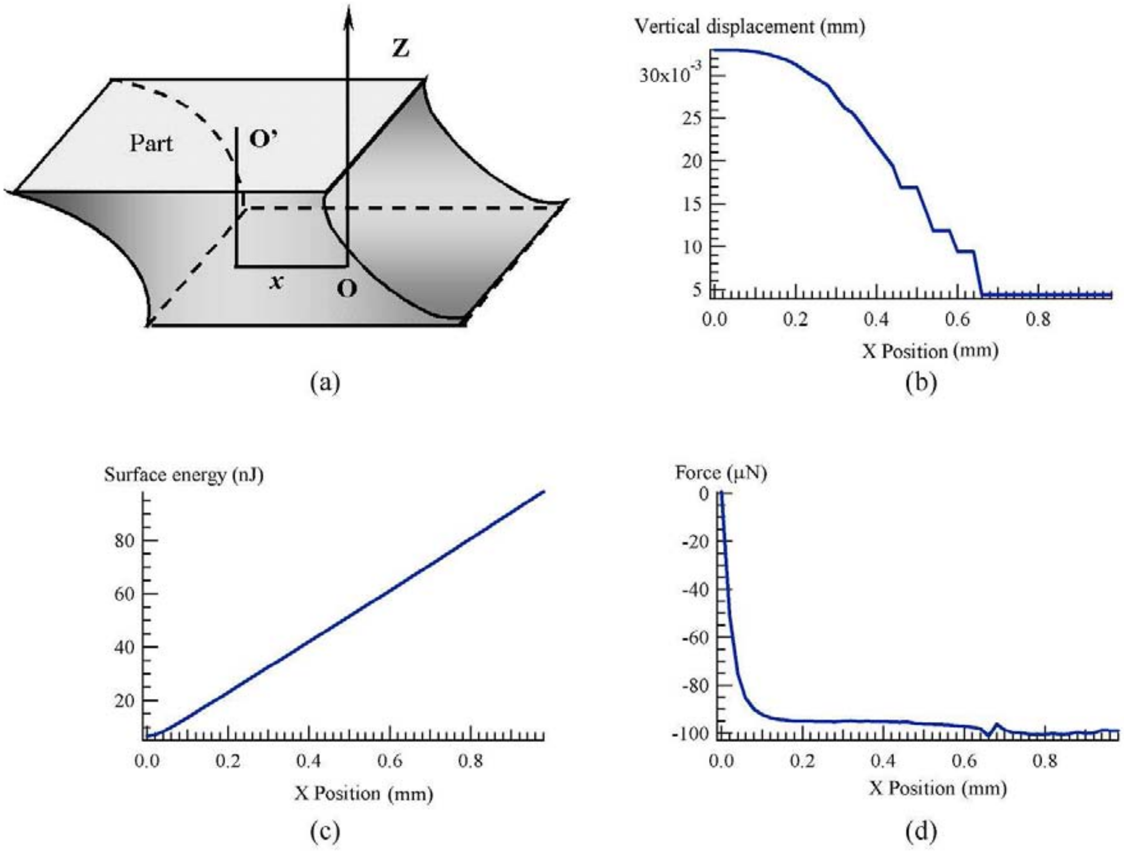

(a) (b)

(c) (d)

Figure 4.19: (a) An illustration of the lateral misalignment x. (b) vertical displacements of the part, (c) surface energy and (d) restoration forces with respect the lateral displacements of the part. The binding site is $1{\times}1\text{mm}^2$ square.

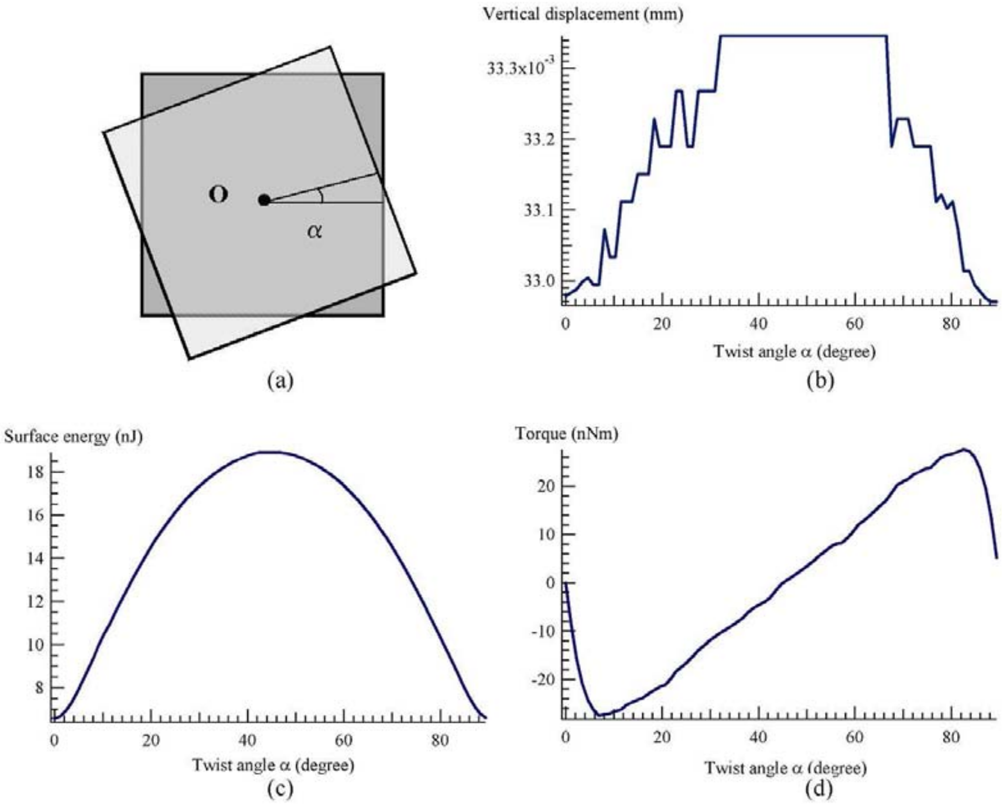

Figure 4.20: (a) An illustration of the misalignment in orientation. The relative orientation between the part and the substrate binding site is α, though their centers coincide. Simulation results by *Surface Evolver*: (b) Vertical displacements of the part, (c) surface energy, and (d) restoration torques with respect to the relative orientations of the part, respectively. The binding site is $1{\times}1\text{mm}^2$ square.

Chapter 5

BINDING SITE GEOMETRY DESIGN

The driving force for self-assembly is provided by a liquid lubricant meniscus confined between two hydrophobic surfaces in an aqueous environment. The shape of the binding site plays an important role in the assembly. So far, most self-assembly experiments have been performed only with specific devices of symmetric binding sites with no preference in orientation, e.g.unpackaged square GaAs/GaAlAs LEDs and mirrors [54, 59, 60]. The final alignment between the part and the substrate binding site will not be unique: for example, the square part has four different possible alignments 90° apart in orientation. Therefore, to achieve best alignment, the hydrophobic pattern design becomes a critical issue for the self-assembly process. With an optimal design, the part can assemble in a unique position and orientation.

In this chapter, we discuss a constructive method to design binding site geometry. First, we introduce a first-order approximation model of the interfacial energy. Based on the model, we can calculate the driving forces or torques for assembly at much smaller computational expense. A series of geometric shapes including disks, symmetric rings and asymmetric rings with non-concentric inner cutout are studied. From the energy and force (torque) analysis, a constructive optimization method is used to find optimal binding site shapes. As the result, optimal symmetric ring shapes ensuring unique alignment position, and asymmetric rings ensuring unique alignment position and orientation, are obtained.

5.1 First order approximation model

In this section, we introduce a first order approximation model for calculating the surface energy. Due to its computational simplicity, this method is preferable, e.g. compared to using the three-dimensional finite element method (FEM) software *Surface Evolver*.

A brief derivation of the model is described as follows. With the assumption that shift

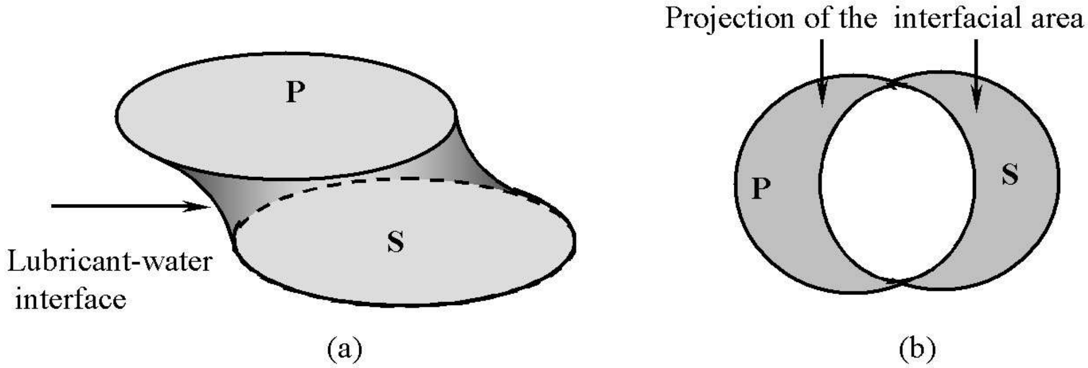

Figure 5.1: (a) Cross-section of the lubricant-water interfacial area. (b) The projection of the interfacial area to the substrate plane is shown as the shaded area. Note the lubricant thickness has been exaggerated.

between the part (P) and the substrate binding site (S) is much larger than the lubricant thickness, the water-lubricant interfacial area (Fig. 5.1(a)) can be approximated by its projection to the substrate plane shown as shaded areas in Fig. 5.1(b). Due to the linear relationship between the interfacial energy and area, we can approximate the interfacial energy E by the projection area (Fig. 5.1(b)):

$$E = \gamma(\mid S \mid + \mid P \mid -2 \mid S \cap P \mid) \tag{5.1}$$

where $\mid P \mid$, $\mid S \mid$ and $\mid S \cap P \mid$ denote the part area, the substrate binding site area and their overlap areas respectively, and γ is the lubricant-water interfacial tension.

Simulation results from the two different methods for a 500μm disk and a $1{\times}1$mm^2 square are shown in Figs. 5.2 and Figs. 5.3. Both the surface energy and force results demonstrate good accordance between the approximation model and the three-dimensional FEM (*Surface Evolver*), as long as the displacement between the part and the substrate binding site is larger than the lubricant thickness. Fro smaller displacements, this model overestimates the alignment forces. A quadratic model provides more accuracy in this range.

This model enables the designer to efficiently estimate the energy of a system where the meniscus is confined to the overlap of the two hydrophobic areas.

To briefly describe the implementation of the simulation tool, the overlap area called

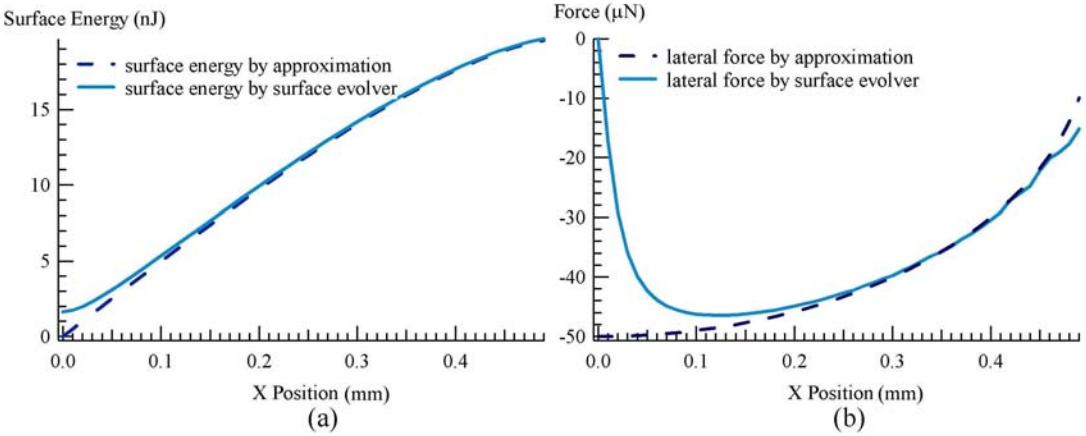

Figure 5.2: Simulation results from the approximation model and *Surface Evolver* for 500μm circular binding site: (a) Surface energy and (b) lateral surface tension force. Here we use γ=50mJ/m^2 and the lubricant volume is 0.0041mm^3.

$A(x, y, \alpha)$ is computed with respect to three parameters, representing the relative location (x, y) and orientation α of P with S. For a given orientation α, the value A can be calculated efficiently by two-dimensional convolution of P to S. To characterize the overlap area as a function of the rotation angle, calculations are iterated for discretized α values in the range from 0° to 360°. Therefore, for a binding site design, we use two plots to show the simulation results: translation and rotation. In the translation result, the overlap ratio, which is the ratio of the overlap area to part binding site area ($\frac{|S \cap P|}{|P|}$), is plotted as a function of relative location (x, y) of P to S. In the rotation result, each point in the plot corresponds to a maximum overlap ratio with respect to a given orientation β. An example of the simulation of a square pattern is shown in Fig. 5.4. A comparison between simulation and experimental results of different binding site designs is investigated in [82].

In the case when the parts have a pre-determined design, we have to decide what is the optimal design for the binding site on the substrate. For example, the binding site design for assembly of the off-shelf LEDs with the hydrophobic pattern shown in Fig. 5.5(a) is not straightforward. If we choose the substrate binding site the same as the LED's (Fig. 5.5(b)), the simulation results in Fig. 5.5(c),(d) show several local overlap maxima, which correspond

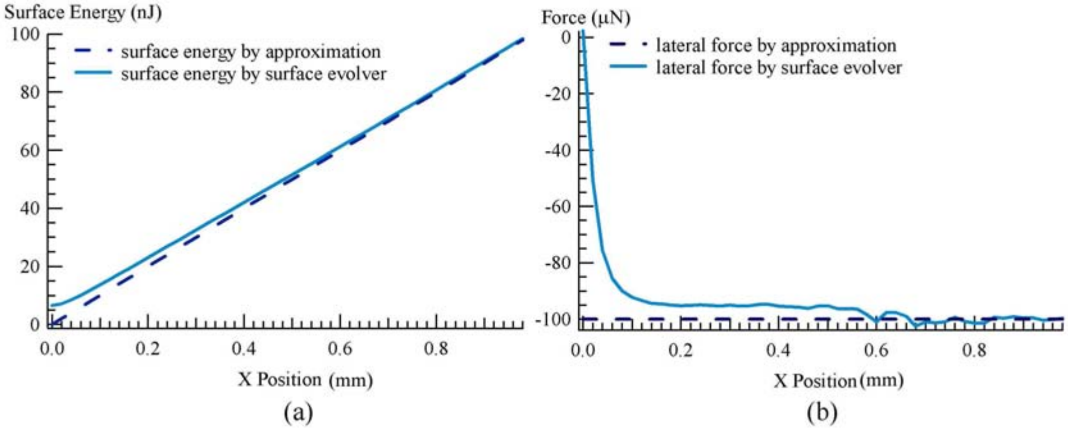

Figure 5.3: Simulation results from the approximation model and *Surface Evolver* for $1{\times}1\text{mm}^2$ square binding site: (a) Surface energy and (b) lateral surface tension force. Here we use γ=50mJ/m^2 and the lubricant volume is 0.033mm^3.

to energy minima. An improved design is shown in Fig. 5.5(e), which has openings in the top-left and right-bottom corners for post-assembly processing. It has no local maximum in the translation result (Fig. 5.5(f)). The minima in the rotation result at 180°, shown in (Fig. 5.5(g)), can not be avoided due to the given LED symmetry design.

The experimental result in Fig. 5.6(a) shows the LED stuck at the position as indicated in the simulation (Fig. 5.5(c)), when using the design in Fig. 5.5(b). Fig. 5.6(b) is an assembled LED on the improved binding site shown in (Fig. 5.5(e)).

In summary, the simulation results accord with the experimental results. The simulation tool can be employed to efficiently evaluate designs for assembly experiments in order to improve the assembly results.

5.2 Geometric pattern design for hydrophobic binding sites

In this section, we discuss the binding site optimization and binding site design methods, by using the first order approximation model. Ideally, an optimal pattern would have a unique assembly location including position and orientation, which corresponds to a unique energy global minimum. Based on the first order model, such an ideal pattern will have a unique

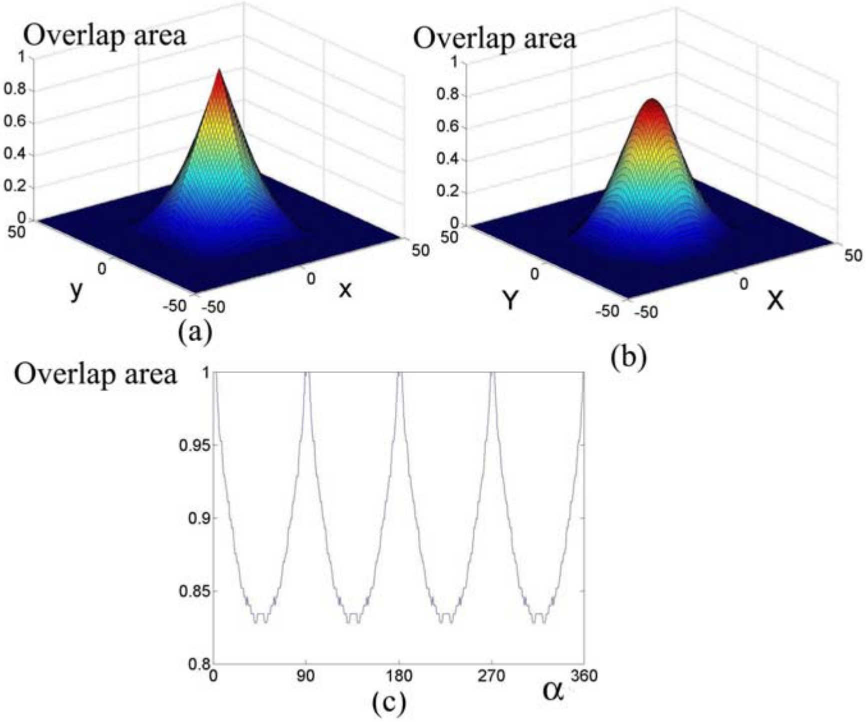

Figure 5.4: Simulation results for the square pattern. (a) Translation simulation of two squares with relative orientation of 0°. (b) Translation simulation of two squares with relative orientation of 45°. (c) Rotation simulation of two squares.

maximum overlap area.

First, we introduce some terminology that will be used in the paper:

- Position (b, β) denotes where the part is in a polar coordinate system.
- Orientation (α) is the angular difference of a part with respect to a reference frame.
- Pose (b, β, α) denotes both the position and orientation
- Position alignment (Δb, $\Delta\beta$) is the relative position of a part to a binding site.
- Orientation alignment ($\Delta\alpha$) is the relative orientation of a part to a binding site.
- Alignment (Δb, $\Delta\beta$, $\Delta\alpha$) is the relative pose of a part to a binding site

For convenience, we use the substrate binding site center as the origin. Therefore, the pose of the part and its alignment have the same value (b, β, α).

There are different ways to design such patterns as follows:

- Pattern design for a given part. When the assembly parts have special requirements and the part binding site cannot be chosen freely, we have to find the design which offers the least number of local maxima. An example is the LED binding site design, discussed in the previous section.
- Heuristic design. An asymmetric "swirl" design has been presented in [83]. By using the first order simulation tool, we have found that there is a unique overlap maximum in all the poses of the part.
- Site design by exhaustive search. A systematic search of the entire design space is performed and an optimal design is found based on evaluations of all the designs searched. Complexity of this algorithm is exponential in the resolution of the discretization. It is computationally expensive and slow, and only approximated solutions are found because of discretization.

- Site design by using composite geometric shapes, formed by simple shapes as circular, square, triangular etc. Simple geometric shapes usually have more than one overlap area maximum in all the poses. For example, two identical hydrophobic square shapes have four maxima in overlap area at the relative orientations of $0°$, $90°$, $180°$ and $270°$. Two identical circular shapes have maximal overlap area at the coincidence of their centers, no matter of their relative orientation. However, composition of simple shapes would generate a design with unique maximal overlap areas. Compared to the previous methods, this method is simple and easy to implement, however we cannot find all the possible optimal shapes by using this method.

In the following sections, we will focus on the last method. Particulary, composite patterns with circular shapes of different sizes are used to create optimal designs.

5.3 Geometric analysis of composite ring shapes

For simplicity of analysis, we investigate rings constructed from the set difference of two disks as examples to study optimal shape design. As the disk-disk intersection area depends exclusively on the disk center distance, the ring-ring overlap area can be obtained in closed-form. From the analytical results of rings, we can derive the general design rules for the construction of optimal shapes.

A ring geometry can be simply defined as the subtraction of a smaller circular shape from a bigger one. We will introduce some basic definitions and operations as follows.

5.3.1 Basic shapes

Definition 5.3.1 *Disk: a disk shape is defined as* $D(c, r)$ *with center* c *and radius* r*.*

Definition 5.3.2 *Ring: a generalized ring is defined as* $R(D_b, D_s)$ *with outer bigger disk as* D_b *and inner circular cutout as* D_s*.*

The parameters for rings include (r_b, r_s, a), with r_b and r_s as the radii of D_b and D_s respectively, and the offset $a = || c_b - c_s ||$ denoting the distance between the centers of the disks. As the small disk has to be included in the large one, the condition $r_b \geq r_s + a$ must be satisfied. A generalized ring is shown in Fig. 5.7.

When offset $a = 0$, i.e. $C_b = C_s$, the rings are referred to as symmetric rings. Otherwise they are called asymmetric rings.

5.3.2 Disk-disk overlap area and its derivatives

Definition 5.3.3 *Overlap Area $A(D_1, D_2)$ denotes the overlap area between disks D_1 and D_2.*

The overlap area between two disks with their radii of r_1 and r_2 respectively, depends only on the distance $b = \| c_1 - c_2 \|$ between their centers. As shown in Fig. 5.8, the overlap area is the addition of two lens-shapes.

Suppose the two circular shapes are D_1 and D_2 with their radii of r_1 and r_2 respectively, then the intersection area can be calculated as:

Proposition 5.3.1

$$A(D_1, D_2) = \begin{cases} 0 & b \geq r_1 + r_2 \\ -\frac{\sqrt{(-b+r_1+r_2)(b+r_1-r_2)(b-r_1+r_2)(b+r_1+r_2)}}{2} & \\ +r_1^2 \arccos(\frac{b^2+r_1^2-r_2^2}{2br_1}) + r_2^2 \arccos(\frac{b^2+r_2^2-r_1^2}{2br_2}) & \mid r_1 - r_2 \mid < b < r_1 + r_2 \\ \min(\pi r_1^2, \pi r_2^2) & 0 \leq b \leq \mid r_1 - r_2 \mid \end{cases} \tag{5.2}$$

Definition 5.3.4 *$F(D_1, D_2)$ denotes the derivative of overlap area of D_1, D_2 in terms of b.*

It can be calculated as:

Corrollary 5.3.1

$$\begin{aligned} F(D_1, D_2) &= \frac{dA(D_1, D_2)}{db} \\ &= \begin{cases} -\frac{\sqrt{(-b+r_1+r_2)(b+r_1-r_2)(b-r_1+r_2)(b+r_1+r_2)}}{b} & \mid r_1 - r_2 \mid < b < r_1 + r_2 \\ 0 & \end{cases} \end{aligned}$$

The derivative $F(D_1, D_2)$ can be interpreted as the intersecting segment between two disks.

When two disks D_1 and D_2 are of same size, i.e. $r_1 = r_2 = r$, the overlap area and derivative area are as follows:

Corrollary 5.3.2

$$A(D_1, D_2) = \begin{cases} -\frac{b\sqrt{(2r-b)(2r+b)}}{2} + 2r^2 \arccos(\frac{b^2}{2br}) & 0 < b < 2r \\ 0 & b \geq 2r \end{cases} \tag{5.3}$$

Corrollary 5.3.3

$$F(D_1, D_2) = \begin{cases} -\sqrt{4r^2 - b^2} & 0 < b < 2r \\ 0 & \end{cases}$$

5.3.3 Ring-ring overlap area and its derivatives

Suppose the two generalized rings $R_1(D_{1b}, D_{1s})$ and $R_2(D_{2b}, D_{2s})$ are identical, i.e.$r_{1b} = r_{2b} = r_b$ and $r_{1s} = r_{2s} = r_s$. To describe the relative pose (position and orientation) between the two rings, we use a triplet: (b, β, α) in the polar coordinate system, shown in Fig. 5.9. Here, b is the magnitude of vector $\overrightarrow{c_{1b}c_{2b}}$ and β is the polar angle of $\overrightarrow{c_{1b}c_{2b}}$ in the domain of $0 \leq \beta \leq 2\pi$. The relative orientation between the two rings is represented by α, with $0 \leq \alpha \leq 2\pi$.

Definition 5.3.5 *$A(R_1, R_2)$ denotes the overlap area between R_1 and R_2.*

The overlap area between them can be decomposed into four parts (Fig. 5.10) as follows:

$$\begin{aligned} \mid R_1 \cap R_2 \mid &= \mid (D_{1b} - D_{1s}) \cap (D_{2b} - D_{2s}) \mid \\ &= \mid D_{1b} \cap D_{2b} \mid + \mid D_{1s} \cap D_{2s} \mid - \mid D_{1b} \cap D_{2s} \mid - \mid D_{1s} \cap D_{2b} \mid \end{aligned}$$

The overlap area can be calculated from four disk-disk intersection areas:

Proposition 5.3.2

$$A(R_1, R_2) = A(D_{1b}, D_{2b}) + A(D_{1s}, D_{2s}) - A(D_{1b}, D_{2s}) - A(D_{1s}, D_{2b}) \tag{5.4}$$

Since the overlap area of two disks only depends on their distance, the distances (Fig. 5.10(a)-(d)) between different circular shapes are calculated to find out the overlap area:

$$\begin{aligned}
\| c_{2b} - c_{1b} \| &= b \\
\| c_{2b} - c_{1s} \| &= \sqrt{a^2 + b^2 - 2ab\cos(\beta)} \\
\| c_{2s} - c_{1b} \| &= \sqrt{a^2 + b^2 + 2ab\cos(\alpha - \beta)} \\
\| c_{2s} - c_{1s} \| &= \sqrt{(2a\sin(\alpha/2))^2 + b^2 - 4ab\sin(\alpha/2)\sin(\alpha/2 - \beta)}
\end{aligned} \tag{5.5}$$

$F_b(R_1, R_2)$, $F_\beta(R_1, R_2)$ and $F_\alpha(R_1, R_2)$ denote the derivatives of the overlap area between $R_1(D_{1b}, D_{1s})$ and $R_2(D_{2b}, D_{2s})$ in terms of b, β and α, respectively.

By substituting the distances bs in Eq. 5.2, Eq. 5.3, Eq. 5.4 with the distances obtained in Eq. 5.5, we obtain the overlap area in terms of (b, β, α). The first order derivatives in terms of b for each term in Eq. 5.4 can be simply derived as:

Proposition 5.3.3

$$\begin{aligned}
F_b(R_1, R_2) &= F_{D_{1b}D_{2b}b} + F_{D_{1s}D_{2s}b} - F_{D_{1b}D_{2s}b} - F_{D_{1s}D_{2b}b} \\
F_{D_{1b}D_{2b}b} &= F(D_{1b}, D_{2b}) \\
F_{D_{1s}D_{2b}b} &= F(D_{1s}, D_{2b})\frac{d(\sqrt{a^2 + b^2 - 2ab\cos(\beta)})}{db} \\
F_{D_{1b}D_{2s}b} &= F(D_{1b}, D_{2s})\frac{d(\sqrt{a^2 + b^2 + 2ab\cos(\alpha - \beta)})}{db} \\
F_{D_{1s}D_{2s}b} &= F(D_{1s}, D_{2s})\frac{d(\sqrt{(2a\sin(\alpha/2))^2 + b^2 - 4ab\sin(\alpha/2)\sin(\alpha/2 - \beta)})}{db}
\end{aligned} \tag{5.6}$$

The first order derivatives in terms of β for each term in Eq. 5.4 are:

$$\begin{aligned}
F_\beta(R_1, R_2) &= F_{D_{1b}D_{2b}\beta} + F_{D_{1s}D_{2s}\beta} - F_{D_{1b}D_{2s}\beta} - F_{D_{1s}D_{2b}\beta} \\
F_{D_{1b}D_{2b}\beta} &= 0; \\
F_{D_{1s}D_{2b}\beta} &= F(D_{1s}, D_{2b})\frac{d(\sqrt{a^2 + b^2 - 2ab\cos(\beta)})}{d\beta}; \\
F_{D_{1b}D_{2s}\beta} &= F(D_{1b}, D_{2s})\frac{d(\sqrt{a^2 + b^2 + 2ab\cos(\alpha - \beta)})}{d\beta}; \\
F_{D_{1s}D_{2s}\beta} &= F(D_{1s}, D_{2s})\frac{d(\sqrt{(2a\sin(\alpha/2))^2 + b^2 - 4ab\sin(\alpha/2)\sin(\alpha/2 - \beta)})}{d\beta}
\end{aligned} \tag{5.7}$$

The first order derivatives in terms of α for each term in the Eq. 5.4 are:

$$\begin{aligned}
F_\alpha(R_1,R_2) &= F_{D_{1b}D_{2b}\alpha} + F_{D_{1s}D_{2b}\alpha} - F_{D_{1b}D_{2s}\alpha} - F_{D_{1s}D_{2s}\alpha} \\
F_{D_{1b}D_{2b}\alpha} &= 0 \\
F_{D_{1s}D_{2b}\alpha} &= 0 \\
F_{D_{1b}D_{2s}\alpha} &= F(D_{1b},D_{2s})\frac{d(\sqrt{a^2+b^2+2ab\cos(\alpha-\beta)})}{d\alpha} \\
F_{D_{1s}D_{2s}\alpha} &= F(D_{1s},D_{2s})\frac{d(\sqrt{(2a\sin(\alpha/2))^2+b^2-4ab\sin(\alpha/2)\sin(\alpha/2-\beta)})}{d\alpha}
\end{aligned} \quad (5.8)$$

With the analysis of the overlap area and its derivatives, we can establish geometric models for finding optimized binding site designs.

5.4 Optimal ring shape design

5.4.1 Optimization objective and condition

As discussed above, an optimal pattern should allow only one energy minimum for all configurations (b, β, α) between two geometric patterns. Therefore, the corresponding overlap area should have only one maximum. A sufficient condition for such designs is that regardless of the part initial position, there should exist a motion path, by following which the overlap area strictly monotonically increases until the part reaches the unique alignment position. In the following sections, we discuss the possible paths satisfying this condition. To assure the existence of such paths, we derive the geometry constraints for different ring shapes including symmetric and asymmetric rings. Therefore, by finding the ring shapes satisfying the constraints, we can obtain a group of optimal rings.

5.4.2 Symmetric rings

With offset $a = 0$, the overlap area between two symmetric rings only depends on their distance b, and not β or α. Symmetric rings might have local maxima in overlap area [82] depending on the ratio r_s/r_b. Here, we analyze different ring configurations (r_s, r_b) based on our optimization model, and obtain quantitative results for optimized symmetric rings. Illustrations of the overlap area (Eq. 5.2) of $R_1(D_{1b}, D_{1s})$ and $R_2(D_{2b}, D_{2s})$ and its derivatives in terms of b are shown in Figs. 5.12.

A necessary condition for the ring shape to have a unique maximum is

Theorem 5.4.1 *The symmetric rings will have a unique overlap area maximum when the ratio between the inner disk radius and outer disk radius is no more than* $\sqrt{\sqrt{108}/2 - 5}$.

The proof of this theorem is based on the sufficient condition, there must exist a continuous path, along which b decreases and overlap area increases. In other words, the derivative of overlap area in terms of b, which is $F_b(R_1, R_2) = F(D_{1b}, D_{2b}) + F(D_{1s}, D_{2s}) - F(D_{1b}, D_{2s}) - F(D_{1s}, D_{2b})$, has to be less than zero in the domain of $0 \leq b \leq 2r_b$. The different overlap area terms and their derivatives are shown in Fig. 5.12. From Fig. 5.12(b), we can see that $F(D_{1b}, D_{2s}) + F(D_{1s}, D_{2b})$ in the domains of $(0, r_b - r_s]$ and $[r_b + r_s, 2r_b)$ are zero, so the total derivative cannot be positive. In addition, maximum of the derivatives is in the domains of $(\sqrt{r_b^2 - r_s^2}, r_b + r_s)$, as the term $F(D_{1b}, D_{2s}) + F(D_{1s}, D_{2b})$ has its maximum in magnitude at $b = \sqrt{r_b^2 - r_s^2}$ with the term $F(D_{1b}, D_{2b})$ monotonically increasing in the domain. Therefore, if there are positive total derivatives in the domain, there must be some in the domain of $[\sqrt{r_b^2 - r_s^2}, r_b + r_s]$.

In summary, the sufficient and necessary condition of non-positive derivative is that there is no non-negative derivative in the domain of $\sqrt{r_b^2 - r_b^2} \leq b \leq r_b + r_s$. Hence we have the following inequality,

$$\begin{aligned}
&F(D_{1b}, D_{2b}) - F(D_{1b}, D_{2s}) - F(D_{1s}, D_{2b}) \\
&= -\sqrt{4r_b^2 - b^2} + 2\sqrt{(-b + r_b + r_s)(b + r_b - r_s)(b - r_b + r_s)(b + r_b + r_s)}/b \leq 0, \\
&\sqrt{r_b^2 - r_b^2} < b < r_b + r_s
\end{aligned} \tag{5.9}$$

The solution to Eq. 5.9 is $r_s \leq \sqrt{\sqrt{108}/2 - 5}r_b$, with the numerical approximation of $r_s \leq 0.442891r_b$.

5.4.3 Asymmetric rings

The configurations for asymmetric rings include the ratios of r_s/r_b and a/r_b. With the inner cutout and outer disk not being concentric, both the orientation parameters β and α have to be considered for analysis. The parametric plots of asymmetric rings overlap derivative profile ($\alpha = \pi$) in terms of b is shown in Fig. 5.13.

Suppose the two asymmetric rings R_1 and R_2 are identical. For any given orientation (β, α), the derivatives of the overlap area with respect to b, $F_b(R_1, R_2)$, has a maxima. Such maxima decrease from $\beta = 0$ to $\beta = \pi$ at $\alpha = \pi$ (Fig. 5.13(b)), with the lower bound at ($\beta = 0$, $\alpha = \pi$) and upper bound at ($\beta = 0$, $\alpha = \pi$). Therefore, we have:

Proposition 5.4.1 *If the maximal derivative at ($\beta = 0, \alpha = \pi$) is smaller than zero, all the derivatives are smaller than zero and the overlap function will have a unique global maximum.*

Proposition 5.4.2 *If the maximal derivative at ($\beta = \pi, \alpha = \pi$) is more than zero, all the maxima at other orientations will be more than zero and the overlap area will have local maxima.*

With the sufficient condition for an optimal design: the existence of a motion path monotonically decreasing the overlap area, we construct two such motion paths from Proposition 5.4.1 and Proposition 5.4.2:

1. Motion path I (Fig. 5.14): translation and rotation. As illustrated in Fig. 5.14(a), one ring moves toward the center of the other one until they are concentric, and during this movement the overlap area increases. Though two rings are concentric, they might not be aligned (Fig. 5.14(b)) and the ring will rotate until they are perfectly aligned (Fig. 5.14(c)) corresponding to maximum overlap area. At a certain point in the translation step, the derivative in terms of b reaches maximum. If the maximum is smaller than zero, such a motion path can lead to the perfect alignment. From Proposition 5.4.1, we expect that for all initial positions, such motion paths (translation and rotation) exist leading to the final alignment.

2. Motion path II (Fig. 5.15): translation, rotation, translation and rotation. This motion path includes four different movements: first one ring translates toward the other until the overlap area no longer increases (Fig. 5.15(a)); the ring then rotates until the

overlap area no longer increases (Fig. 5.15(b)); the next two movements are the same to those in motion path I, including translation and rotation shown in Fig. 5.15(c) and (d). Finally, the maximum overlap area is reached as shown in Fig. 5.15(e). In this situation, derivatives in terms of b are not all negative, which does not satisfy the conditions in motion path I. Therefore, during the first translation step, there will be some points, at which the derivative in terms of b is positive or zero. However, in order to achieve the perfect alignment, there must exist at least one translation path with the derivatives in terms of b negative. From Proposition 5.4.2, such a path is in the direction of $(\beta = \pi, \alpha = \pi)$, which is the condition of this motion path II.

In summary, motion path I is a more strict constraint on the rings, while motion path II imposes the least strict constraints for asymmetric rings to reach perfect alignment.

For each constructed path, certain conditions have to be imposed. The following sections are dedicated to analyze the different situations.

Motion path I

If paths in the motion path I category exist, they have to satisfy two conditions:

1. There is only one overlap maximum at $b = 0$, regardless of the values of β and α.

2. When $b = 0$, there is only one overlap maximum at $\alpha = 0$.

In order to satisfy the first condition of unique maximum at $b = 0$, the derivative in terms of b has to be non-negative for all possible β and α. We only consider the derivative when $\beta = 0$ and $\alpha = \pi$ shown in Fig. 5.14(a), where the maximum happens.

The derivative consists of four different terms, illustrated in Fig. 5.16. From similar arguments in the symmetric ring section, we can derive the following inequality in the domain of $\sqrt{r_b^2 - r_b^2 + a} < b < r_b + r_s + a$:

$$\begin{aligned}
&- \sqrt{4r_b^2 - b^2} - \sqrt{4r_s^2 - (b-2a)^2} \\
&+ \frac{2\sqrt{(a-b+r_b+r_s)(b-a+r_b-r_s)}}{b} \\
&\times \sqrt{(b-a-r_b+r_s)(b-a+r_b+r_s)} \leq 0, \\
&\text{when} \sqrt{r_b^2 - r_b^2 + a} < b < r_b + r_s + a \qquad (5.10)
\end{aligned}$$

Numerical solutions are obtained to Ineq. 5.10 shown in Fig. 5.17(a). Each point in the plot of Fig. 5.17(a) is the solution to Ineq. 5.10, with the horizontal axis denoting the ratio of r_s/r_b and vertical axis of a/r_b .

From the second condition, we have that the first derivative of α is non-positive, when $b = 0$ and the rotation angle α is in the range of $[0, \pi]$ (Fig. 5.14(c)).

$$F_{D_{1s}D_{2s}\alpha} - F_{D_{1b}D_{2s}\alpha} \leq 0, \text{when } d = 0,\ \beta = 0 \text{ and } 0 \leq \alpha \leq \pi.$$

From Eq. 5.8, we have

$$\begin{aligned}
&F_{D_{1s}D_{2s}\alpha} = -\sqrt{4r_s^2 - 4a^2 \sin(\alpha/2)^2}a\cos(\alpha/2) \\
&\text{when } b = 0,\ \beta = 0 \text{ and } 0 \leq \alpha \leq \pi. \qquad (5.11) \\
&F_{D_{1b}D_{2s}\alpha} = F(D_{1b}, D_{2s}) \frac{d(\sqrt{a^2 + b^2 + 2ab\cos(\alpha - \beta)})}{d\alpha} = 0, \\
&\text{when } b = 0,\ \beta = 0 \qquad (5.12)
\end{aligned}$$

Therefore, Ineq. 5.11 can be simplified as

$$\begin{aligned}
&F_{D_{1s}D_{2s}\alpha} = -\sqrt{4r_s^2 - 4a^2 \sin(\alpha/2)^2}a\cos(\alpha/2) \leq 0, \\
&\text{when } b = 0,\ \beta = 0 \text{ and } 0 \leq \alpha \leq \pi. \qquad (5.13)
\end{aligned}$$

The solution to Ineq. 5.13 is
$4r_s^2 - 4a^2 \sin(\alpha/2)^2 \geq 0$, as $a\cos(\alpha/2) \geq 0$, when $\quad 0 \leq \alpha \leq \pi$.
Therefore we have $a \leq r_s$, which means the inner circular cutoff must touch the center of the large circle. By combining both of the solutions for the translation and rotation conditions, we have the solutions as plotted in Fig. 5.17(b).

In addition, we evaluate each feasible solution r_s, a by calculating the maximal derivative denoted by $F_{bmax}(R_1, R_2)$ for all feasible b in the domain of $(\sqrt{r_b^2 - r_b^2} + a, r_b + r_s + a)$. As in Fig. 5.18, each point in the surface represents a triplet $(r_s/r_b, a/r_b, F_{bmax}(R_1, R_2))$ with the feasible solution pair $(r_s/r_b, a/r_b)$ and the corresponding value of $F_{bmax}(R_1, R_2)$.

Motion path II

In this section, we analyze the paths in the motion path II category, which includes four different movements. As illustrated in Fig. 5.15(a) and (b), the part can always reaches the position shown in Fig. 5.15(c), as the overlap area reaches its maximum in terms of β and α. Therefore, to achieve the final perfect alignment, the overlap area must keep increasing during the movements illustrated in Fig. 5.15(c) and (d), which leads to two constraints:

1. The first order derivative of b is negative, when the part approaches from the thickest edge of the ring (Fig. 5.15(c)).

$$F_{D_{1b}D_{2b}b} + F_{D_{1s}D_{2s}d} - F_{D_{1b}D_{2s}b} - D_{1s}D_{2b}b \leq 0 \tag{5.14}$$

2. When $b = 0$, there is only one overlap maximum at $\alpha = 0$ (Fig. 5.15d). This condition is exactly as the conditions in Path I, with the solution to it as $r \leq R_b$.

The numerical solution of (r_s, a) for the first condition is shown in Fig. 5.19(a). By combining both of the solutions, the translation and rotation conditions, we have the solutions as plotted in Fig. 5.19(b).

In addition, we evaluate each feasible solution r_s, a, by calculating the maximal derivative $F_{bmax}(R_1, R_2)$ for all feasible b in the domain of $(\sqrt{r_b^2 - r_b^2} - a, r_b + r_s - a)$. As in Fig. 5.20, each point in the surface represents a feasible solution pair of (r_s, a) with the evaluation value of $F_{bmax}(R_1, R_2)$.

5.5 Summary and conclusions

In this chapter, we have discussed a first-order approximation model to simulate surface energy in the self-alignment process. In addition, we have investigated a method to find optimal geometric shape for alignment by using composite shapes. We have developed an analytical model of the simple case of composite shapes: rings. By using the model, we can decide the configurations of the rings in order to achieve unique alignment results.

From the results of optimizations, we can conclude:

- Symmetric rings require the constraint $r_s \leq 0.442891 r_b$ in order to achieve perfect alignment.
- From the results of the symmetric rings, we can generalize the result. If any pattern that can be enclosed in a circle with radius $r \leq 0.442891 r_b$ with r_b the outer circle radius, it can reach perfect alignment.
- Asymmetric rings satisfying the constraints as shown in Fig. 5.19 are optimal.

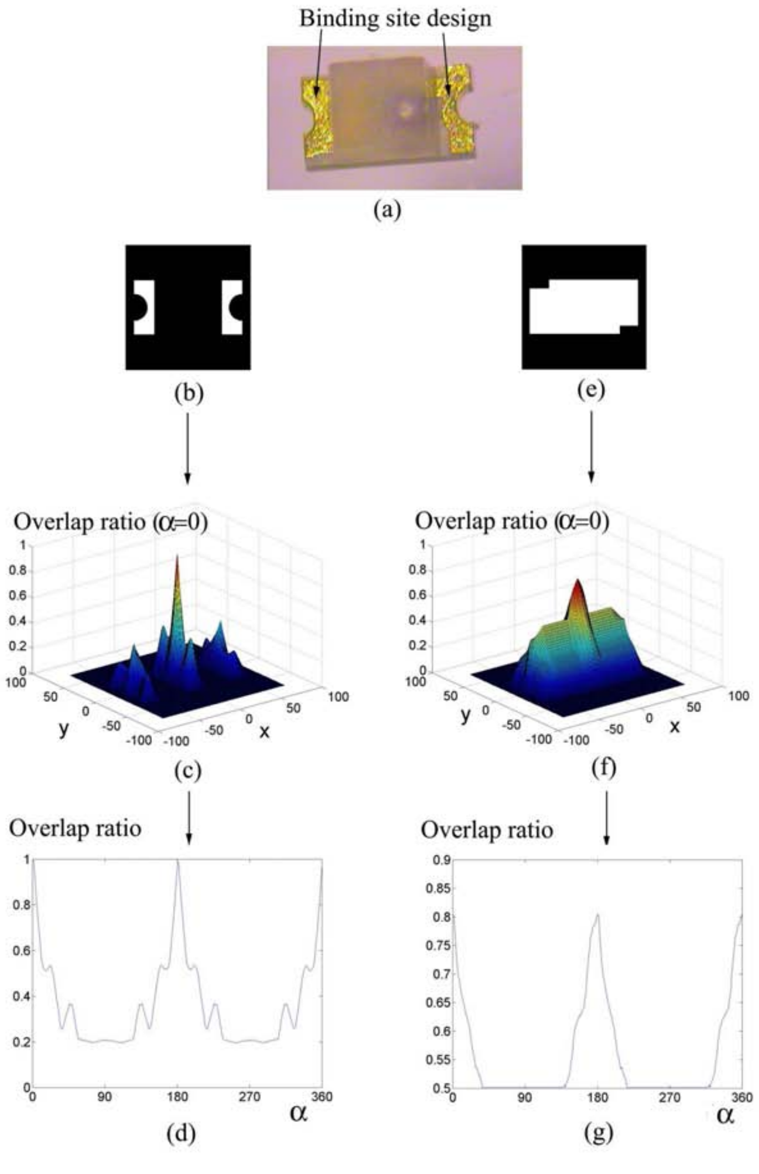

Figure 5.5: (a) A commercial LED with the given binding site design. (b) An straightforward design for the substrate binding site is the same as the binding site pattern of the LED. (c) Translation and (d) rotation simulations for the design in (b). (e) An improved binding pattern design for LED assembly, with the openings on the top-left and bottom-right corners for placing the electroplating bases. (f) Translation and (g) rotation simulations for the design shown in (e), which show no local maximum for the improved design.

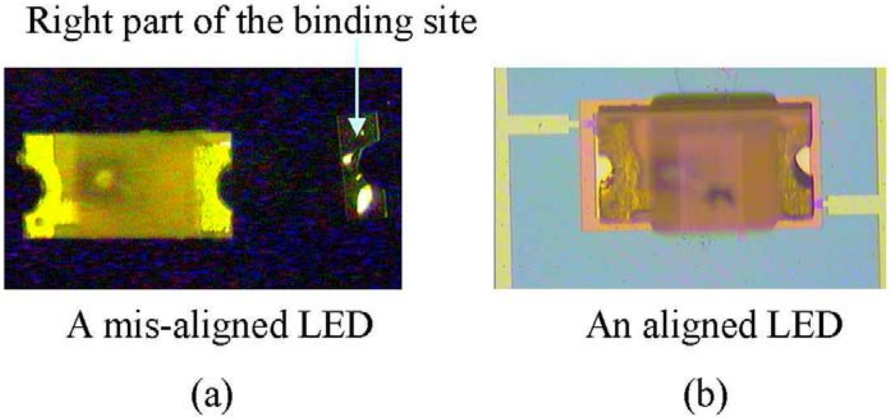

Figure 5.6: Assembly of LEDs to different binding sites: (a) A LED is mis-aligned on the binding site pattern shown in Fig. 5.5(b). (b) An LED is aligned on the improved binding site shown in Fig. 5.5(e).

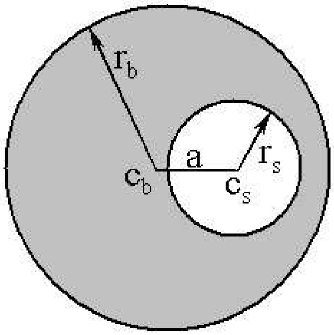

Figure 5.7: The parameters of a ring shape.

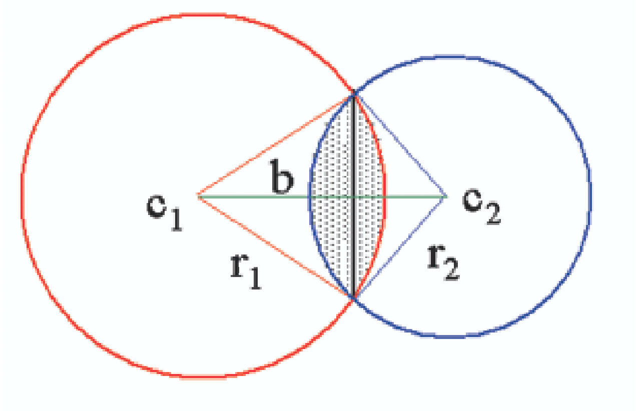

Figure 5.8: The overlap area between two disks.

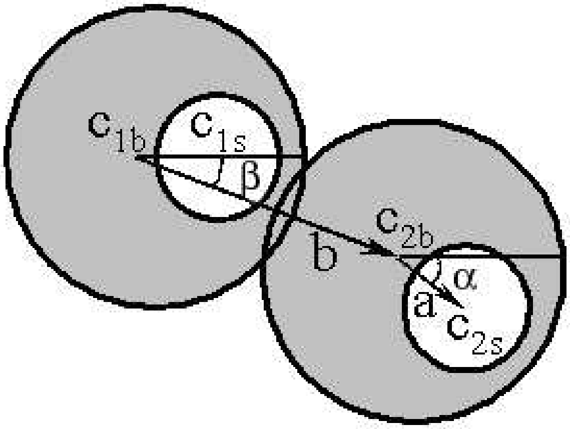

Figure 5.9: The parameters to describe the intersection between two identical rings $R_1(D_{1b}, D_{1s})$ and $R_2(D_{2b}, D_{2s})$.

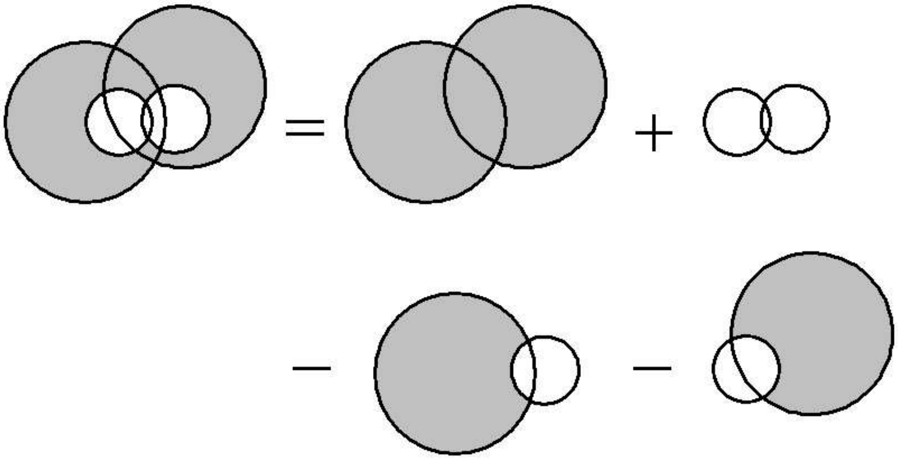

Figure 5.10: The intersection between two identical rings can be decomposed into four different intersections.

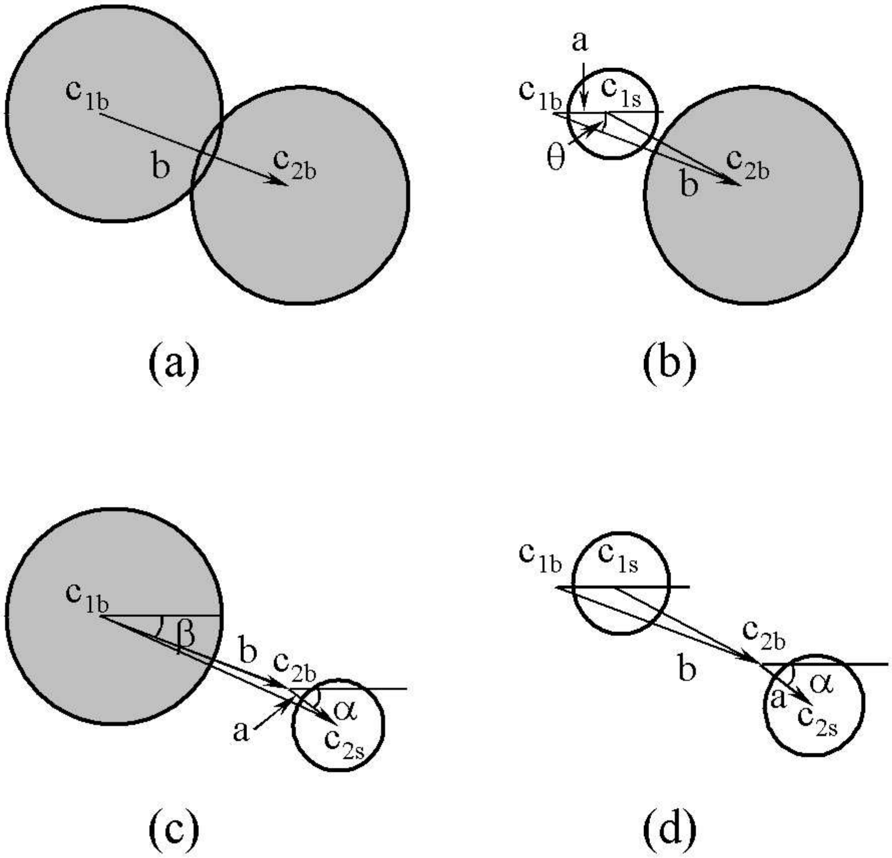

Figure 5.11: The four components of the ring-ring overlap areas are intersections between different circular shapes with centers of c_{1b}, c_{2b}, c_{1s} and c_{2s} respectively. (a). Intersection between c_{1b} and c_{2b}. (b). The intersection between c_{1s} and c_{2b}. (c). The intersection between c_{1b} and c_{2s}. (d). The intersection between c_{1s} and c_{2s}.

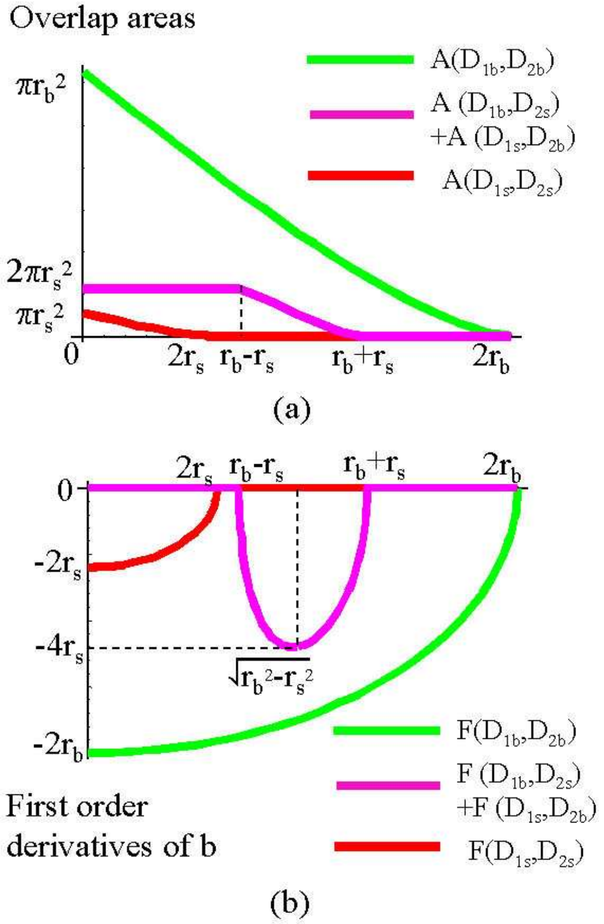

Figure 5.12: (a) The overlap area profile between two identical symmetric rings $R_1(D_{1b}, D_{1s})$ and $R_2(D_{2b}, D_{2s})$. Different terms plotted in different colors denote the overlap areas of different disks. (b) The derivatives of the overlap area terms.

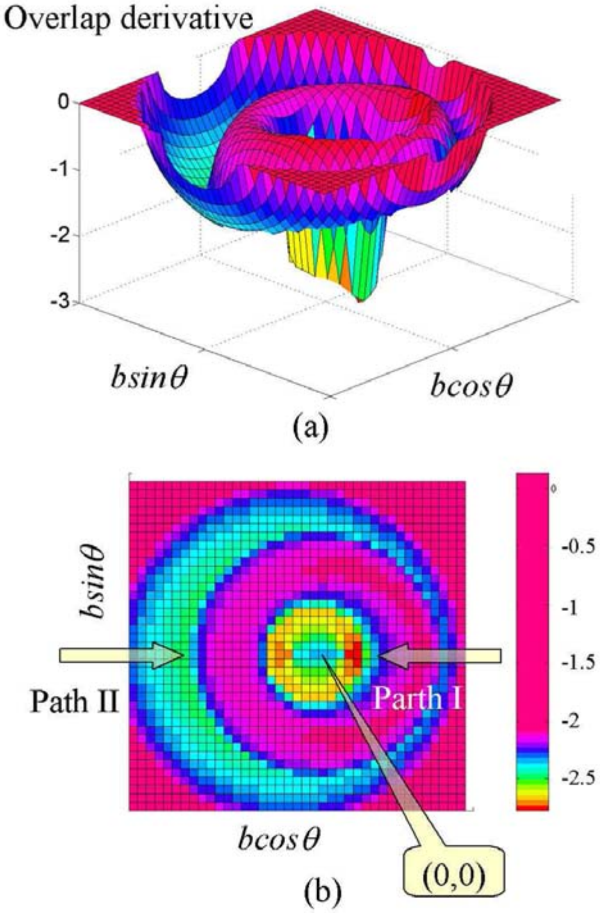

Figure 5.13: An example of the overlap derivative profile for asymmetric ring shape. (a) Three-dimensional plot. (b) Intensity plot with color representing the derivatives of the overlap area with respect to b.

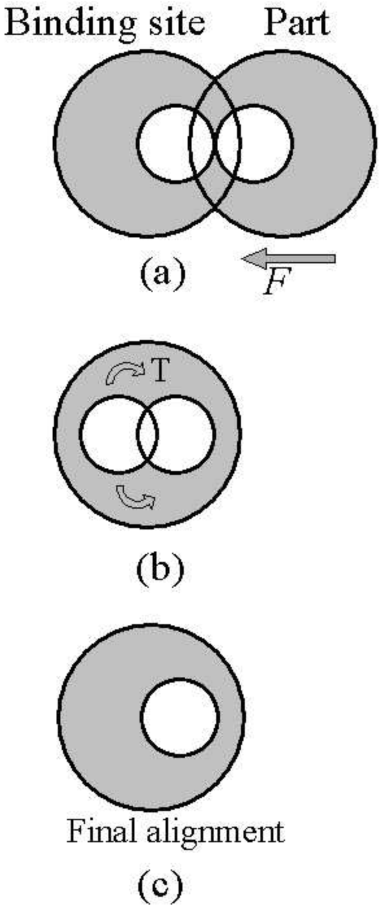

Figure 5.14: Constructed path I. (a) The part approaches the fixed binding site with the restoration force bigger than zero until their centers coincide. (b) The part then rotates till (c) perfect alignment.

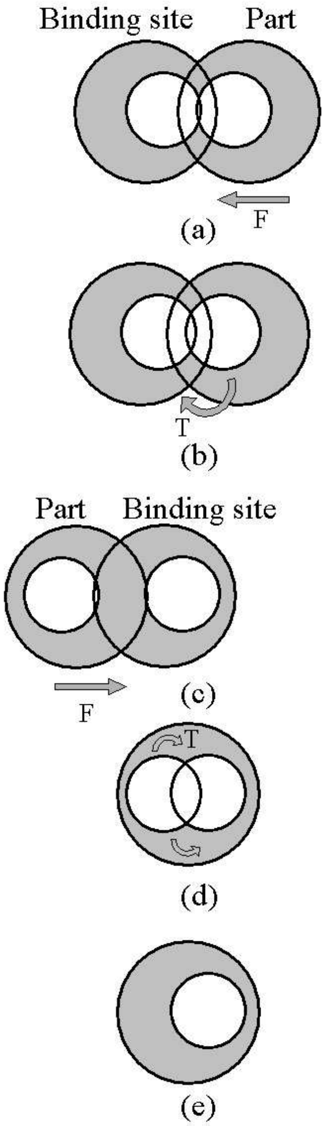

Figure 5.15: Constructed path II. (a) The part approaches the fixed binding site till restoration force is zero. (b) The part then rotates along the center of the fixed binding site until the maximum overlap area is achieved. (c) The part then moves towards the center of the binding site till their centers coincides. (d) The part then rotates till (e) perfect alignment.

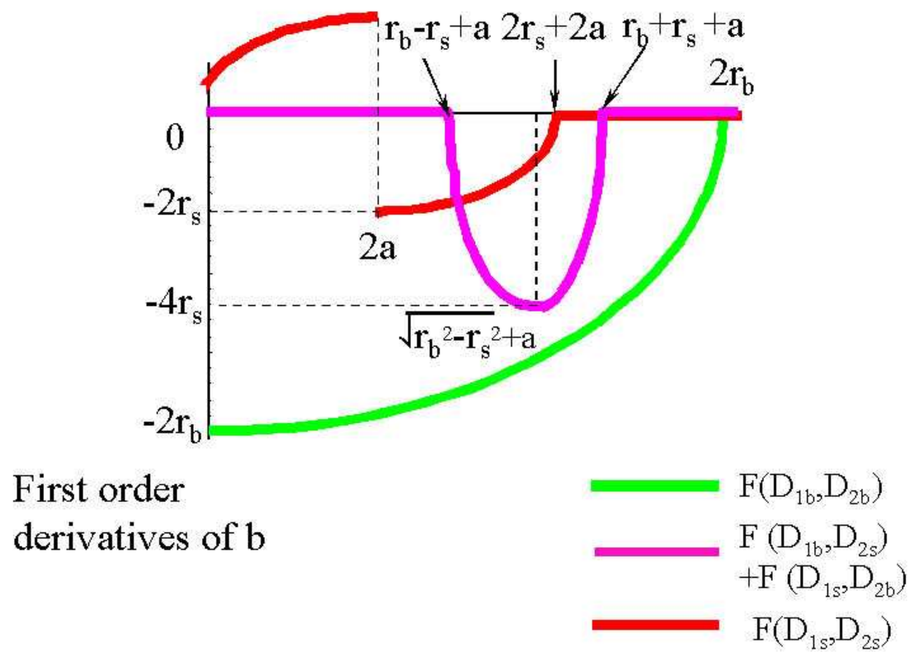

Figure 5.16: An example of first order derivative terms of overlap area.

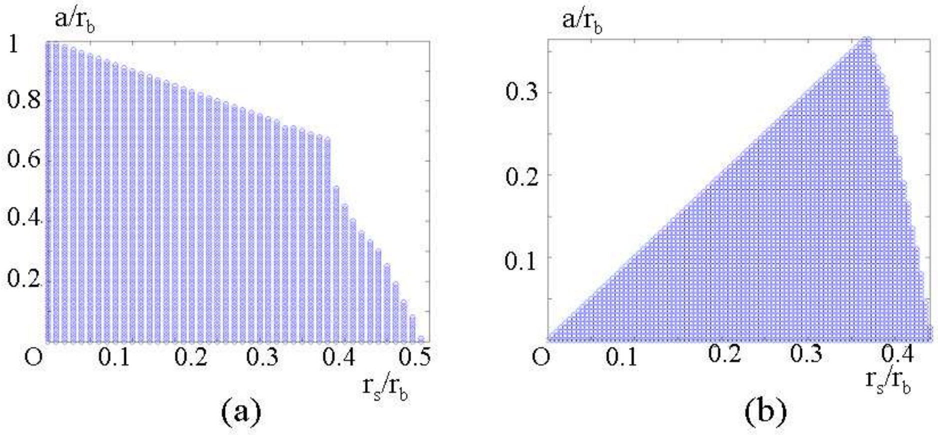

Figure 5.17: Numerical solutions satisfying two constraints of motion path I. (a) Solutions to the first condition. (b) Solutions to both of the conditions.

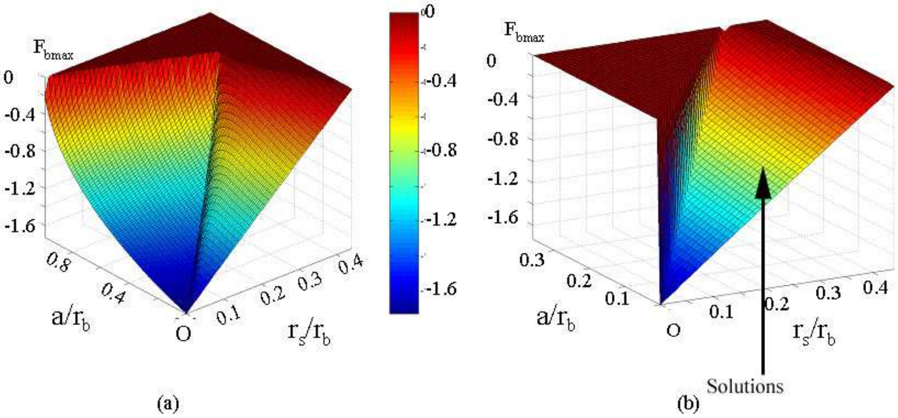

Figure 5.18: Evaluations of solutions satisfying the constraints for motion path I. The function value corresponding to each point (r_s, a) is the maximal overlap area derivative of b in its of $(\sqrt{r_b^2 - r_s^2} + a, r_b + r_s + a)$. (a) Solutions to the first condition. (b) Solutions to both of the conditions.

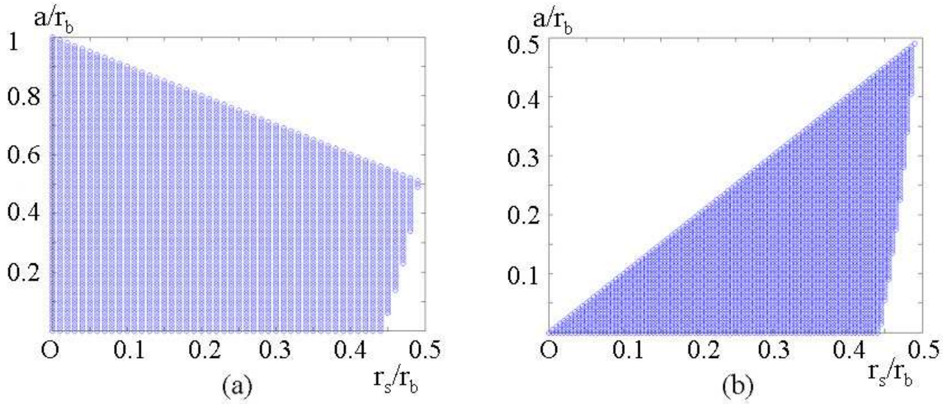

Figure 5.19: Numerical solutions to motion path II. (a) Solutions to the first condition. (b) Solutions to both of the conditions.

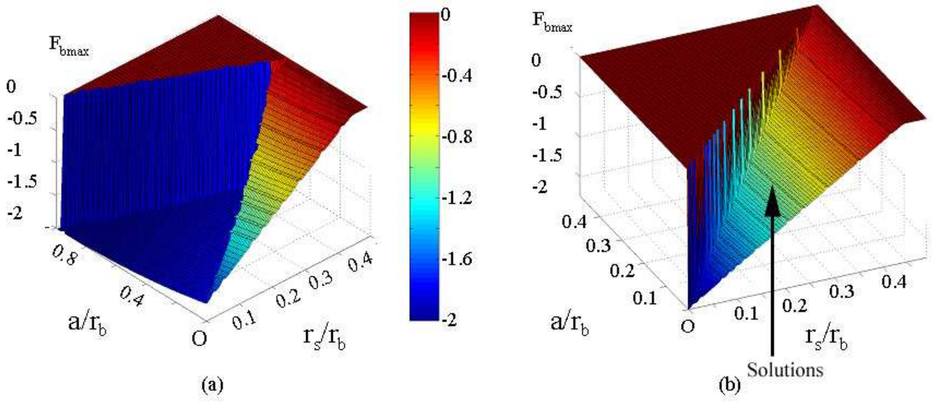

(a) (b)

Figure 5.20: Evaluations of solutions satisfying the constraints for motion path II. The function value corresponding to each point (r_s, a) is the maximal overlap area derivative of b in its domain of $(\sqrt{r_b^2 - r_s^2} - a, r_b + r_s - a)$. (a) Solutions to the first condition. (b) Solutions to both of the conditions.

Chapter 6

SURFACE MODIFICATION AND ELECTROPLATING

In this section, we discuss two key issues for our multi-batch assembly technique: surface modification and electroplating. The surface modification method provides us with a simple means for selectively activating the substrate binding sites for assembly. By repeatedly applying the surface modification and self-assembly steps, we can achieve multi-batch assembly. The surface modification techniques include alkanethiol SAM adsorption and SAM desorption, which changes the surface hydrophobicity back and forth. Electroplating, as the post-assembly step, establishes electrical connections for the assembled parts.

This chapter is dedicated to the discussion of the principles and experimental implementation of the surface modification and electroplating processes. It is divided into three sections: alkanethiol adsorption, alkanethiol reductive desorption and electroplating.

6.1 SAM adsorption

Since the discovery of thiol SAMs formed by long-chain thiols on Au surfaces in the early eighties [62, 84, 85], the study of different SAMs has attracted intensive attention from researchers e.g. [64, 68, 69, 86]. With the advantages including the ease of formation and the stability of the monolayer [87], thiol SAMs deposited on metals (gold, silver, nickel, iron, copper and mercury) provide a robust way to engineer surface properties and surface structures.

For our application, we use alkanethiol monolayers adsorbed on Au to change the Au binding sites to hydrophobic, and therefore activate the binding sites. The study of alkanethiol SAM adsorption mechanism has been presented in [88]. As a summary, the mechanism of adsorption of alkanethiol on a single crystalline Au(111) surface can be illustrated in Fig. 6.1. In Fig. 6.1(a), the alkanethiol adsorbs on the Au surface with lower coverage, until the saturation coverage is reached (Fig. 6.1(b)). Beyond the saturation coverage, the adsorbed alkanethiol starts forming high-density islands as shown in Fig. 6.1(c) due to the molecular interactions between the adsorbed alkanethiol. Finally, the nucleation islands of alkanethiol grow into a well structured and full-packed monolayer (Fig. 6.1(cd)).

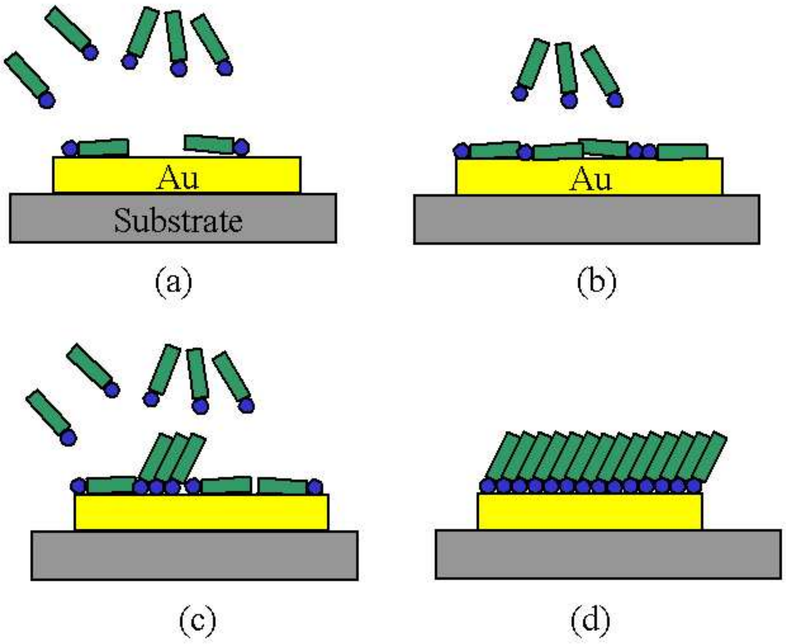

Figure 6.1: Alkanethiol adsorption on a single crystalline Au(111) surface. (a) The adsorption of alkanethiol on Au surface takes place instantly when Au is exposed to alkanethiol. (b) The adsorption continues until a saturation point is reaches. (c) Due to the alkanethiol interactions, nucleation islands of high-density alkanethiol start to form. (d) The islands grow into a well-orientated full-packed alkanethiol monolayer on the Au(111) surface.

To perform adsorption, we immerse the Au surface in the solution of alkanethiol in solvent. We use fresh-prepared ethonalic alkanethiol solution of 1mM dodecanethiol ($CH_3(CH_2)_{11}SH$, Aldrich). The adsorption of alkanethiol SAM on Au happens simultaneously as the Au surface is put into the solution (Fig. 6.1(a)). However, to form a well packed and organized monolayer, with the alkanethiol tilted 60° to the horizontal plane (Fig. 6.1(d)), more time is needed [64, 69, 72]. Usually, we soak the sample overnight (∼10 hours) [64, 72, 73]. After the adsorption, an alkanethiol monolayer is formed on the exposed Au areas on the substrate. The sulfur compound in alkanethiol forms a bond with Au, with the functional hydrophobic long hydrocarbon chain being exposed to the external environment. Therefore, the surface becomes hydrophobic, and the measured contact angle of the SAM of dodecanethiol on Au is 93°. Therefore, the binding sites are activated for assembly.

In addition to the Au on silicon substrates, we use some single crystalline Au(111) samples for the purpose of characterizing different alkanethiol SAM desorptions. The sample are prepared by evaporating Au on mica [86]. They are soaked in 1mM alkanethiol ($CH_3(CH_2)_nSH$, n=2, 7, 11, 17, Aldrich) solutions in ethanol overnight for the SAM adsorption, prior to the desorption process. The details of the desorption experimental setups and different SAM desorption characterizations are discussed in detain in the following section.

6.2 Selective SAM desorption

After SAM adsorption, the reductive desorption is carried out. Unlike the SAM adsorption, which takes place on all the binding sites, the desorption is performed on selected binding sites to de-active them by applying potential bias to them. Afterwards, the desired binding sites, which are without desorption, stay activated and hydrophobic, and ready for assembly.

In our multi-batch self-assembly method, the desorption process plays a crucial role. Without it, we cannot selectively activate binding sites, and cannot perform multi-batch assembly. Furthermore, compared to the method of removing the SAM by UV light etching through a mask [61], this electrochemical desorption is advantageous for its ease of experimental implementation.

In Fig. 6.2, we plot the SAM desorption process schematically. The reductive reaction of alkanethiol SAMs on the Au surface is as follows:

$$CH_3(CH_2)_nSAu + e^- \rightarrow Au + CH_3(CH_2)_nS^- \tag{6.1}$$

6.2.1 Desorption results and discussions

With SAM desorption, the binding sites will change to hydrophilic and thus become deactivated. When the substrate with lubricant is slid into water, the de-activated binding sites, those with desorption, will not be wetted by the lubricant.

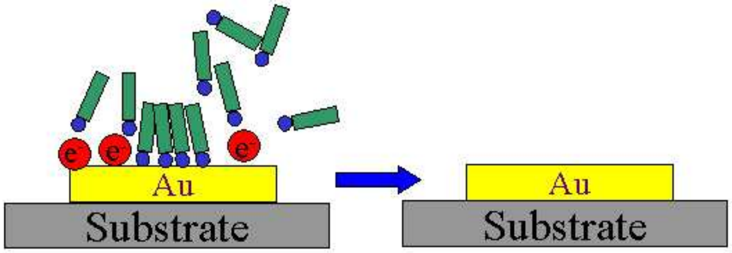

Figure 6.2: Electrochemical desorption of alkanethiol SAM from the gold surfaces. (a) With reductive reaction of alkanethiol SAM, the thiol is removed from the Au surface. (b) Without SAM, the Au binding site becomes hydrophilic.

Fig. 6.3 shows the initial results of the octadecanethiol SAM desorption in two pictures of substrates with lubricant in water. The desorption time is approximately six hours for Fig. 6.3(a), and three hours for Fig. 6.3(b).

Fig. 6.3(a) shows the difference between the binding sites with and without desorption: the lubricant wets the binding sites without desorption on the left, while it does not wet the binding sites with desorption on the right. Therefore, we can tell that the desorption has completed for the binding sites on the right and makes them hydrophilic. Those on the left are without desorption and stay hydrophobic.

In Fig. 6.3(b), potential bias is applied to all the square binding sites from an electrical contact, which is not shown in the picture. The contact is at the middle bottom position of the sample. Fig. 6.3(b) shows the relationship between the binding site hydrophobicities and their distances to the contact: the further, the less desorbed and the more hydrophobic, as indicated by the arrows in the picture.

These results show that it can take as long as six hours to desorb octadecanethiol SAMs from the Au binding sites. To find an optimal alkanethiol forming stable SAMs for assembly, but also possessing desorption time suitable for our application, we have explored reductive desorption of different alkanethiolate SAMs ($CH_3(CH_2)_nSH$, n=2,7,11,17). Therefore, cyclic voltammograms, obtained from single crystalline Au(111) on mica [63, 69], have been used for characterization. With single crystalline Au(111), we can obtain well-defined CV curves

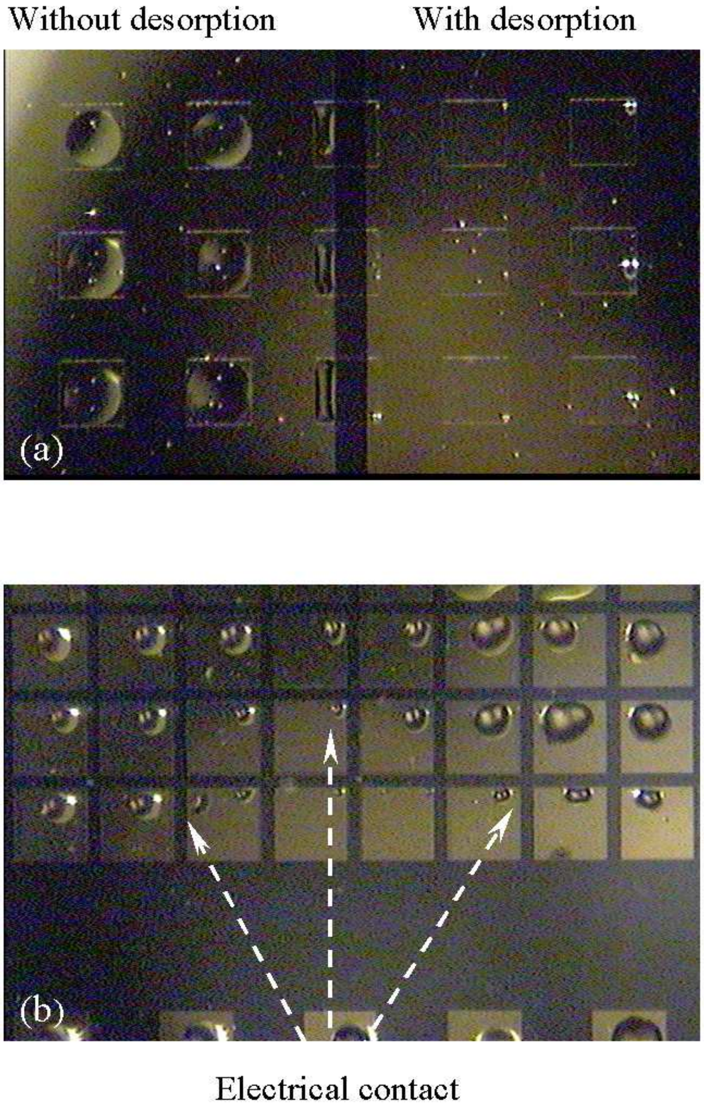

Figure 6.3: Results from selective octadecanethiol SAM desorption. (a) A substrate with six-hours selective SAM desorption. The potential bias is applied on the right hand side of the substrate in the image to remove the SAM. The gold patterns on the left have SAM on them, thus the surfaces are hydrophobic. (b) A substrate with three-hour SAM desorption. The potential bias is applied to all the square binding sites from an electrical contact. The contact, not shown in the picture, is at the middle bottom position of the sample. The closer the binding sites are to the contact, the more SAM is desorbed and they are more hydrophilic.

and have more insight into the desorption.

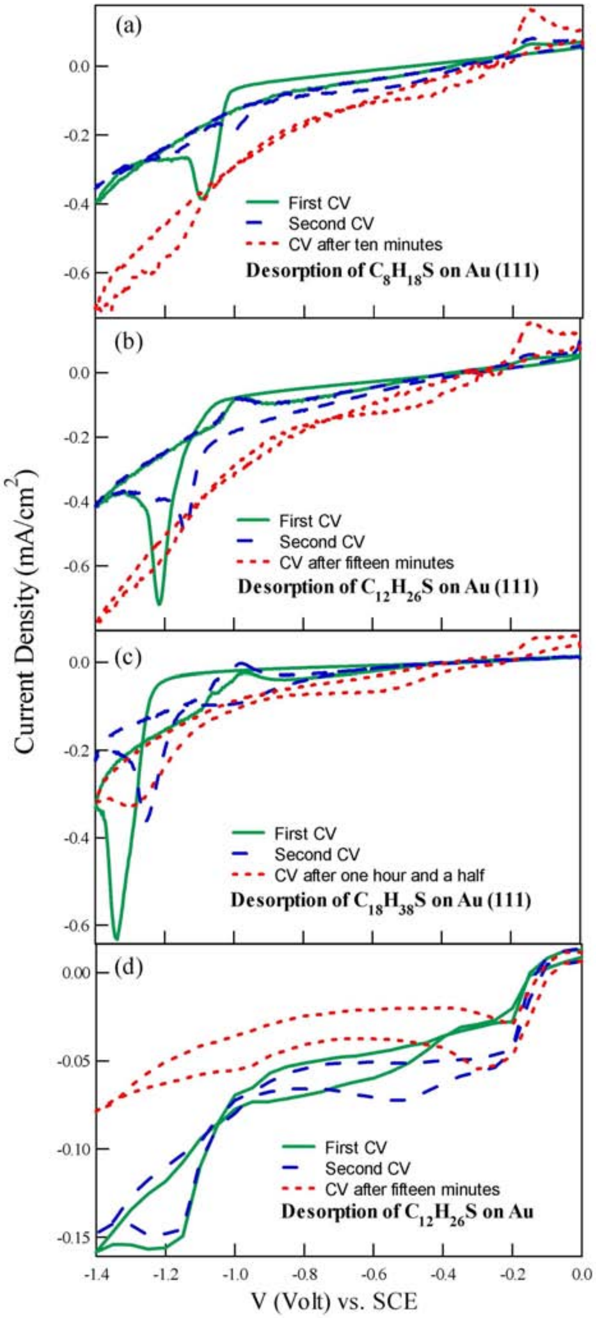

Figure 6.4: (a)-(c) CVs of SAM desorption from Au(111) on mica. (a) Octanethiol ($C_8H_{18}S$). (b) Dodecanethiolate ($C_{12}H_{26}S$). (c) Octadecanethiol ($C_{18}H_{38}S$). (d) CVs of dodecanethiolate ($C_{12}H_{26}S$) SAM desorption from polycrystalline Au on Si.

Figs. 6.4(a)-(c) show results from the reductive desorption experiments of Au(111) on mica samples. The clear negative current peaks in the CVs indicate the reductive desorption of alkanethiolate SAMs from the surfaces. These peaks become less pronounced with additional CV scanning cycles, implying the decreasing coverage of SAMs. The disappearance of the desorption peaks indicates that a major portion of the SAM has been desorbed. The desorption peak shifts systematically with carbon chain length, with the $C_8H_{18}S$, $C_{12}H_{26}S$ and $C_{18}H_{38}S$ peaks being at -1.05V, -1.2V and -1.35V vs SCE (Figs. 6.4(a)-(c)). Also, the time needed to desorb the SAMs varies systematically with chain length. For example, the longest alkanethiolate SAM assessed, $C_{18}H_{38}S$, still has a significant fraction on the surface after one hour and half of desorption (Fig. 6.4(c)).

These results agree with previous studies [62, 89]. The reasons are that monolayers formed by alkanethiols with longer chain lengths are more densely packed and the lower ion permeation during the desorption process [62, 89, 90]. The chain length also affects the stability of the monolayer. On the other hand, we observe that the surface with propanethiolate SAM changes hydrophobicity in the KOH solution even in the absence of an applied potential. Therefore, propanethiol is ruled out as a choice for the assembly experiment. The longer desorption time for the longer chain length alkanethiolate SAMs might be the result of re-adsorption of the reduced products. The discussions in [68] suggest that the re-adsorption is attributed to the solubilities and diffusion rates of the alkanethiolate desorption products, with the longer alkanethiolates having the lower solubility and diffusion rate.

By comparing desorption time (Figs. 6.4a-c) and stability of the different alkanethiolate SAMs, dodecanethiol ($C_{12}H_{26}S$) is chosen for the assembly experiments. The dodecanethiol forms a stable hydrophobic SAM on Au, and desorption of a major fraction of the monolayer takes approximately fifteen minutes implied by the disappearance of the desporption peak in the dotted CV data in Fig. 6.4b.

Desorption of dodecanethiolate SAM from polycrystalline Au patterns on a Si substrate is shown in Fig. 6.4d. These desorption CVs have broader peaks, compared with desorption CVs from single crystalline Au on mica. Moreover, it is observed that the time needed to desorb the SAM to turn the Au surface hydrophilic is longer than the time measured by the disappearance of the desorption peak. A sample of the binding sites after fifteen minutes of dodecanethiolate desorption is shown in Fig. 6.5. Fig. 6.5(a) is a picture of a substrate, with each column of the binding sites being electrically connected. Fig. 6.5(b) shows a substrate with lubricant in water, after fifteen minutes of dodecanethiol desorption as measured by the desorption peak disappearance. The shrinking droplets in the two column of square binding sites in the center (Fig. 6.5(b)) suggest that the desorption has taken place on them, while it has not completely remove the SAM yet.

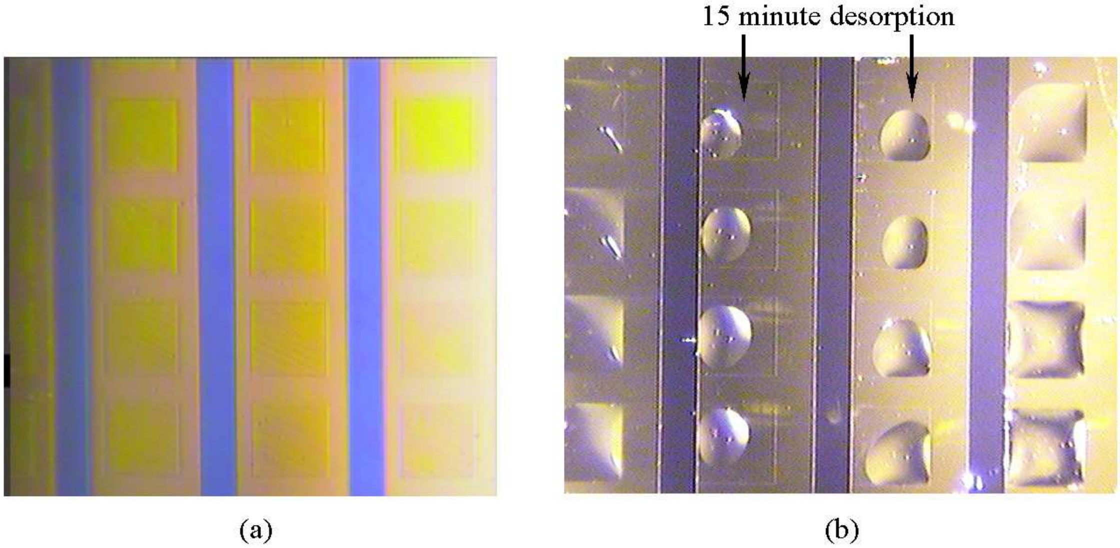

(a)

(b)

Figure 6.5: (a) A substrate with arrays of square binding sites. Each column of the exposed squares is electrically connected. (b) A substrate with lubricant in water, after fifteen minutes desorption. The two columns of binding sites in the center have SAM desorption, as indicated by the shrinking lubricant droplets on them. However, the SAM has not been completely removed from the binding sites yet.

Therefore, we usually perform the desorption longer and the average desorption time for the designs shown in Fig. 3.1e is around one hour for dodecanethiol SAM.

6.3 Two step assembly

By repeating the surface modulation and self-assembly steps, multi-batch assembly can be achieved. A substrate shown in Fig. 3.1 is used to demonstrate two step assembly of square test parts. The substrate is first coated with dodecanethiolate SAM (Fig. 2.1(b)). Then selected sites undergo electrochemical desorption to return them to the hydrophilic state (Fig. 2.1(c)). After SAM adsorption and one hour selective desorption, the substrate with a thin layer of lubricant is immersed in water (Fig. 2.1(d) without part). The different lubricant wetting properties of Au binding sites with and without SAM are readily seen in Fig. 6.6(a). The Au squares without SAM on the substrate remain lubricant free (Fig. 6.6(a)). Next, a first batch of parts is added to the aqueous phase and assembled on the lubricant coated layer (Fig. 6.6(b)). The square test parts are used as fabricated. Untreated Au surfaces have a contact angle of 70° (Table. 4.1), after exposure to lab atmosphere, which is sufficient to ensure assembly. After curing the lubricant and cleaning the substrate, a second assembly is performed by repeating steps described in Fig. 2.1(e) and (f).

By repeating SAM adsorption, desorption and assembly, controlled micro assembly is feasible, in principle, for a large number of batches.

6.4 Electroplating process

We now turn to demonstrate the use of an electroplating method to establish electrical connections to assembled parts. The plating process employs a platinum mesh as an anode and the plating bases on the substrate as a cathode. The bath is a commercial solder solution (Technic solder matte NF 820 HS (60/40), Technic Inc.). The plated solder is an alloy of lead (Pb) 40wt.% and tin (Sn) 60wt.%.

Our choice of the electroplating basis metal is mainly based on the following considerations: compatibility with the substrate fabrication process and adhesion with electroplated alloy. Different metals: Au, aluminum (Al), titanium-tungsten (TiW) and Ni have been tested. The results are summarized in Table 6.4.

In Fig. 6.7, it is shown that the plated alloy has smoother and even profile on the Au seed (Fig. 6.7(a)(c)) than on the TiW (Fig. 6.7(b)(d)). The electroplating on TiW seed is performed at the current density of 1A/cm^2 and plating rate at 2μm/min, and the plated

Table 6.1: Comparisons between electroplating basis materials.

Metals	Process compatibility	Adhesion with alloy
Au	compatible.	good
Al	compatible.	poor
TiW	incompatible	poor
Ni	compatible.	good

solder at lower current density has poorer adhesion and the solder can be rinsed away by water. Electroplating on Au seed is performed at the current density of 300mA/cm^2 and plating rate of 3μm/min. The poor adhesion on Al and TiW is due to their natural oxide layer, while Au does not have such a natural oxide layer. As a result, the plated alloy has uneven profile on Al and TiW plating bases.

Good adhesion between Ni plating basis and the plated alloy is observed (Fig. 6.8), though the nickel has an oxide layer as well. The Ni oxide, which is thinner than the Al oxide [91], can be reduced at the plating potential in the acid electroplating solution, thus allowing good adhesion.

To demonstrate the electroplating method, we use LEDs for assembly by repeating the process described in Figs. 2.1a-d. The current density for plating is 300mA/cm^2 on the Ni base, and the plating rate is approximately 5μm/min. The resistivity of the alloy is approximately $1.4\times10^{-7}\Omega$m.

The results are shown in Fig. 6.9. In Fig. 6.9a, we show a Au binding site with two Ni plating bases. The design is chosen based on the simulation results in Fig. 5.5. No alkanethiolate SAM is formed on the oxide coated Ni during the adsorption process. Thus during the assembly process, the lubricant does not wet the Ni plating bases, leaving them clean for electroplating (Fig. 6.9b). An assembled LED is aligned and bonded at the desired site after lubricant curing (Fig. 6.9c).

In Fig. 6.10a, we show an environmental scanning electron microscope (ESEM) image of an assembled LED. The gap between the LED and the substrate is approximately

20μm. Using the electroplating procedure described above, the gap is bridged by solder alloy (Fig. 6.10b) and assembled LEDs can be activated by applying voltage to the electrical contacts on the substrate described in Chapter 3. Measured contact resistance is 10Ω for the current design. An illustration of an activated glowing LED on a substrate is shown in Fig. 6.11.

6.4.1 Substrate material and durability

As discussed above, both Au and Ni are demonstrated as good electroplating basis metals. However, there are several considerations that make Ni advantageous. When using Au bases, an extra desorption process is needed to remove the alkanethiolate monolayer deposited on the bases. Also, we have observed severe wrinkling and peeling of SOG on Au after approximately two hours of desorption in the alkaline bath. This is due to poor adhesion between SOG and Au, particularly in alkaline solution (i.e. 0.5M KOH) with potential bias applied to the Au areas. Tests of silicon nitride on Au during the desorption process have also shown wrinkling results. To overcome these problems Ni is chosen as an additional metal for electroplating basis. The Ni layer is also patterned as connections between the Au binding sites and the electrical contacts to reduce the contact area between Au and the passivation layer. With Ni beneath the passivation layer, it is observed that there are no signs of wrinkling after more than two hours, when performing SAM desorption.

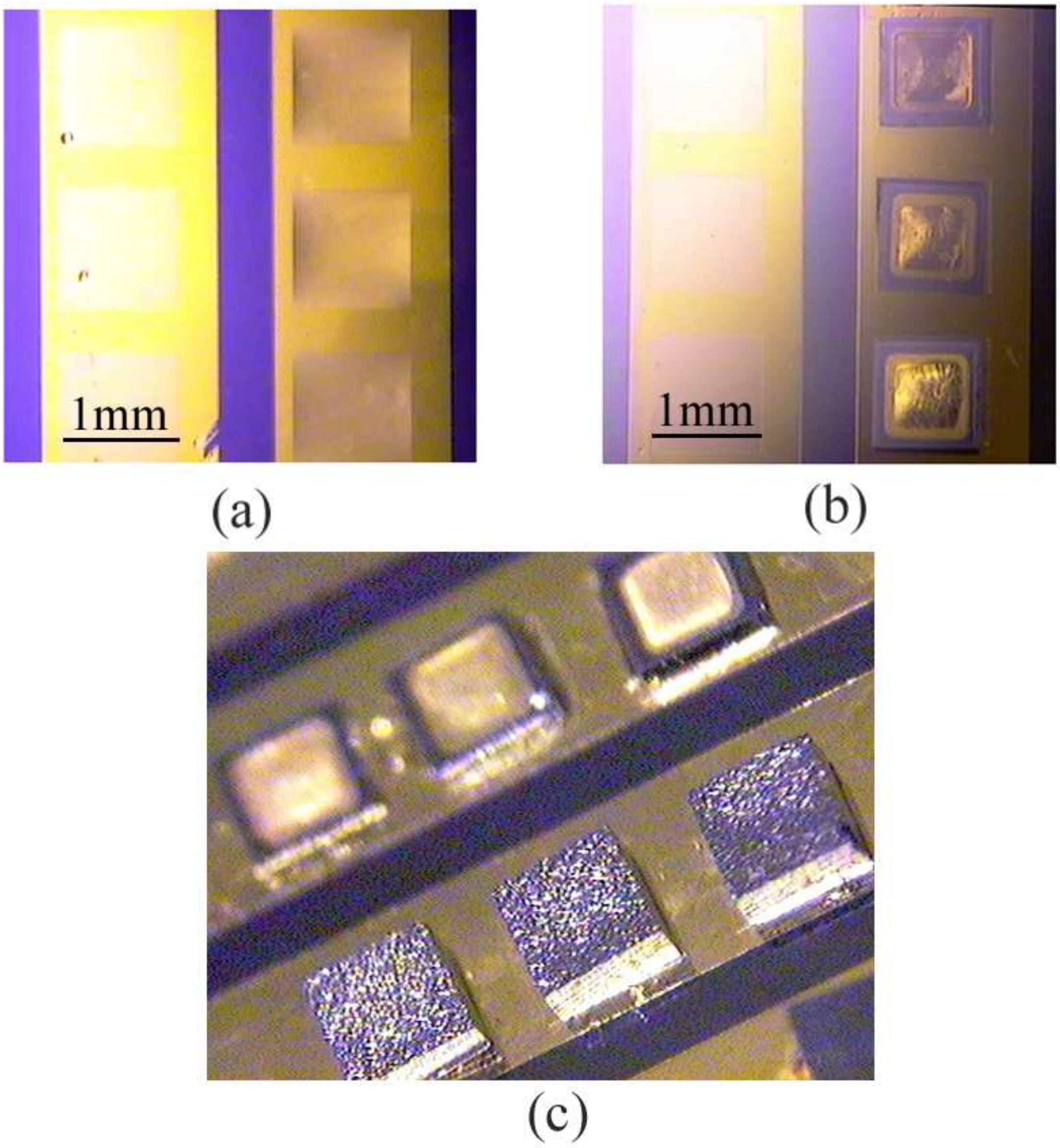

Figure 6.6: (a) A substrate with lubricant in water after selective SAM desorption. Reductive desorption has removed SAM from the Au squares on the left column. Lubricant wets the Au squares with SAM. (b) First batch of 1×1mm^2 parts have been assembled and bonded only to Au patterns with lubricant on the right. (c) Side view of two-batch controlled micro assembly. Foreground: Second batch of 1×1mm^2 assembled parts. Background: First batch of assembled parts.

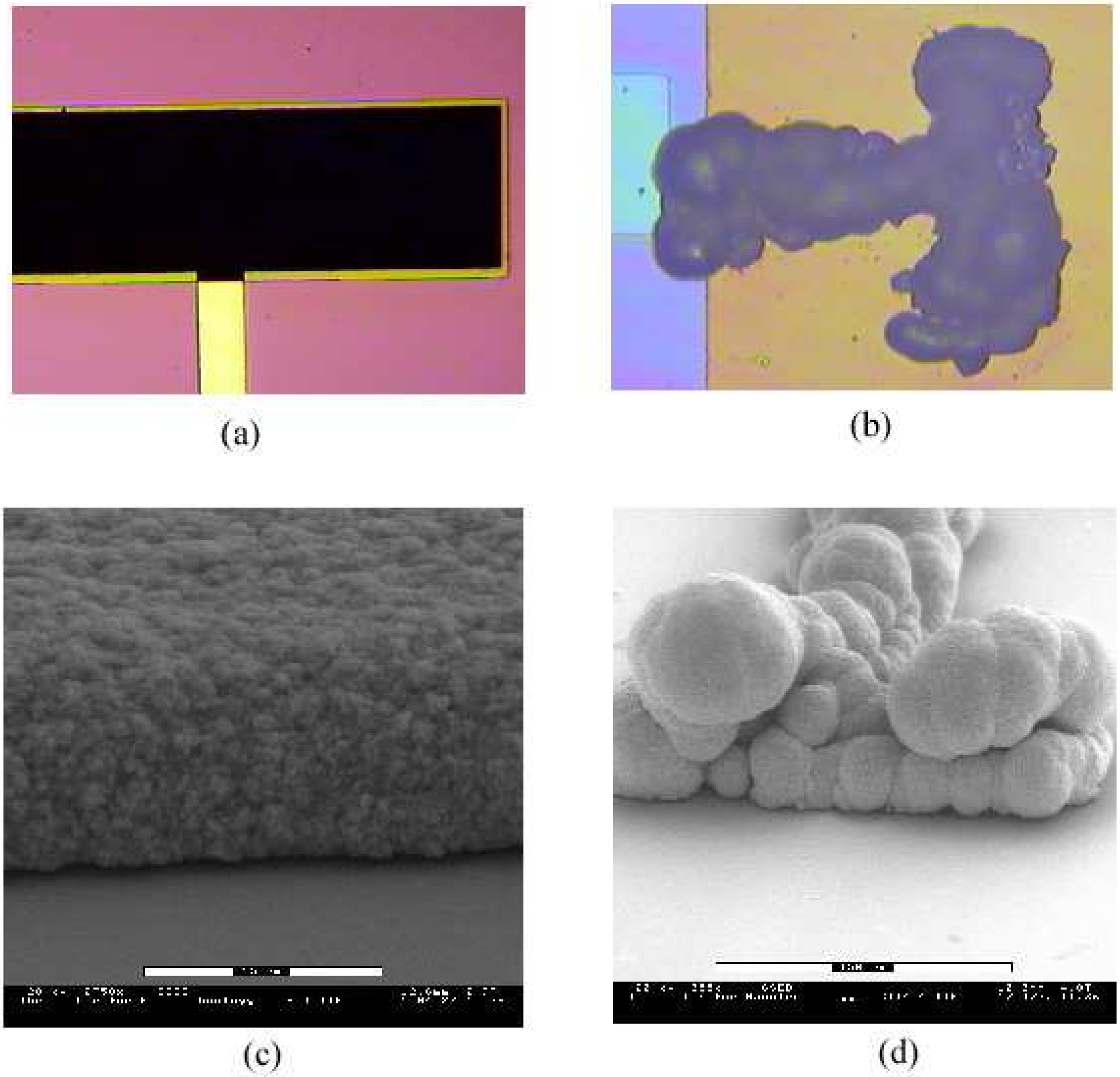

(a) (b) (c) (d)

Figure 6.7: Electroplated solder on Au and TiW seeds. (a) Image of smooth plated solder on Au. (b) Image of plated solder on TiW seed with mushroom profile. (c) An ESEM image of the plated solder on Au seed. (d) An ESEM image of the plated solder on a TiW seed.

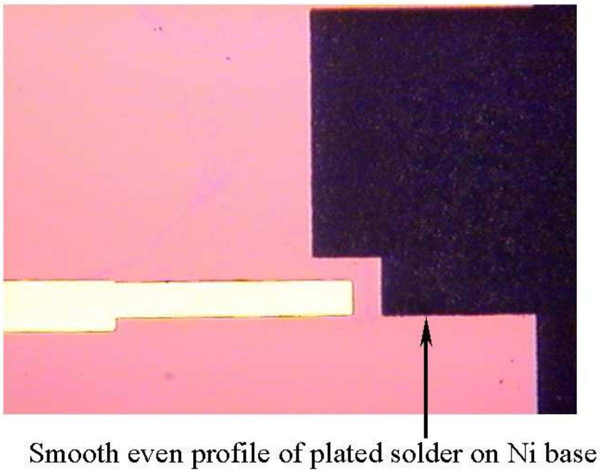

Figure 6.8: Solder plated on Ni base shows smooth and even profile.

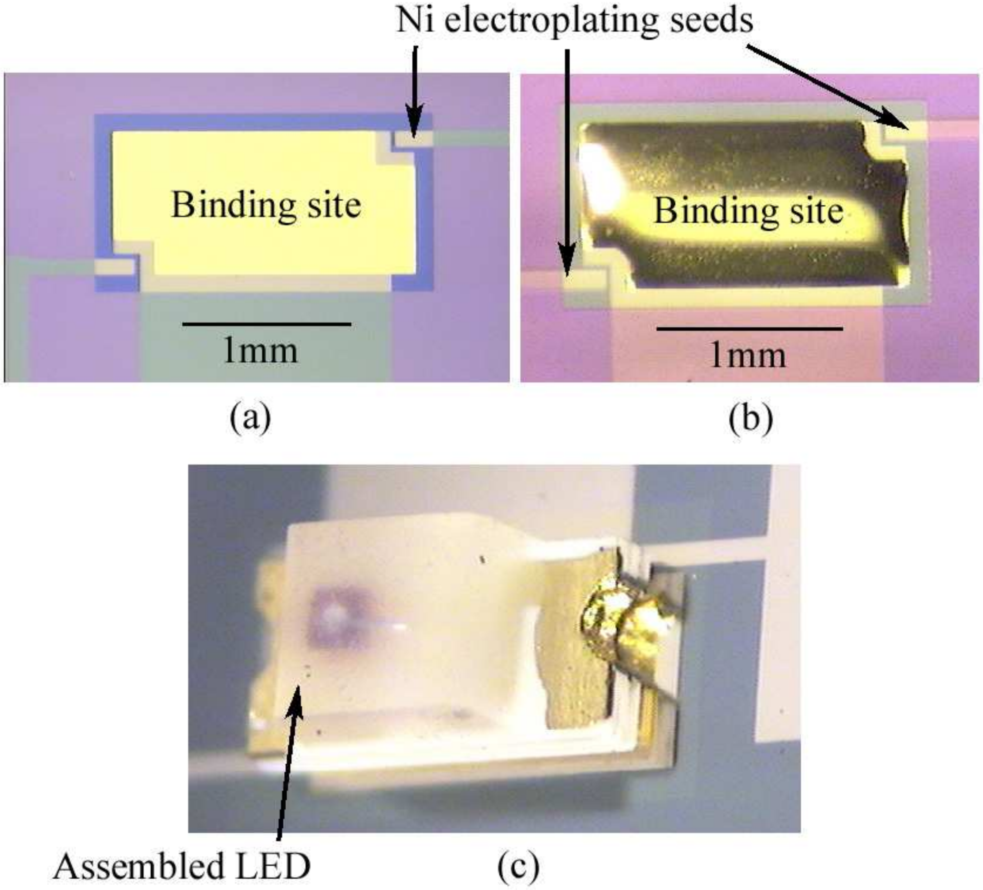

Figure 6.9: (a) A binding site designed for LED assembly. (b) A binding site with SAM after lubricant is applied. The exposed Ni electroplating bases remain clean. (c) An assembled LED on a binding site.

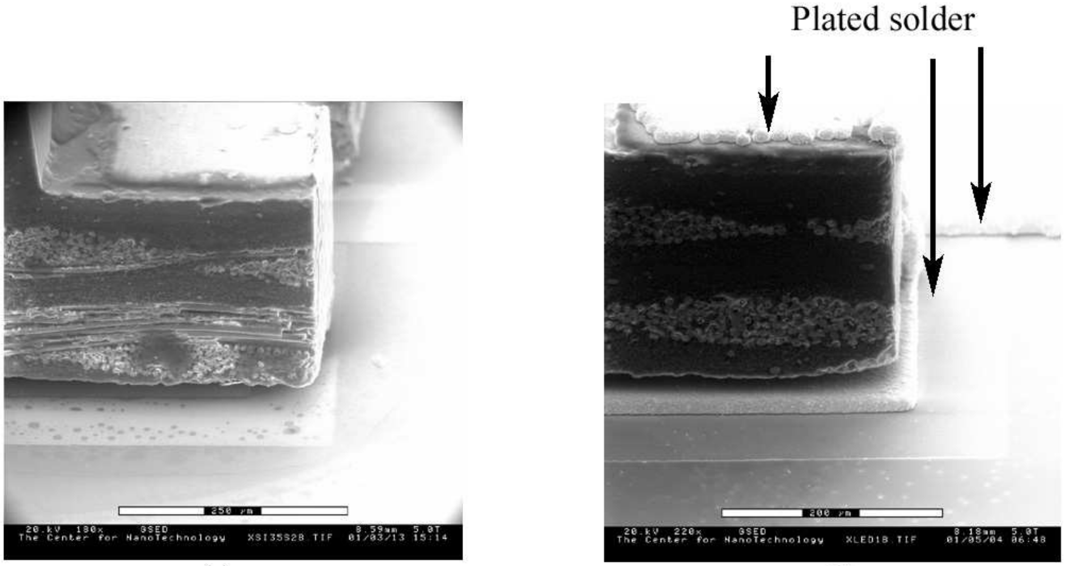

(a) (b)

Figure 6.10: (a) An environmental scanning electron microscope (ESEM) image of an assembled LED. (b) An ESEM image of an assembled LED after electroplating.

Figure 6.11: An LED on a substrate after electroplating. The LED is lightened by applying potential on the electrical contacts on the substrate.

Chapter 7

SELF-ASSEMBLY IN THE THE MICRO AND NANO DOMAIN

In the previous chapters, we have discussed the surface-tension driven self-assembly technique covering the aspects of the principle, experimental implementation, simulation and surface geometry design. We have demonstrated the capability to assemble multiple batches of micro parts into hydrophobic binding sites. By using a numerical simulation tool, we have calculated the surface tension driving force applied on the parts during the assembly, which shows good accordance with our experiments.

In this chapter, we investigate how the surface energy and surface tension forces change with the size. By using the simulation tools, the surface tension forces at different dimensions for assembly can be estimated, and the optimal working domain of this technique can be determined. To work below the optimal domain, a new self-assembly approach has been explored, which can be used to organize and self-assemble objects at the nano scale. Success has been achieved to assemble polystyrene nano beads as small as 100nm. Details are also presented in this chapter on the principle, modelling and experimental design of this nano-assembly approach.

7.1 Scaling effect and self-assembly working domain

When scaling down to micro scale, the significance of various types of forces changes. In order to find the optimal domain for the self-assembly process, we investigate the scale effects on it in this section.

Trimmer's paper [92] compared the scaling effects of different forces. It categorizes the forces into four classes in terms of their scaling behavior represented by a bracket notation as follows:

$$F = \begin{bmatrix} s^1 \\ s^2 \\ s^3 \\ s^4 \end{bmatrix}$$

where s denotes the scale variable and the superscript of s indicates how force scales with s. s^1, s^2, s^3 and s^4 indicate the forces scale in the first, second, third and fourth order of magnitude with the dimension, respectively.

For example, surface tension force falls into the first category, as it scales with length. Chemical reactions, friction and pressure forces scale with the surface area, therefore quadratic with the dimension. The gravitation force, proportional to volume, scales with cubically with dimension. Electrostatic force can be scale linearly or quadratically with the dimension, while magnetic forces can scale quadratic, cubical or quartic with dimension, depending on their operation mode. With the scale effects of the forces (F) and mass ($m = [s^3]$), the scaling effects of other system parameters e.g. energy E, acceleration a, speed v, time t can be derived accordingly as follows:

$$F = \begin{bmatrix} s^1 \\ s^2 \\ s^3 \\ s^4 \end{bmatrix} \qquad E = F \cdot x = \begin{bmatrix} s^2 \\ s^3 \\ s^4 \\ s^5 \end{bmatrix} \qquad a = \tfrac{F}{m} = \begin{bmatrix} s^{-2} \\ s^{-1} \\ s^0 \\ s^1 \end{bmatrix}$$

where x is the distance and $x = s^1$.

As a result, force scaling with the larger order of magnitude, will loose their dominance

$$v = \sqrt{\tfrac{2E}{m}} = \begin{bmatrix} s^{-0.5} \\ s^0 \\ s^{0.5} \\ s^1 \end{bmatrix} \qquad t = \tfrac{x}{v} = \begin{bmatrix} s^{1.5} \\ s^1 \\ s^{0.5} \\ s^0 \end{bmatrix}$$

and become less favorable at micro domain. On the other hand, surface tension, linearly decreasing with length, becomes advantageous at the micro scale, and has been exploited for many applications [48, 49, 52, 93, 94]. It is exploited for our self-assembly technique as well. With surface tension force as s^1, we can derive that the surface energy is s^2 and velocity is $s^{-0.5}$ from Eq. 7.1.

In addition, we characterize the scaling effects quantitatively based on the estimation of the actual forces for our assembly experiments. First, we calibrate the lubricant volume changes with respect to the binding site dimensions. From the lubricant information, we can use the numerical simulation tool to evaluate the surface energy, surface tension forces etc. associated with the assembly process.

Here, we use circular binding sites with diameter of 200μm, 400μm, 500μm and 600μm. Table 7.1 shows the measured lubricant thickness, its standard deviation (STD), variance (VAR), lubricant volume and contact angle of the different binding sites.

Table 7.1: Lubricant information with respect to the binding site diameters including measured lubricant thickness, its standard deviation, its variance, calculated lubricant volume and contact angles.

Diameter (μm)	Thick.(μm)	STD	VAR	Vol. (μm^3)	Contact angle (θ)
200	30.5	2.9643	8.7868	0.000494	33.92°
400	37.9	1.1810	1.3947	0.002408	21.46°
500	41.3	3.2261	10.4079	0.00409	18.75°
600	48.1	3.8509	10.3330	0.00686	18.22°

Fig. 7.1 is a plot of the relationships between the lubricant thickness, contact angle and the size of the binding sites.

From the information in Table 7.1, the surface energy and surface tension forces are determined by simulation, as shown in Fig 7.2. Fig. 7.2(a) shows the energy profiles with respect to the part's lateral displacements for binding sites of different size; while Fig. 7.2(b) shows the corresponding force profiles.

To compare the surface energies at different dimensions, we calculate the change of

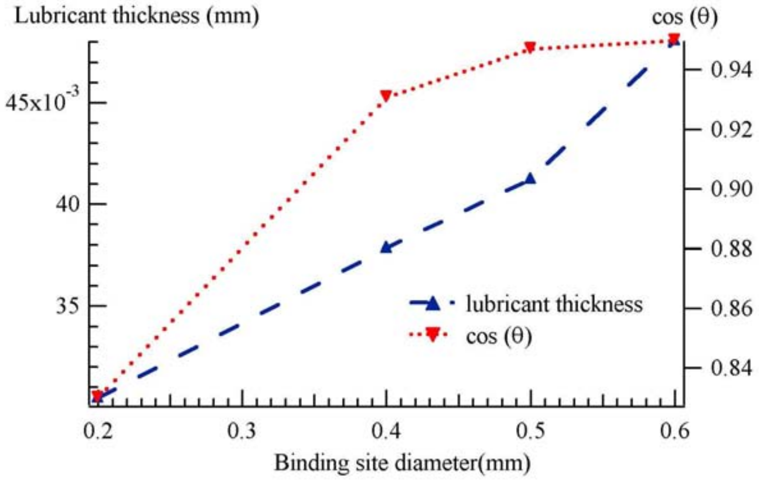

Figure 7.1: Lubricant thickness and contact angles on binding sites of different sizes.

surface energy during the alignment for binding sites with different diameters. We plot the surface energy with respect to the diameter, which is the solid line in Fig. 7.4. In previous discussion, the scaling rule of surface energy is s^2, therefore the surface energy can be calculated as $E = \gamma\pi d^2/4$ shown as dashed line in Fig. 7.4. Supposing the thickness of the circular silicon parts is as same with their diameter, we can calculate the surface tension force and compare it with the gravity force. With the interfacial tension as γ=50mJ/mm^2, we can estimate that the gravitational potential reaches the interfacial energy when the diameter of the binding size is approximately 2.5mm, at which the surface tension force starts to lose its dominance. Hence, the upper bound of the self-assembly working domain can be in the lower millimeter range.

On the other hand, to decide the lower bound of the working domain, we have to consider other factors at smaller dimension. When the dimension of the binding site decreases to the nanometer range, there are other forces that starts to arise, for example, the dissolvability of the lubricant in water; solvation forces, which is a short range force due to the interactions between water molecules and the interface [95]; friction due surface roughness and etc. The dissolvability arises when the binding site size is as big as 100μm, while other factors

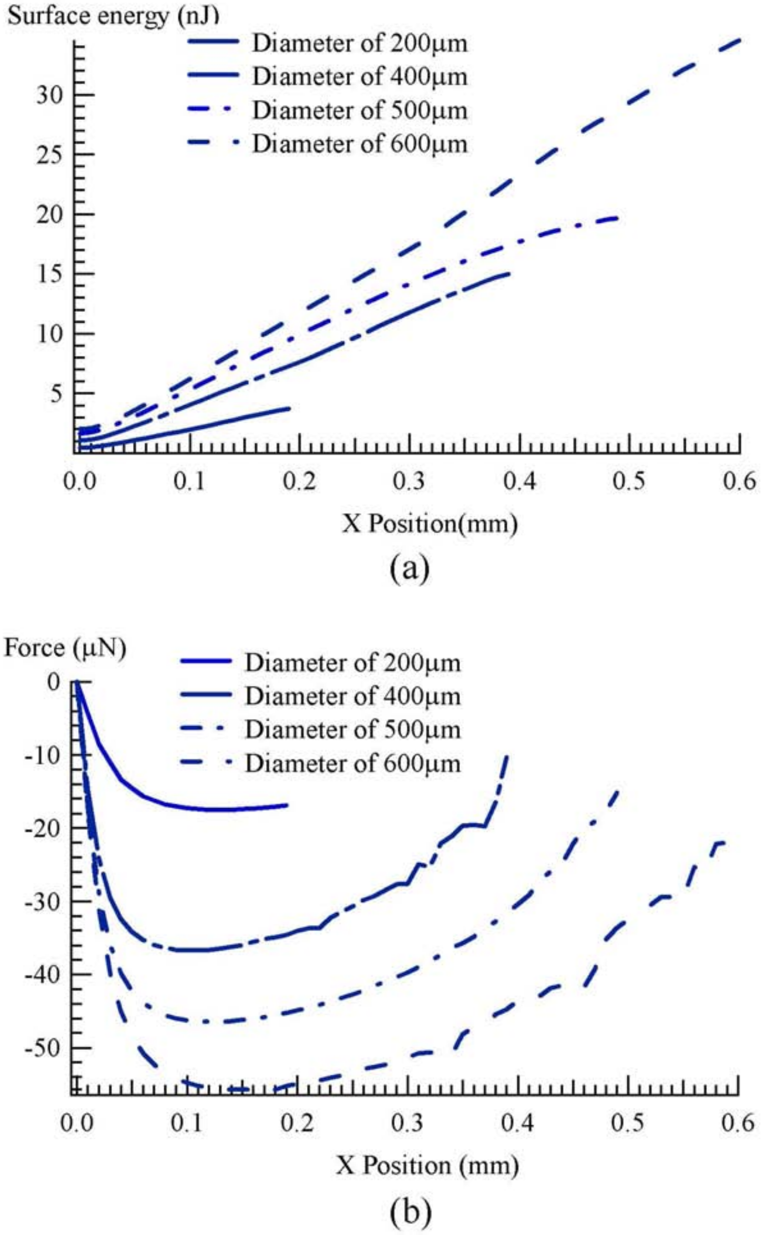

Figure 7.2: (a) Surface energy and (b) surface tension forces change with respect to the part's lateral position for binding site of 200μm, 400μm, 500μm and 600μm.

come into play at much smaller dimension, e.g. solvation forces arises when the liquid film is in the range of nanometer scale. The dissolvability becomes a major concern at the

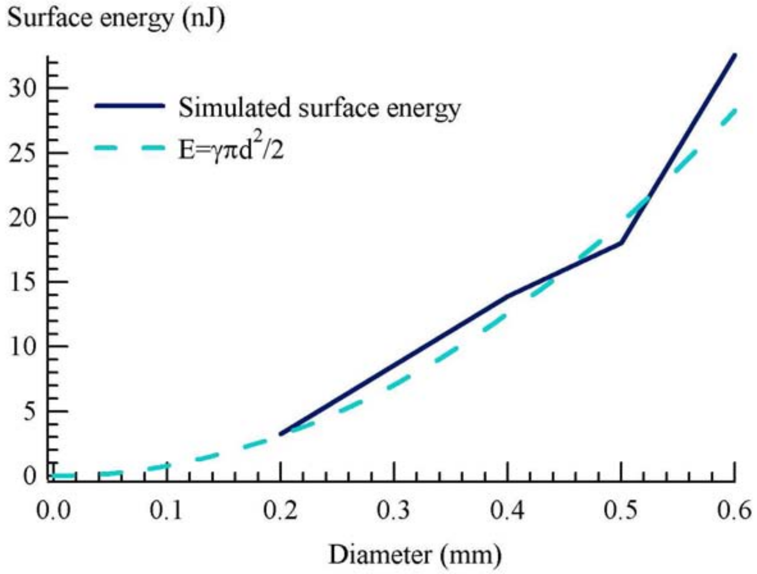

Figure 7.3: Surface energy changes during the alignment process for circular binding sites of 200μm, 400μm, 500μm and 600μm in diameter.

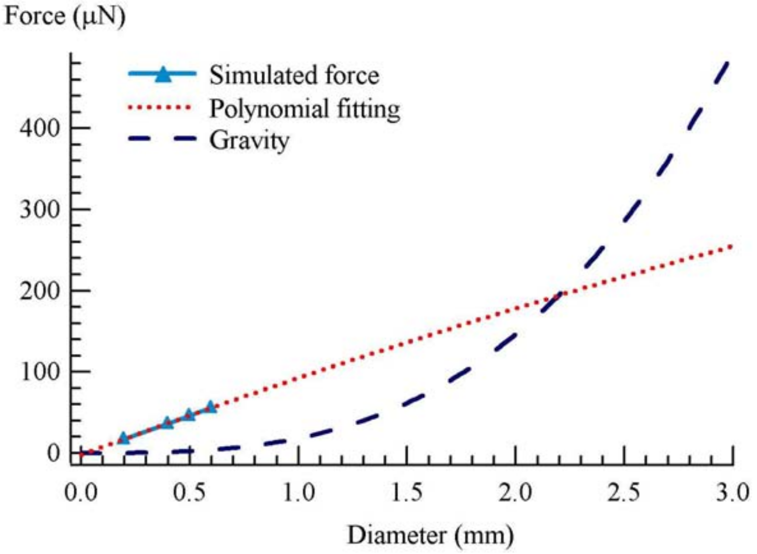

Figure 7.4: Comparison between the surface tension force and the gravity.

micro scale, though it can be negligible at millimeter scale. As the lubricant volume scales down faster than the water-lubricant interfacial surfaces, the dissolvability of the lubricant increases with decreasing dimension. For binding sites with diameter of 100μm, shrinkage of a lubricant is observed after five minutes. When being cured, the lubricant would shrink even more. Therefore, the dimension of the binding site should not be smaller than 100μm. The optimal working domain for self-assembly is between one hundred microns to lower millimeter range.

At the scale smaller than 100μm, self-assembly with a different mechanism is developed, which is discussed in the following section.

7.2 Self-assembly at the nano scale

With recent successful developments in functional nano-structures, e.g. nano-bead or carbon-nanotube sensors, their control and manipulation at the nano-scale becomes a challenging problem. A variety of self-assembly methods have been demonstrated by using biological, chemical, electrical or magnetic driving forces [47, 77, 96, 97]. All these approaches require specific treatments or coatings of the nano-devices. For example, single stranded DNA has been attached to nano-beads to create the driving force from DNA strand binding [47]. In this paper, we discuss a method to self-assemble and arrange nano-beads using surface tension.

To use the surface tension force at smaller scale, we adapt this micro fluidic assembly technique into the nano-domain by taking advantage of water air interfacial energy. Different from prior work at the micro-scale using liquid-liquid interfacial energy, the self-assembly is achieved by using colloid aggregation at the air-water interface [98, 99]. By controlling the colloid volume and dilution, the aggregation of beads can be precisely arranged into nano-structures that are one to two orders of magnitude smaller than the original pattern. In addition, this technique can be applied to general nano-devices without specific surface treatment.

7.2.1 Principle and models

Fig. 7.5 illustrates the self-assembly process. The substrate is prepared with hydrophilic patterns on hydrophobic background (Fig. 7.5(a)). When the substrate covered with the colloid passes through the air-water interface, the excessive colloid is removed from the substrate and the colloid wets exclusively the hydrophilic areas (Fig. 7.5(b)). As a result of surface tension force and dragging effect from the receding air-water interface due to evaporation (Fig. 7.5(c)), the nano-beads are arranged on the surface in predictable patterns (Fig. 7.5(d)).

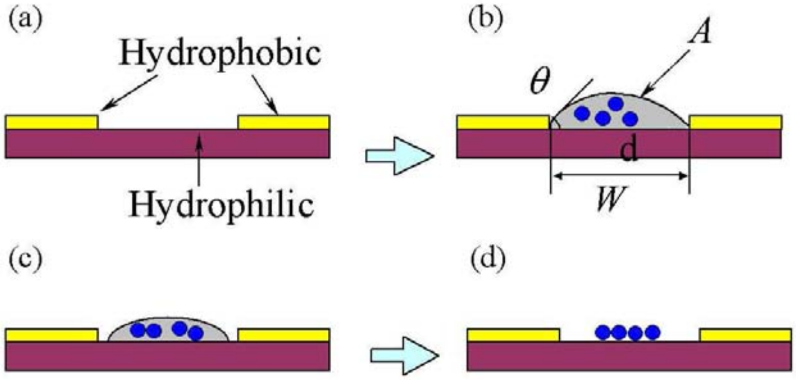

Figure 7.5: (a) A substrate prepared with hydrophilic binding sites on hydrophobic background. (b) When the colloid is applied, it wets the hydrophilic binding pattern. (c) With the evaporation of water, the beads are dragged towards the center of the droplet. (d) The structure formed by the beads aggregating in the center of the binding pattern.

With constant bead concentration C, we can estimate the number N of beads deposited on the hydrophilic areas as:

$$N = C \times V/V_b \tag{7.1}$$

where V and $V_b = \pi a^3/6$ are the respective volumes of the colloid droplet and the bead with diameter a. More accurate calculations of N will take into account the droplet shape on the hydrophilic template. In this paper, we discuss models for two basic template patterns: rectangles and circular shapes.

Rectangular pattern model

Suppose the hydrophilic rectangular pattern is $L \times W$, with $L \gg W$. The number of beads per unit length can be calculated by taking a segment of the colloid droplet with the length of a, which is the diameter of the beads (Fig. 7.6(a)); the area of the colloid droplet cross-section is A and the volume of the droplet segment is V, which can be derived as:

$$\begin{aligned} A &= \frac{W^2(\theta \sin^2\theta - \cot\theta)}{4} \\ V &= A \times a \end{aligned} \tag{7.2}$$

where θ is the contact angle of the colloid on the hydrophilic area.

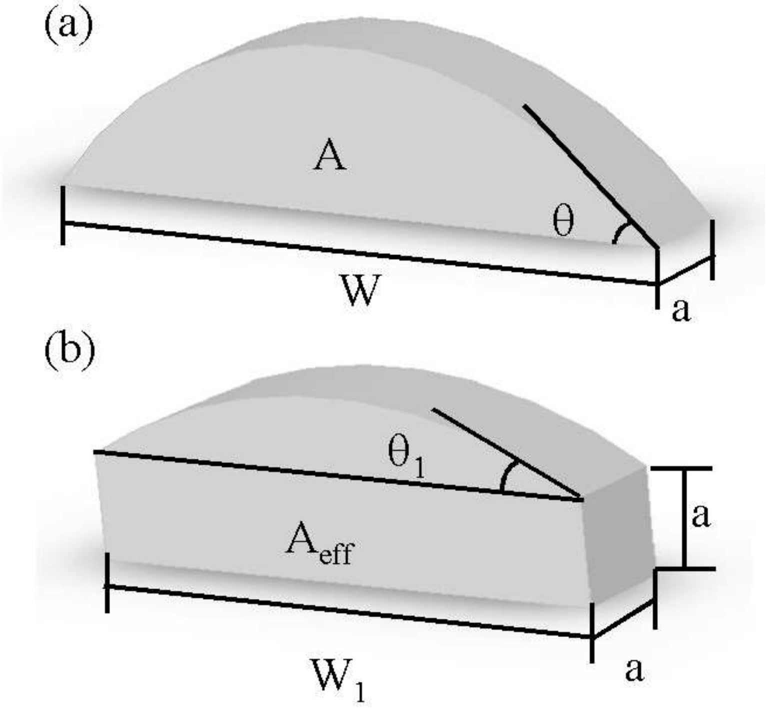

Figure 7.6: (a) Three-dimensional model of the colloid droplet segment formed on a rectangular pattern. (b) The effective volume of the droplet. A_{eff} is the effective cross section area.

Beads of diameter d cannot occupy regions of the volume that have a minimum dimension smaller than d. Therefore, determining the number of beads simply by applying Eqs. 7.2

Table 7.2: Effective area A_{eff} ratio changes with respect to the bead size a, when the contact angle θ is 20°.

Bead size ratio (a/W)	Effective area ratio (A_{eff}/A)
0.0100	0.9951
0.0200	0.9797
0.0300	0.9517
0.0400	0.9089
0.0500	0.8474
0.0600	0.7611
0.0700	0.6380
0.0800	0.4458

would create a significant error. The effective volume V_{eff} of the droplet that can include beads is in general smaller than V. As shown in Fig. 7.6(b), the effective volume V_{eff} which the beads can occupy is $V_{eff} = A_{\text{eff}} \times a$, where the effective cross-section area is A_{eff}.

$$A = \frac{W_1^2(\theta_1 \sin^2 \theta_1 - \cot \theta_1)}{4} \tag{7.3}$$

where

$$\begin{aligned} W_1 &= 2\sqrt{(\frac{W}{2\sin\theta} - \frac{W\cot\theta}{2} - a)(\frac{W}{2\sin\theta} + \frac{W\cot\theta}{2} + a)} \qquad (7.4) \\ \theta_1 &= \arcsin\left(\frac{W_1\sin\theta}{W}\right) \qquad (7.5) \end{aligned}$$

With the same rectangular binding sites, the effective area A$_{\text{eff}}$ varies with respect to the bead size a, which is illustrated in Table 7.2.1.

The number of beads per length can be estimated as:

$$\begin{aligned} N &= C \times \frac{V_{eff}}{V_b} \\ &= C \times \frac{A_{eff} \times a}{V_b} \\ &= \frac{6C \times A_{eff}}{\pi d^2} \end{aligned} \tag{7.6}$$

(7.7)

Circular pattern model

Fig. 7.7 shows the three-dimensional model of a colloid droplet on a circular hydrophilic pattern. Similar to the discussion of the rectangular pattern above, we determine the number of beads deposited on a circular binding site with diameter a as

$$N = \frac{C \times d^3((\frac{1}{\sin\theta - cot\theta})(3 + (\frac{1}{\sin\theta} - \cot\theta)^2)}{8d^3} \tag{7.8}$$

From Eqs. 7.6- 7.8, we can calculate the number of aggregated beads on patterns of various sizes. Conversely, control of the nano-bead aggregate dimensions can be achieved by specific design of the hydrophilic patterns with respect to the bead size and bead concentration.

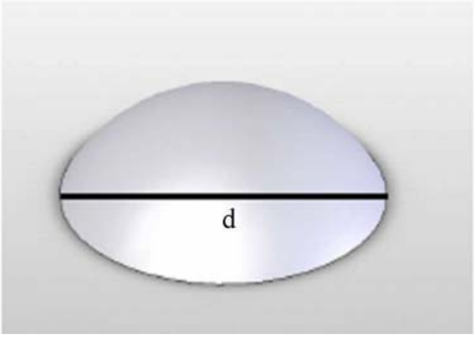

Figure 7.7: A three-dimensional model of the colloid droplet on a circular pattern with diameter d.

7.2.2 Experimental setup

The substrate is prepared with a thermal oxidation layer of 400nm on a silicon wafer. Then a thin layer of TiW/Au (30nm) is sputtered and patterned by photolithography and Au/TiW etching for 20s to expose the hydrophilic silicon oxide patterns. It is cleaned by two minutes of oxygen plasma, followed by soaking in 1mM ethanolic dodecanethiol solution to make the Au background hydrophobic. Colloid is then applied to cover the entire substrate, before the substrate touches the air-water interface, which removes the excessive colloid from the surface (Fig 7.8). In this step, the colloid is cleared from the hydrophobic area. Afterwards only the hydrophilic binding sites remain wetted. After the water evaporates in air, nano-beads are patterned on the binding sites. We use polystyrene nano-beads (Bangs Laboratories, Inc.) with the size ranging from 100nm to 10μm.

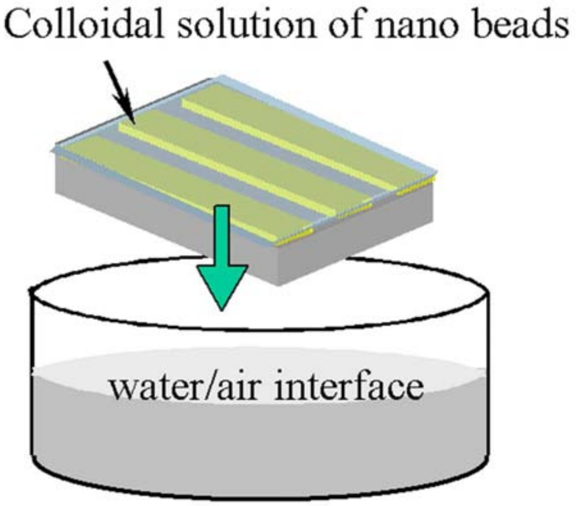

Figure 7.8: The substrate with colloid is moved toward to water-air interface. When it touches the interface, the excessive colloid will be removed except on the hydrophilic areas.

7.2.3 Results

Experimental results show agreement with our models. With the same bead size and concentration, different three-dimensional structures are observed. Fig. 7.9 shows results of various nano-structures formed from colloid with 10 wt.% 290nm beads on different binding shapes and sizes. For comparison, we calculated the number of beads based on the models discussed in the previous section, with the contact angle θ of water on silicon dioxide at the range of 12°∼20°. Table 7.2.3 shows both the calculated and experimental values.

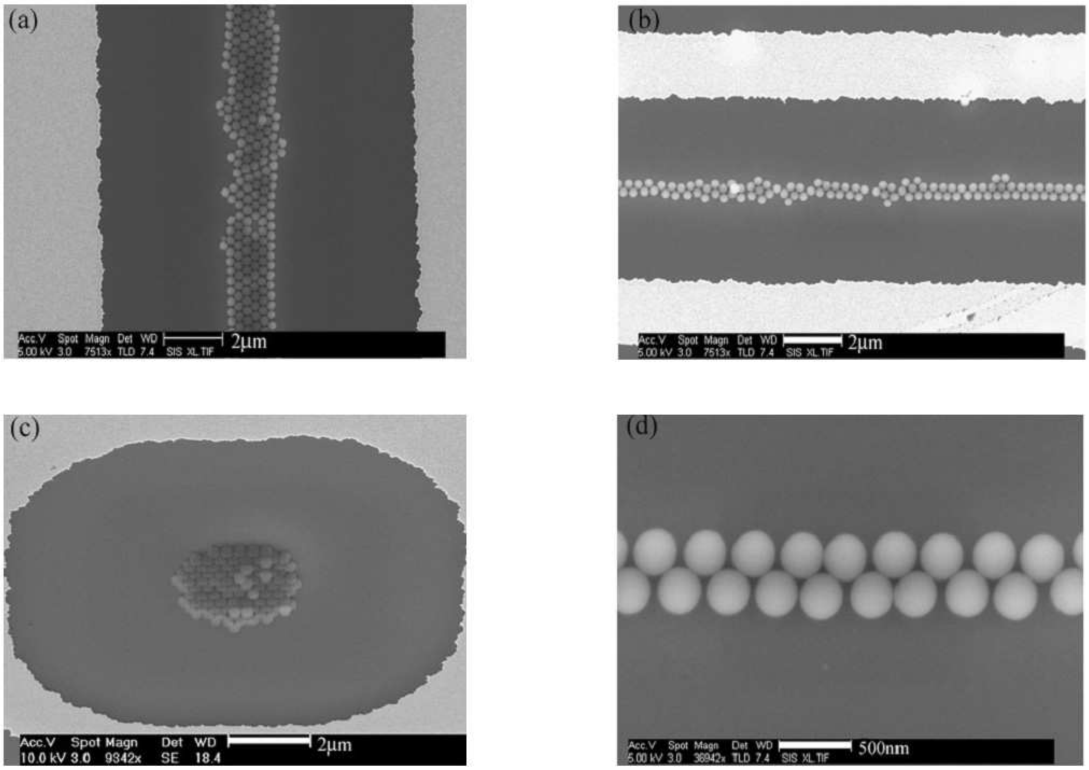

Figure 7.9: SEM images of nano-structures formed with 290nm beads on different patterns. Arrays of beads on a rectangular shape with (a) $W = 10\mu$m and (b) $W = 6\mu$m. (c) Beads arrange concentric to the circular binding site with diameter of 7μm. (d) A zoomed-in image of a double-strand bead array.

For similar binding sites, different bead sizes can result in significant changes in the aggregated nano-structures. Figs. 7.10(a)-(c) show the different nano-structures formed on identical patterns with 100nm, 290nm and 1μm beads. On circular binding sites with diameter of approximately 100μm, the aggregated structures formed by 1μm and 10μm are

Table 7.3: Comparisons between calculated and experimental data of nano-structure sizes formed from colloid with 10 wt.% 290nm beads.

Binding site shape	Rectangle	Rectangle	Circle
Size	$W = 10\mu\text{m}$, $L \gg W$	$W = 6\mu\text{m}$, $L \gg W$	$d = 7\mu\text{m}$
Cal. N (# of beads)	6∼12	1∼4	55∼94
Exp. N (# of beads)	5∼6	2∼3	101

rings and disks, respectively (Fig. 7.11). With different bead sizes and concentrations but similar binding site dimensions, the patterns can be drastically different: a discontinuous 1μm single bead line (Fig. 7.12(a)) formed by 1wt.% concentration colloid and multiple layered 100 nm nano-structures (Fig. 7.12(b)) forme by 10wt.% concentration colloid.

When being heated to the melting point, the nano-beads will reflow and form different structures. As an example, we heated the samples shown in Fig. 7.13(a), which were lines formed with 10μm beads on rectangular patterns with the width of approximately 40μm. After being heated on a hotplate for 30 seconds at 200°, the three dimensional nano-beads structures will change into polystyrene formed with melted beads (Fig. 7.13(b)).

7.2.4 Summary

As a summary, we have investigated the scaling effects of the self-assembly method in this section. Based on the analysis of the surface energy and surface tension forces, the optimal working domain of this technique can be derived: between hundreds of microns to several millimeter. This result gives us the insight of the self-assembly technique. It can be used as the design rule for the applications of our self-assembly approach.

In addition, we have developed a new self-assembly method at the nano scale, which has demonstrates the capability of organizing polystyrene nano-beads on micron scale binding sites. The hydrophilic binding sites, which are patterned on a hydrophobic background, are covered with colloidal droplets as a result of the colloidal aggregation on the water-air interface. By varying the bead dimension and concentration, we can control the not only the

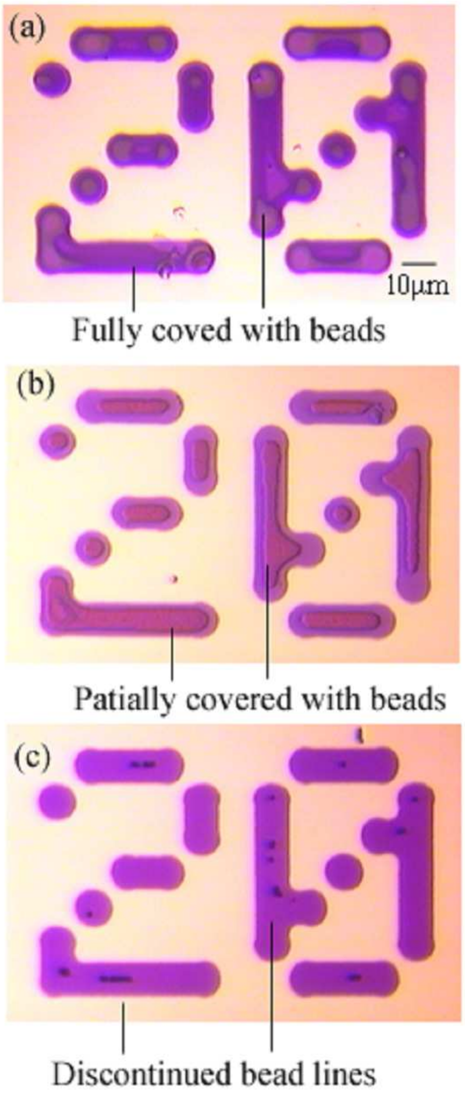

Figure 7.10: Different nano-structures formed on identical patterns by beads of different sizes: (a) 100nm (b) 290nm (c) 1μm in diameter. Note: the pattern in (a) is packed with multiple layers of beads, showing as different shadows.

sizes of the three dimensional structures but also the structure profiles formed on the binding sites. The advantages of this technique include: (1) simple surface patterning techniques suffice to construct the binding templates for nano-scale structures; (2) no specific surface treatment is required for the beads; (3) with the proposed models, we can predict and

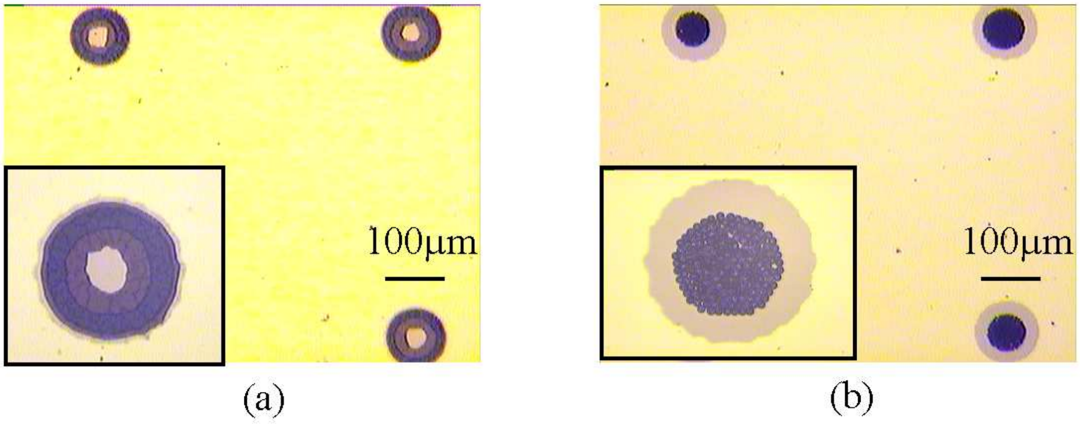

(a)

(b)

Figure 7.11: With circular binding sites of 100μm, the 3D structures formed by 1μm and 10μm are (a) ring shapes and (b) circular shapes, respectively. The inserted left bottom images of each figure are zoomed pictures of the three dimensional structures.

control the shape of the three-dimensional structures.

This technique can be applied as an enabling technology for building nano-systems, e.g. nano-bead based biochemical sensing elements. More generally, it can be used as a nanofabrication technique for transforming micro patterns into nano-structures at one to two size scales below the optical lithography limit. This could lead to new, low-cost methods in the manufacture of nanoscale masks and circuits.

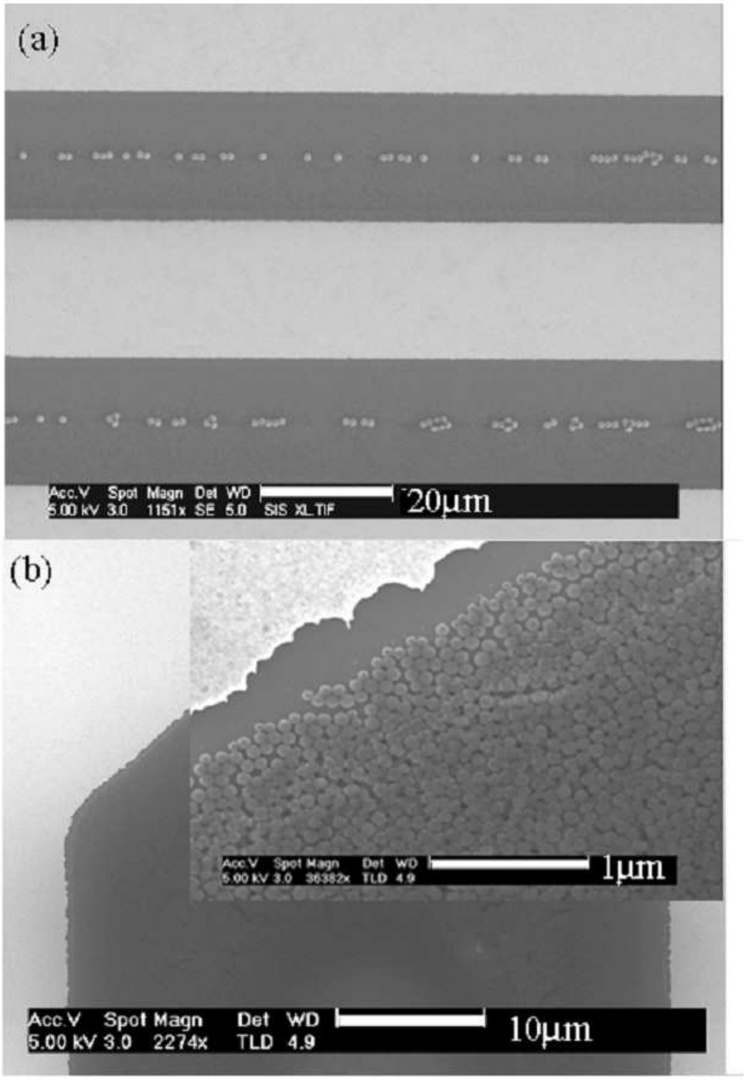

Figure 7.12: Binding sites with similar size result in different nano-structures formed by different beads and different concentrations: (a) 1 wt.% concentration 1μm beads form single sparse line, (b) 10 wt.% concentration 100nm beads form multi-layer nano-structure.

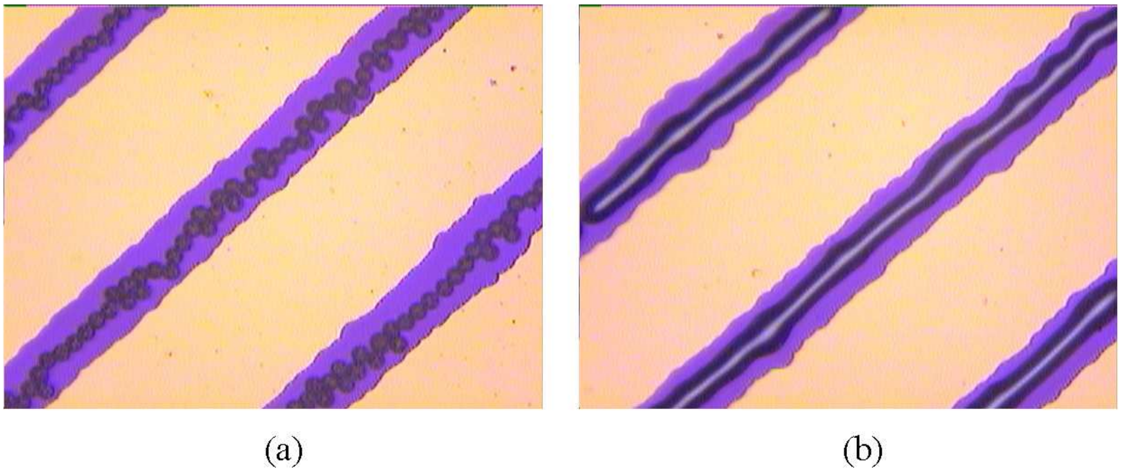

Figure 7.13: (a) Aggregated 10μm beads on lines with a width of 40μm. (a) 10μm bead lines formed by melted 10μm beads. The line shape follows the zigzag boundary shape of the binding site.

Chapter 8

SUMMARY AND DISCUSSIONS

We have established a protocol based on capillary force and surface hydrophobicity modulation for multi-batch micro self-assembly. The previous chapters discussed the important aspects of this self-assembly approach: the principle of the assembly; fabrication process developments; experimental implementation of the self-assembly process; simulations of surface energy and surface tension driving forces for the self-assembly process; geometric binding site designs to achieve alignment uniqueness; self-assembly alignment uniqueness; electrochemical surface modification and electroplating methods; the scaling effect of the technique and the possible extension into the nano domain.

In particular, we would like to discuss the following important issues of electrochemical surface modification and electroplating; optimal binding site design; and scaling effects in the following sections.

8.1 Electrochemical surface modification and electroplating

The electrochemical surface modification method provides means of engineering the surface properties at the micro scale. As a key component incorporated with the existing self-assembly techniques, it makes multi-batch assembly possible. Electrochemical desorption of SAM from Au has demonstrated the ability of changing surface hydrophobicity, thus altering the driving force for assembly. In addition, with the binding sites being electrically addressable, the desorption can be controlled on each individual binding site by applying potential bias. Experimental details are discussed in Chapter 6. Based on characterization of different alkanethiol desorption, dodecanethiol is selected as it forms a stable monolayer for assembly while taking a reasonable time to desorb.

The electroplating method is compatible with the parallel assembly process, and simultaneously establishes electrical connectivity for assembled components. In Chapter 6, two connections of LEDs have been established. In addition, the plated solder might provide a stronger bond between the part and substrate by reflowing the solder.

8.2 Optimal binding site design

In Chapter 5, we discuss the binding site design problem. The goal is to find optimal designs with unique alignment position and orientation. We use a first order approximation model to calculate the surface energy in terms of overlap area. From the analysis of simulation results, we can derive that symmetric rings with the constraint $r_s \leq 0.442891\ r_b$ can achieve a unique alignment position, where r_s and r_b are the radii of the inner cutout and outer circle, respectively. Furthermore, a class of optimal designs is found consisting of asymmetric rings with additional geometric constraints.

In practice, experiments are performed to test these designs, and accordant results have been obtained [100].

8.3 Scaling effects

Another important issue of the assembly is the scaling effect. In Chapter 7, we have derived the scaling rules for the self-assembly systems. In our experiments, assembly parts are in the millimeter scale. In [60,61], parts are in the range of 150-400μm and in [55] parts are up to 5mm in size. These self-assembly methods are with part sizes ranging from hundreds of micrometers to several millimeters. With the lubricant thickness scaling with the binding site size, the driving force changes as well. We have calculated the scaling effects of surface energy and surface tension forces at the range of hundreds of microns. From the force simulations and experimental observations of the lubricant dissolvability, we derive that the working domain for this technique is from 100μm to several millimeters.

8.4 Multi-batch assembly

By repeating the surface modification and self-assembly steps, multiple batches of parts can be assembled on the substrate. Assembly of two batches of Si part($1\times1\text{mm}^2$) has been achieved. When used for hybrid integration, this assembly can achieve high efficiency with high batch volume. In principle, the process cycle of SAM adsorption, selective desorption, and controlled self-assembly can be repeated multiple times to build up increasingly complex microsystems.

8.5 Future directions

As an enabling technique, the assembly approach is applicable to generic parts such as surface mount LEDs. We believe that parallel micro self-assembly is feasible and essential for the production of microsystems. There are two major future directions of this technique: application development and technique extension. To apply this technique to practical applications, several critical issues we have to be addressed:

For application development, a critical issue is the choice of lubricant. For self-assembly, the lubricant has to have low surface tension and low viscosity, which can help the part to align during the assembly process. In addition, studies show how the polymerization affects the final alignment [101, 102]. As a result, the alignment error increases with the polymerization shrinkage and lubricant thickness. Therefore, lubricant with smaller shrinkage in the polymerization process is preferable. On the other hand, the polymerized lubricant, acting as a glue to bond the part after assembly, has to provide certain a strength for the assembled parts.

Another practical issue about the assembly technique is the yield. The yield is largely determined by the assembly setup. Several methods can be used to improve the yield [59,60]. To achieve high yield on the substrate binding site occupancy, a large number of excess parts are provided into the system. Yield can also be improved by using recycling of the unassembled parts and repeating the assembly step. Agitation is another way to improve the yield. With agitation in the vertical direction [59, 60], the parts initially upside-down can be assembled.

The second direction of this technique is the extension of the self-assembly. With devices of decreasing size, control and manipulation of micro and even nano devices has become a challenge. An example of extending the surface-tension driven self-assembly to the nano domain has been presented in Chapter 7. Initial results have shown the feasibility of assembling nano and micro beads into regular patters: line, disk, rings, etc., by taking advantage of air-water interfacial forces. Further work would include: the study of a dynamic model of the assembly, assembly experiments of nano beads of different materials or nano objects of different geometries (nano wires and nano tubes) for the purpose of developing a general nano-assembly method.

We have investigated an approach to construct nano-structures by colloidal aggregation, with accordant simulation and experimental results. This technique can be applied as an enabling technology for building nano-systems, e.g. nano-bead based biochemical sensing elements. More generally, it can be used as a nanofabrication technique for transforming micro patterns into nano-structures at one to two size scales below the optical lithography limit. This could lead to new, low-cost methods in the manufacture of nanoscale masks and circuits.

Self-assembly brings together the macro, micro and the nano scales, by using surface tension forces. With the success of multi-batch assembly at the micro scale, it is anticipated to be applicable to a wide range of micro and nano parts made of different materials, for the integration and packaging of complex heterogeneous systems.

BIBLIOGRAPHY

[1] K. E. Petersen, “Silicon as a mechanical material,” in *Proceedings of the IEEE*, pp. 58–95, 1982.

[2] F. Goodenough, “Airbags boom when IC accelerometer sees 50 g.,” *Electronic Design*, vol. 39, no. 15, 1991.

[3] B. E. Boser and R. T. Howe, “Surface micromachined accelerometers,” *IEEE Journal of Solid-State Circuits*, vol. 31, no. 3, 1996.

[4] Analog Devices, http://www.analog.com
Analog Devices, One Technology Way P. O. Box 9106 Norwood, MA 02062-9106.

[5] Seiko Epson Corporation, http://www.epson.com
Seiko Epson Corporation, 3-3-5 Owa, Suwa, Nagano, Japan 392-8502.

[6] Texas Instruments DLP Products,
http://www.dlp.com/dlp_technology/dlp_technology_chip_details.asp
Texas Instruments, 6550 Chase Oaks Blvd Plano, TX 75023.

[7] G. M. Rebeiz, *RF MEMS: Theory, Design and Technology.* John Wiley and Sons, 2003.

[8] D. J. Anderson, K. Najafi, S. J. Tanghe, D. A. Evans, K. L. Levy, J. F. Hetke, X. Xue, J. J. Zappia, and K. D. Wise, “Batch fabricated thin-film electrodes for stimulation of the central auditory system,” *IEEE Trans. Biomed. Eng.*, vol. 36, pp. 693–704, 1989.

[9] G. A. Kovacs, C. W. Storment, M. Halks-Miller, C. R. Belczynski Jr., C. C. D. Santina, E. R. Lewis, and N. I. Maluf, “Silicon-substrate microelectrode arrays for

parallel recording of neural activity in peripheral and cranial nerves.," *IEEE Trans. Biomed. Eng.*, vol. 41, pp. 567–577, 1994.

[10] Y. Hanein, C. G. J. Schabmueller, G. Holman, P. Luecke, D. D. Denton, and K. F. Böhringer, "High-aspect ratio submicrometer needles for intracellular applications," *IOP Journal of Micromechanics and Microengineering (JMM)*, vol. 13, no. 4, pp. S1–S10, July 2003.

[11] G. MacBeath and S. L. Schreiber, "Printing proteins as microarrays for high-throughput function determination," *Science*, vol. 28, pp. 1760–1763, 2000.

[12] J. Lee, H. Moon, J. Fowler, T. Schoellhammer, and C.-J. Kim, "Electrowetting and electrowetting-on-dielectric for microscale liquid handling," *Sensors and Actuators A*, vol. 95, pp. 259–268, 2002.

[13] S. K. Cho, S.-K. Fan, H. Moon, and C.-J. Kim, "Toward digital microfluidic circuits: Creating, transporting, cutting and merging liquid droplets by electrowetting-based actuation," in *Proc. IEEE Conf. MEMS*, (Las Vegas, NV), pp. 32–35, Jan. 2002.

[14] S. K. Cho, H. Moon, and C.-J. Kim, "Creating, transporting, cutting, and merging liquid droplets by electrowetting-based actuation for digital microfluidic circuits," *Journal of Microelectromechanical Systems*, vol. 12, no. 1, pp. 70–80, Feb. 2003.

[15] W. Yun, R. Howe, and P. Gray, "Surface micromachined, digitally force-balanced accelerometer with integrated cmos detection circuitry," in *Proc. IEEE Solid-State Sensor and Actuator Workshop*, pp. 126–131, 1992.

[16] J. H. Smith, S. Montague, and J. J. Sniegowski, "Material and processing issues for the monolithic integration of microelectronics with surface-micromachined polysilicon sensors and actuators," in *Micromachining and Microfabrication 95, SPIE*, Oct. 1995.

[17] T. Wipiejewski, Y. Akulova, G. Fish, C. Schow, P. Koh, A. Karim, S. Nakagawa, A. Dahl, P. Kozodoy, A. Matson, B. Short, C. Turner, S. Penniman, M. Larson,

C. Coldren, and L. Coldren, "Integration of active optical components.," in *Proc. SPIE, Vol. 4997*, (San Jose, California), pp. A–02, January 2003.

[18] Y.-C. Tseng, P. Xuan, A. Javey, R. Malloy, Q. Wang, J. Bokor, and H. Dai, "Monolithic integration of carbon nanotube devices with silicon mos technology.," *Nano Letters*, vol. 4, no. 1, pp. 123 –127, 2004.

[19] M. B. Cohn, *Assembly Techniques for Microelectromechanical Systems. Ph.D Thesis.* University of California at Berkeley, Department of Electrical Engineering and Computer Sciences, 1997.

[20] R. S. Fearing, "Survey of sticking effects for micro-parts," in *Proc. IEEE/RSJ Int. Conf. on Robotics and Intelligent Systems (IROS)*, (Pittsburg, PA), pp. 212 –217, 1995.

[21] K. Saitou, D. A. Wang, and S. J. Wou, "Externally resonated linear microvibromotor for microassembly," *ASME/IEEE J. of Microelectromechanical Systems*, vol. 9, no. 3, pp. 336–346, 2000.

[22] S. J. Ralis, B. Vikramaditya, and B. J. Nelson, "Micropositioning of a weakly calibrated microassembly system using coarse-to-fine visual servoing strategies," *IEEE Transactions on Electronics Packaging Manufacturing*, vol. 23, no. 2, pp. 123 –131, 2000.

[23] G. Yang, J. A. Gaines, and B. J. Nelson, "A flexible experimental workcell for efficient and reliable wafer-level 3D micro-assembly," in *Proc. IEEE International Conference on Robotics and Automation (ICRA)*, (Seoul, South Korea), pp. 133 – 138, 2001.

[24] J. A. Thompson and R. S. Fearing, "Automating microassembly with ortho-tweezers and force sensing," in *Proc. IEEE/RSJ International Conference on Intelligent Robots and Systems (IROS)*, (Maui, HI), pp. 1327 –1334, 2001.

[25] M. Sitti, "Survey of nanomanipulation systems," in *IEEE-Nanotechnology Conference*, (Maui, USA), Nov. 2001.

[26] Zyvex Corporation, http://www.zyvex.com
Zyvex Corporation 1321 N. Plano Road, Richardson, Texas 75081 .

[27] B. Mokaberi and A. A. G. Requicha, "Towards automatic nanomanipulation: drift compensation in scanning probe microscopes," in *IEEE Int'l Conf. on Robotics and Automation*, (New Orleans, LA), April 25-30, 2004.

[28] M. B. Cohn, K. F. Böhringer, J. M. Noworolski, A. Singh, C. G. Keller, K. Y. Goldberg, and R. T. Howe, "Microassembly technologies for MEMS," in *Proc. SPIE Micromachining and Microfabrication*, (Santa Clara, CA), pp. 2–16, 1998.

[29] A. Singh, D. A. Horsley, M. B. Cohn, A. P. Pisano, and R. T. Howe, "Batch transfer of microstructures using flip-chip solder bonding," *ASME/IEEE J. of Microelectromechanical Systems*, vol. 8, no. 1, pp. 27–33, 1999.

[30] A. S. Holmes and S. M. Saidam, "Sacrificial layer process with laser-driven release for batch assembly operations," *ASME/IEEE J. of Microelectromechanical Systems*, vol. 7, no. 4, pp. 416–422, 1998.

[31] G. M. Whitesides and B. Grzybowski, "Self-assembly at all scales," *Science*, vol. 295, pp. 2418–2421, 2002.

[32] L. J. Barbour, G. W. Orr, and J. L. Atwood, "An intermolecular $(\mathrm{H_2O})_{10}$ cluster in a solid-state supramolecular complex," *Nature*, vol. 393, pp. 671 – 673, 1998.

[33] J. M. Lehn, "Supramolecular chemistry," *Science*, vol. 260, no. 5115, pp. 1762–1763, 1993.

[34] H. J. Yeh and J. S. Smith, "Fluidic assembly for the integration of GaAs light-emitting diodes on Si substrates," *IEEE Photonics Technology Letters*, vol. 46, pp. 706–709, 1994.

[35] J. K. Tu, J. J. Talghader, M. A. Hadley, and J. S. Smith, "Fluidic self-assembly of InGaAs vertical cavity surface emitting lasers onto silicon," *Electronics Letters*, vol. 31, pp. 1448–1449, 1995.

[36] Alien Technology, http://www.alientechnology.com
Alien Technology, 18220 Butterfield Boulevard, Morgan Hill CA 95037 .

[37] M. Tanase, D. M. Silevitch, A. Hultgren, L. A. Bauer, P. C. Searson, G. J. Meyer, and D. H. Reich, "Magnetic trapping and self-assembly of multicomponent nanowires," *Journal of Applied Physics*, vol. 91, no. 10, pp. 8549–8551, 2002.

[38] B. Yellen and G. Friedman, "Magnetic driven assembly of colloidal particles onto patterned surfaces," in *Technical Proceedings of the 2003 Nanotechnology Conference and Trade Show, Vol. 3*, (San Francisco , California, U.S.A.), pp. 542 – 545, 2003.

[39] B. Yellen, G. Friedman, and A. Feinerman, "Printing superparamagnetic colloidal particle arrays on patterned magnetic film," *Journal of Applied Physics*, vol. 93, no. 10, pp. 7331–7333, 2003.

[40] K. F. Böhringer, R. S. Fearing, and K. Y. Goldberg, "Microassembly," in *The Handbook of Industrial Robotics* (S. Nof, ed.), pp. 1045–1066, John Wiley & Sons, 2nd ed., February 1999.

[41] F. Caruso, H. Lichtenfeld, M. Giersig, and H. Möhwald, "Electrostatic self-assembly of silica nanoparticle-polyelectrolyte multilayers on polystyrene latex particles," *Journal of the American Chemistry Society*, vol. 120, pp. 8523–8524, 1998.

[42] K. F. Böhringer, K. Y. Goldberg, M. B. Cohn, R. T. Howe, and A. P. Pisano, "Parallel microassembly using electrostatic force fields," in *IEEE International Conference on Robotics and Automation (ICRA)*, (Leuven, Belgium), pp. 483 – 496, 1998.

[43] J. Tien, A. Terfort, and G. M. Whitesides, "Microfabrication through electrostatic self-assembly," *Langmuir*, vol. 13, no. 20, pp. 5349–5355, 1997.

[44] B. A. Grzybowski, A. Winkleman, J. A. Wiles, Y. Brumer, and G. M. Whitesides, "Electrostatic self-assembly of macroscopic crystals using contact electrification," *Nature materials*, vol. 2, no. April, pp. 241–245, 2003.

[45] M. N. Yousaf, B. T. Houseman, and M. Mrksich, "Using electroactive substrates to pattern the attachment of two different cell populations," *Proceedings of the National Academy of Sciences of the United States of America (PNAS)*, vol. 98, no. 11, pp. 5992–5996, 2001.

[46] Y. Wang, X. Cheng, Y. Hanein, A. Shastry, D. D. Denton, B. D. Ratner, and K. F. Böhringer, "Selective attachment of multiple cell types on thermally responsive polymer.," in *The 12th International Conference on Solid-State Sensors and Actuators (Transducers'03)*, (Boston, MA), June 6-12, 2003.

[47] H. McNally, M. Pingle, S. Lee, D. Guo, D. Bergstrom, and R. Bashir, "Self-assembly of micro- and nanoscale particles," *Applied Surface Science*, vol. 214, pp. 109–119, 2003.

[48] A. A. Darhuber, S. M. Troian, and S. Wagner, "Physical mechanisms governing pattern fidelity in microscale offset printing," *Journal of Applied Physics*, vol. 90, no. 7, pp. 3602–3609, 2001.

[49] A. A. Darhuber, S. M. Troian, J. M. Davis, S. M. Miller, and S. Wagner, "Selective dip-coating of chemically micropatterned surfaces," *Journal of Applied Physics*, vol. 88, no. 9, pp. 5119–5126, 2000.

[50] J. Lee and C. J. Kim, "Surface-tension-driven microactuation based on continuous electrowetting," *ASME/IEEE J. of Microelectromechanical Systems*, vol. 9, no. 2, pp. 171–180, 2000.

[51] K. F. Harsh, R. S. Irwin, and Y. C. Lee, "Solder self-assembly for MEMS," in *Proceedings of the 1998 International Instrumentation Symposium (ISA)*, (Reno, NV), pp. 256–261, 1998.

[52] D. M. Hartmann, O. Kibar, and S. C. Esener, "Optimization and theoretical modelling of polymer microlens arrays fabricated with the hydrophobic effect," *Appl. Opt.*, vol. 40, pp. 2736–2746, 2001.

[53] R. R. A. Syms, E. M. Yeatman, V. M. Bright, and G. M. Whitesides, "Surface tension-powered self-assembly of microstructures - the state-of-the-art," *IEEE/ASME Journal of Microelectromechanical Systems*, vol. 12, no. 4, pp. 387 – 417, 2003.

[54] U. Srinivasan, M. A. Helmbrecht, C. Rembe, R. S. Muller, and R. T. Howe, "Fluidic self-assembly of micromirrors onto microactuators using capillary forces," *IEEE Journal On Selected Topics In Quantum Electronics*, vol. 8, no. 1, pp. 4–11, 2002.

[55] D. Gracias, J. Tien, T. L. Breen, C. Hsu, and G. M. Whitesides, "Forming electrical networks in three dimensions by self-assembly," *Science*, vol. 289, pp. 1170–1172, 2000.

[56] A. Terfort, N. Bowden, and G. M. Whitesides, "Three-dimensional self-assembly of millimetre-scale components," *Nature*, vol. 386, pp. 162–164, 1997.

[57] A. Terfort and G. M. Whitesides, "Self-assembly of an operating electrical circuit based on shape complementarity and the hydrophobic effect," *Advanced Materials*, vol. 10, no. 6, pp. 470–473, 1998.

[58] U. Srinivasan, R. T. Howe, and D. Liepmann, "Fluidic microassembly using patterned self-assembled monolayers and shape matching," in *Proc. 1999 Int. Conf. on Solid-State Sensors and Actuators (Transducers)*, (Japan), pp. 1170–1173, 1999.

[59] U. Srinivasan, D. Liepmann, and R. T. Howe, "Microstructure to substrate self-assembly using capillary forces," *ASME/IEEE J. of Microelectromechanical Systems*, vol. 10, no. 1, pp. 17–24, 2001.

[60] H. O. Jacobs, A. R. Tao, A. Schwartz, D. H. Gracias, and G. M. Whitesides, "Fabrication of a cylindrical display by patterned assembly," *Science*, vol. 296, pp. 323–325, 2002.

[61] U. Srinivasan, *Fluidic Self-Assembly of Microfabricated Parts to Substrates Using Capillary Forces. Ph.D Thesis.* University of California at Berkeley, Department of Chemical Engineering, 2001.

[62] M. D. Porter, T. B. Bright, D. L. Allara, and C. E. D. Chidsey, "Spontaneously organized molecular assemblies. 4. structural characterization of n-alkyl thiol monolayers on gold by optical ellipsometry, infrared spectroscopy, and electrochemistry," *Journal of American Chemical Society*, vol. 109, no. 12, pp. 3359–3568, 1987.

[63] N. L. Abbot, A. B. Gorman, and G. M. Whitesides, "Active control of wetting using applied electrical potentials and self-assembled monolayers," *Langmuir*, vol. 11, no. 1, pp. 16–18, 1995.

[64] C. D. Bain, E. B. Troughton, Y. T. Tao, J. Evall, G. M. Whitesides, and R. G. Nuzzo, "Formation of monolayer films by the spontaneous assembly of organic thiols from solution onto gold," *Journal of the American Chemical Society*, vol. 111, pp. 321–335, 1989.

[65] Y. Xia and G. M. Whitesides, "Soft lithography," *Angew. Chem. Int. Ed.*, vol. 37, pp. 550–575, 1998.

[66] F. Ma and R. B. Lennox, "Potential-assisted deposition of alkanethiols on au: Controlled preparation of single- and mixed-component sams," *Langmuir*, vol. 16, pp. 6188–6190, 2000.

[67] G. E. Poirier and E. D. Pylant, “The Self-Assembly Mechanism of Alkanethiols on Au(111),” *Science*, vol. 272, no. 5265, pp. 1145–1148, 1996.

[68] C. J. Zhong and M. D. Porter, “Fine structure in the voltammetric desorption curves of alkanethiolate monolayers chemisorbed at gold,” *Journal of Electroanalytical Chemistry*, vol. 425, pp. 147–153, 1997.

[69] M. M. Walczak, D. D. Popenoe, R. S. Deinhammer, B. D. Lamp, C. Chung, and M. D. Porter, “Reductive desorption of alkanethiolate monolayers at gold: A measure of surface coverage,” *Langmuir*, vol. 7, no. 11, pp. 2687–2693, 1991.

[70] S. Abbott, J. Ralston, G. Reynolds, and R. Hayes, “Reversible wettability of photoresponsive pyrimidine-coated surfaces,” *Langmuir*, vol. 15, pp. 8923–8928, 1999.

[71] M. E. Schrader, “High- and medium-energy surfaces: Ultrahigh vacuum approach,” in *Modern Approaches to Wettability: Theory and Applications* (M. E. Schrader and G. I. Loeb, eds.), pp. 53–71, 233 Spring Street, New York, New York 10013-1578: Plenum Publishing Corporation, 1992.

[72] H. O. Finklea, “Electrochemistry of organized monolayers of thiols and related molecules on electrodes,” *Electroanalytical Chemistry*, vol. 19, pp. 109–335, 1996.

[73] X.-M. Zhao, J. L. Wilbur, and G. M. Whitesides, “Using twostage chemical amplification to determine the density of defects in self-assembled monolayers of alkanethiolates on gold,” *Langmuir*, vol. 12, pp. 3257–3264, 1996.

[74] A. J. Bard and L. R. Faulkner, *Electrochemical Methods: Fundamentals and Applications*. New York: John Wiley & Sons, 1st ed., 1980.

[75] J. A. Pojman, W. W. West, and J. Simmons, “Propagating fronts of polymerization in the physical chemistry laboratory,” *Journal of Chemical Education*, vol. 74, no. 6, pp. 727–730, 1997.

[76] D. H. Kaelble, *Physical Chemistry of Adhesion.* New York: Wiley-Interscience, 1971.

[77] H. Andersson, C. Jönsson, C. Moberg, and G. Stemme, "Self-assembled and self-sorted array of chemically active beads for analytical and biochemical screening," *Talanta*, vol. 56, pp. 301–308, 2002.

[78] M. D. Berg, M. V. Kreveld, M. Overmars, O. Schwarzkopf, M. de Berg, and M. V. Kreveld, *Computational Geometry.* Springer Verlag, 2nd ed., 2000.

[79] C. Isenberg, *The science of soap films and soap bubbles.* Clevedon : Tieto Ltd., 1978.

[80] K. A. Brakke, "The surface evolver," *Experimental Mathematics*, vol. 1, no. 2, pp. 141–165, 1992.

[81] K. A. Brakke, *Surface Evolver Manual.* Mathematics Department, Susquehanna University, Selinsgrove, PA, August 18 1999. http://www.susqu.edu/facstaff/b/brakke/.

[82] K. F. Böhringer, U. Srinivasan, and R. T. Howe, "Modeling of capillary forces and binding sites for fluidic self-assembly," in *Proc. of IEEE Workshop on Micro Electro Mechanical Systems (MEMS)*, (Switzerland), pp. 369–374, 2001.

[83] X. Xiong, Y. Hanein, W. Wang, D. T. Schwartz, and K. F. Böhringer, "Multi-batch micro-selfassembly via controlled capillary forces," in *International Conference on Intelligent Robots and Systems*, (Maui, HI), IEEE/RSJ IROS, October – November 2001.

[84] D. Allara and R. Nuzzo, "Modifications of properties of metals," in *U.S. Patent Application 389/775*, June 18 1982.

[85] R. Nuzzo and D. Allara, "Adsorption of bifunctional organic disulfides on gold surfaces," *Journal of American Chemical Society*, vol. 105, pp. 4481–4483, 1983.

[86] S. Chen, L. Li, C. L. Boozer, and S. Jiang, "Controlled chemical and structural properties of mixed self-assembled monolayers of alkanethiols on Au(111)," *Langmuir*, vol. 16, no. 24, pp. 9287–9293, 2000.

[87] H. O. Finklea, "Self-assembled monolayers on electrodes," in *Encyclopedia of Analytical Chemistry: Applications, Theory, and Instrumentation* (R. A. M. E. in Chief), ed.), John Wiley & Sons, June 2001.

[88] G. Poirier and E. Pylant, "The self-assembly mechanism of alkanethiols on au(111)," *Science*, vol. 272, pp. 1145–1148, 1996.

[89] D.-F. Yang and M. Morin, "Chronoamperometric study of the reductive desorptionof alkanethiol self-assembled monolayers," *Journal of Electroanalytical Chemistry*, vol. 441, pp. 173–181, 1998.

[90] C. A. Widrig, C. Chung, and M. D. Porter, "The electrochemical desorption of n-alkanethiol monolayers from polycrystalline au and ag electrodes," *Journal of Electroanalytical Chemistry*, vol. 310, pp. 335–359, 1991.

[91] J. W. Dini, *Electrodeposition: The Materials Science Of Coatings And Substrates.* New Jersey: Noyes Publications, 1993.

[92] W. S. N. Trimmer, "Microrobots and micromechanical systems," *Sensors and Actuators*, vol. 19, no. 3, pp. 267–287, 1989.

[93] W. Moench and H. Zappe, "Fabrication and testing of micro-lens arrays by all-liquid techniques," *Journal Of Optics A: Pure And Applied Optics*, vol. 6, pp. 330–337, 2004.

[94] M.-H. Wu and G. M. Whitesides, "Fabrication of two-dimensional arrays of microlenses and their applications in photolithography," *Journal of Micromechanics and Microengineering*, vol. 12, pp. 747–758, 2002.

[95] L. Xu and M. Salmeron, "Studies of wetting and capillary phenomena at nanometer scale with scanning polarization force microscopy," in *Nano-Surfcae Chemistry* (M. R. (Editor), ed.), pp. 243–288, JMarcel Dekker Inc. New York, NY, 2002.

[96] Z. Zhong, B. Gates, and Y. Xia, "Soft lithographic approach to the fabrication of highly ordered 2D arrays of magnetic nanoparticles on the surfaces of silicon substrates," *Langmuir*, vol. 16, pp. 10369–10375, 2000.

[97] S. Lee, H. McNally, D. Guo, M. Pingle, D. Bergstrom, and R. Bashir, "Electric-field-mediated assembly of silicon islands coated with charged molecules.," *Langmuir*, vol. 18, no. 8, pp. 3383–3386, 2002.

[98] K. Nagayama, "Two-dimensional self-assembly of colloids in thin liquid films," *Colloids Surfaces A: Physicochem. Eng. Aspects*, vol. 109, pp. 363–374, 1996.

[99] P. Kralchevsky and N. Denkov, "Capillary forces and structuring in layers of colloid particles," *Current Opinion in Colloid and Interface Science*, vol. 6, pp. 383–401, 2001.

[100] S.-H. Liang, X. Xiong, and K. F. Böhringer, "Towards optimal designs for self-alignment in surface tension driven micro-assembly," in *17th IEEE International Conference on Micro Electro Mechanical Systems (MEMS)*, (Maastricht, Netherlands), 2004.

[101] J. Lienemann, A. Greiner, and J. G. Korvink, "Volume shrinking in micro-fluidic self-assembly," in *4th International Conference on Advanced Semiconductor Devices and Microsystems (ASDAM 2002)*, (Smolenice Castle, Slovakia), pp. 369–372, October 2002.

[102] J. Lienemann, A. Greiner, J. G. Korvink, X. Xiong, Y. Hanein, and K. F. Böhringer, "Modelling, simulation and experimentation of a promising new packaging technology

- parallel fluidic self-assembly of micro devices," *Sensors Update*, vol. 13, no. 1, pp. 3–43, December 2003.

VITA

Xiaorong Xiong received the B.S. degree in mechanical engineering from Huazhong University of Science and Technology, China, and the M.S. degree in industrial engineering from University of Washington, Seattle. She is currently working toward the Ph.D. degree in electrical engineering at University of Washington. In 2001-2002, she was the recipient of a Ford Fellowship. Her research includes development of self-assembly techniques for micro system integration and nano system development.